

Master's thesis

The Application of Supervised Machine Learning in the Search For BSM-Physics

A Study of Dense-, Parametrized- and Ensemble Networks and their Application
to Physics

William Hirst

Computational Science: Physics
60 ECTS study points

Department of Physics
Faculty of Mathematics and Natural Sciences

13th April 2023



William Hirst

The Application of Supervised Machine Learning in the Search For BSM-Physics

A Study of Dense-, Parametrized- and Ensemble Networks
and their Application to Physics

Supervisors:
Professor Farid Ould-Saada
Dr. Eirik Gramstad

Abstract

This will be the abstract.

Acknowledgments

Thank you, to nobody.

Contents

Introduction	1
1 The Standard model of elementary particles and beyond.	3
1.1 The bulding blocks	3
1.2 The Forces	5
1.3 Beyond the Standard Model	5
1.4 Proton-Proton collisions at the LHC	7
1.5 The Background Channels	9
1.6 The Signal	12
2 Introduction to Machine Learning and Data Analysis	13
2.1 Phenomenology	13
2.2 Optimization	14
2.3 Hyperparameters	15
2.4 Data Handling	15
2.5 Regularization	16
2.6 Neural Networks	18
2.7 Decision Trees and Gradient Boosting	24
2.8 Machine Learning Applied to a BSM Search	26
2.9 Model assessment	27
3 Implementation of the Analysis	29
3.1 Tools and Data	29
3.2 Features	32
3.3 The Machine Learning Models	37
3.4 Model Training and Validation	40
4 Results & Discussion	43
4.1 Benchmarking the Analysis with Boosted Trees	43
4.2 Dense Neural Networks	43
4.3 Ensemble methods	46
4.4 Parametrized Neural Network	52
4.5 Comparing Models on Original Signal Set	55
4.6 Increasing Sensitivity through PCA	55
4.7 Comparing Models on Full Statistics Signal	56
4.8 Comparing Exclusion Limits between ML Models and Previous Analysis	59
Appendices	63
Appendix A	65
A.1 Sensitivity Grids	65
A.2 The Features	68
A.3 The implementation of Channel-Out, Stochastic-Channel-Out (SCO) and Maxout	73

Introduction

The Standard Model ([SM](#)) is perhaps one of the most successful scientific theories ever created. It accurately explains the interactions of leptons and quarks as well as the force carrying particles which mediate said interactions. In 2012 the [SM](#) achieved one of its crowning achievements when we discovered the Higgs boson. Much of the accolade was rightfully given to the theoretical work on the [SM](#), but another aspect of the discovery was equally important. Data analysis was and is a crucial part of any new discovery in physics. One of the most important and exiting tools is Machine Learning ([ML](#)).

Outline of the Thesis

Chapter 1

The Standard model of elementary particles and beyond.

The **SM** is the most successful scientific theory ever created. It accurately explains the interactions of leptons and quarks as well as the force carrying particles which mediate said interactions. The model is a result of over a century of work demanding the contributions of great minds like Paul Dirac, Erwin Schrodinger and Richard Feynman. In 2012 the SM achieved one of its crowning achievements when we discovered the Higgs boson [1]. In spite of the success of the **SM**, there are still questions we are unable to answer. **SM** is yet to merge the physics of the micro and macro or even accommodate the particles that make up most of the universe. Most people believe this is not a sign to discard the **SM**, but instead to expand it!

1.1 The bulding blocks

As early as ancient Greece, humans pondered the nature of the most elementary building blocks of the universe. The Greeks imagined a rope of a given length and a pair of scissors with adjustable size. Then one could ask, how many times can you cut the rope in half? If the answer is less than infinite, what are you left with?

In 1897, Joseph John Thomson (1856-1940) discovered the first elementary particle using the Cathode Ray Tube [2]. The particle that Thomson discovered was named the *electron*. Prior to the time of discovery, we believed atoms to be the smallest building blocks. After the discovery of the electron, the discovery of the proton and neutron quickly followed. It was not until more than 50 years after the discovery of the proton (by Ernest Rutherford 1871-1937 [3]) that we discovered that also protons and neutrons could be further dissected to smaller particles. We call these particles quarks. The "final-piece"¹ of the puzzle came in 1956 [4] when we discovered the (at that time thought of as massless) neutrino. Together, the electron and the neutrino form the leptons. We refer to both the leptons and the quarks as fermions.

Upon the evolution of quantum mechanics and physics as a whole, we started to divert our focus from the what and over to the how. How can we explain all the complex interactions that emerge between these relatively simple particles? Through the creation of **SM** and countless experiments, we discovered that forces are nothing but interactions between particles and fields. The **SM** describes all forces as a field which are mediated through a particle, we call gauge bosons.

The four forces responsible for all the forces in the universe are electromagnetism (Quantum Electro Dynamics (**QED**)), the weak-force, the strong-force(Quantum Chromo Dynamics (**QCD**))) and gravity. The boson most familiar to most is the photon. The photon is responsible for the mediation of **QED** and is responsible for all electromagnetic effects, such as the ones allowing us to see objects using our eyes. Similarly, the W^\pm and Z bosons are responsible for the weak-force which allows for radioactive decay. And the gluon is responsible for **QCD** which holds protons and neutrons together. Gravity is the only force not included in the SM, but would (if one day included) have its own force carrying particle, graviton.

The final building block in the universe introduced and described by **SM** is the Higgs boson. The Higgs boson was proposed by Robert Brout, Francois Englert and Peter Higgs in 1964 and discovered at CERN in 2012. The Higgs boson, sometimes called the God particle is responsible for giving particles mass in a process called spontaneous symmetry breaking of the electroweak theory [5]. Together the fermions and the bosons make up all the particles in the **SM**.

¹Given the nature of this thesis, the existence of further pieces is implied.

Generation	Flavour	Mass [MeV]	Charge [Elementary charge]
1st	e	0.511	-1
1st	ν_e	< 0.001	0
2nd	μ	105.66	-1
2nd	ν_μ	< 0.17	0
3rd	τ	1776.8	-1
3rd	ν_τ	< 18.2	0

Table 1.1: A list of all leptons along with their generation, flavor, mass and charge.

Generation	Flavour	Mass [MeV]	Charge [Elementary charge]
1st	u	2.2	-2/3
1st	d	4.7	+1/3
2nd	c	1280	-2/3
2nd	s	96	+1/3
3rd	t	173100	-2/3
3rd	b	4180	+1/3

Table 1.2: A list of all quarks along with their generation, flavor, mass and charge.

1.1.1 The leptons

The leptons are all elementary particles with half-integer spin², $\pm 1/2$. A lepton can be either charged or neutral. For reasons that are yet to be known, the leptons come in 3 generations. Each generation contains a pair of charged and neutral lepton. The first generation contains the electron, e^- and the electron-neutrino, ν_e . The second contains the muon, μ and the muon-neutrino, ν_μ . And the third generation contain the tau, τ^- and ν_τ . The generations are numbered by the mass of the charged lepton, where the first generation is the lightest. As is often the case in particle physics, the heavier a particle, the rarer. This is due to the heavier particles (higher generations) quickly decaying into lighter particles (lower generation), in a process we call particle decay. This explains why particle physicists often neglect the τ when speaking about leptons, given that this is by far the heaviest and also the rarest.

The charged leptons are all massive particles ranging from a fraction of 1eV to more than a 10^9 eV. The neutrinos were up until the turn of the millennia presumed to be massless. This was not only backed by experiments but also by the SM which seldom seemed to be wrong. In 1998 [6], it was discovered that neutrinos in fact do have mass although being extremely light. Given the size of the masses we are yet to accurately measure the mass of the neutrinos, but we have found them all to be less than 20 MeV.³ The fact that the neutrinos in fact do have mass is a problem which will be discussed further in later section. In table 1.1, a summary of all leptons is found, along with the respective mass and electric charge.

1.1.2 The quarks

'Three quarks for Muster Mark!
Sure he hasn't got much of a bark.
And sure any he has it's all beside the mark.' [7]

The poem above was written by James Joyce (1882-1941) in 1939, and was the motivation for Gell-Mann (1929-2019) when naming the inner particles of hadrons, quarks. Quarks were introduced to explain some strong-force properties of hadrons. We can categorize quarks as being either positively charged or negatively charged. All down-type quarks have a negative charge equal to 1/3 that of the electron (e) and all positive quarks have a positive charge equal to 2/3 that of the electron (+e). Similarly to leptons, all quarks have a spin equal to 1/2 and are divided in 3 generations. Each generation of quarks are made of a pair of one positive and one negative quark. The first generation contains the up, u and the down, d quark, the second the charm, c and the strange, s quark and third the top, t and the bottom, b quark. Also similarly to leptons, the higher the generation and mass the more energy is need to create them.

Similarly to how difference in spin allows leptons to stay in an otherwise similar quantum state, the quarks have color. The colors of quarks are what connects them to the strong-force. QCD is what allows quarks to change color. It predicts asymptotic freedom when quarks are free at short distances, also known as color

²Spin is a quantum number which predicts the effect of an applied electromagnetic field.

³The lightest neutrino ν_e , is found to have an upper bound of 1eV.

confinement. Briefly explained, color confinement results in quarks never existing in isolation but always in a quark-antiquark pair, mesons or in three quark state, baryons (like protons and neutrons). Given color confinement, quarks are never directly observed in experiments, instead we detect the signature of quarks forming hadrons in a process called hadronisation. We call these signature jets of hadrons.

1.2 The Forces

Why do the nuclei of atoms stick together? Why do the electrons revolve around said nuclei? And why can neutrons decay to photons and vice versa? These phenomena are all described through the interactions of leptons and quarks. But how do we describe the interactions? In the previous section I briefly mentioned that the interactions of the leptons and quarks (or fermions) are mediated by the gauge bosons. The explanation of force as a mediation of bosons is the cornerstone of the **SM** and is explained through the introduction of Quantum Field Theory (**QFT**). **QFT** is a precise mathematical framework which relies on the properties of local symmetries (Gauge symmetries) and field theory. Given the scope of this thesis an introduction to **QFT** will not be given, yet certain attributes of the forces themselves are of interest.

1.2.1 Electromagnetism

Electromagnetism is one of the two macroscopic forces⁴. This means that most people have directly experienced it and therefore have built an intuition for it. If you place two oppositely charged objects close enough, they attract. The closer they are, the more they attract. Electric charge is the property that causes particles to experience electromagnetic forces. This is due to the boson responsible for mediating it, the photon (γ). The photon is massless, and only couples to particles with an electric charge, which means only particles with a non-zero charge can interact through the electromagnetic force.

1.2.2 The Strong Force

The strong force is, alongside the weak force a microscopic force, meaning that although we never experience it directly. The strong force holds nuclei together and is (as the name suggests) the strongest force. Similarly to how electric charge plays a role in electromagnetism, the strong force has *color*. Not to be mistaken with the spectrum of frequencies of light, color in the **SM** is known as the charges associated with the strong force. Where there is one electric charge, color is instead a collection of three conserved charges, 'r', 'b' and 'g'. Like the photon, the gluons carry color and anticolor and only couple to colorful⁵ particles. Due to the three color charges, there exists a collection of independent color states, 8 which corresponds to the number of gluons. The only particles with color are the quarks, antiquarks and gluons, which explain why only they experience the strong force.

1.2.3 The Weak Force

The weak force is the weakest of all the forces of the **SM**. This is due to the bosons coupling weakly to fermions, and the fact that the W^\pm and Z are very heavy. The charged weak force is the only force which allows for flavor change⁶. They interact only with left-handed particles. The charge associated with the weak force is the weak isospin. All left-handed fermions and right handed-handed antifermions have non-zero isospin ($1/2$), meaning the W and Z bosons interact with both the leptons and the quarks.

1.3 Beyond the Standard Model

1.3.1 Why look beyond?

'There is nothing new to be discovered in physics now.

All that remains is more and more precise measurement.' [8]

The quote above is rumored to have been spoken by William Thompson (1824–1907), better known as Lord Kelvin when addressing the British Association for the Advancement of Science in 1900. The statement was

⁴The other being gravity.

⁵Meaning particles with a non-zero color charge.

⁶Flavor is a term used to differentiate the fermions, i.e. the six leptons (electron, muon, electron neutrino etc.) and six quarks (top, bottom, charm etc.). A change in flavor therefor means to transition from one of this flavor to another through the weak charge bosons. For example $\mu_e \rightarrow e^- W^+$

followed by a long period of advancements in the field of physics by the likes of Max Planck (1858–1947) and Albert Einstein (1879–1955). Less than half a decade after Lord Kelvin uttered the famous words, began the development of Quantum Mechanics. Just as Kelvin was wrong back then, would he be wrong today. For although **SM** explains a large range of phenomena, there are yet many mysteries to explain in the universe and even problems rooted in **SM**. In this section I will present some of the problems we hope to tackle in the future.

- **SM** in its current form cannot incorporate *gravity*, as it does not have sufficient symmetry. The hope has been to integrate gravity into **SM** through the discovery of a gravity-carrying particle, the graviton [9]. So far, no-such particle is found.
- *Dark matter* and *dark energy* make up more than 90% of the mass in the observable universe, but is found to lie beyond the **SM** [10].
- Inflation is today the leading explanation to what happened in the early-stages (the first fraction of a second) of the universe. It explains a universe in which all space undergoes a rapid increase in rate of expansion. None of the fields explained by **SM** are capable of causing any such expansion.
- Finally, and the one most relevant for this analysis; what is the origin of the neutrino mass and is Charge-Parity (**CP**) violated in the neutrino sector?

1.3.2 Neutrino-Mass problem

Neutrinos have a special place in physics. For one, they are the only particles that only interact by the weak force. This means that neutrinos rarely interact at all. It is often used as a (granted for many not incredibly exciting) conversation piece that a colossal amount (*ca.* 10^{14}) of neutrinos pass through your body every second. This is harmless to us exactly because of the rarity of neutrinos interaction with anything. For this reason we call neutrinos ghostly.

Another reason neutrinos are special is that they exhibit flavor mixing. In 2015 Arthur McDonald (1943-) and Takaaki Kajita (1959-) were awarded the Nobel Prize for their contributions in the discovery. In simple terms, flavor mixing is a process where a particle oscillates between different flavors. For neutrinos this means oscillating between ν_e , ν_μ and ν_τ . Flavor mixing is in itself not special. Quarks have been observed to exhibit the same behavior. The reason this is interesting in the case of neutrinos, is that it implies that neutrinos are massive. Before this discovery, we believed neutrinos to be massless. But why are massive neutrinos a problem?

All (previously) known massive particles gain mass through interactions with the Brout-Englert-Higgs (**BEH**) field. For particles to gain mass they need to have a right- and left-handed⁷ particle. So far, no right-handed neutrinos have been observed, due to them being sterile⁸ in the **SM**. Generally there are two schools of thought for why a right-handed neutrino has not been observed. Either, it is very heavy, and we are yet to generate energies large enough to recreate it, or it is indistinguishable to the left-handed neutrino. In the first scenario we would call the right-handed neutrino a *Dirac* fermion. This means that it is no different from any other right-handed lepton as far as mass is concerned. In the second the right-handed neutrino is a *Majorana* fermion. A Majorana fermion is simply a lepton where the particle and the antiparticle are the same. In this thesis I have searched for a right-handed neutrino and considered both Majorana and Dirac neutrinos.

1.3.3 Super Symmetry and the Neutralino

A supersymmetric theory has for many years been an interesting candidate for a new physics beyond the standard model. Supersymmetry (**SUSY**) aims to alter the standard model such that mass and force (or fermions and bosons) is treated equally. **SUSY** suggests that each **SM** particle has an additional Superpartner (**SP**) which we call a sparticle. The sparticles all differ with half a spin from the original **SM** particle. Because **SUSY** is a broken symmetry, sparticles are expected to be much higher than the corresponding **SM** masses, often in the range of 100- 1000GeV. The difference in spin means that the **SP** of a fermion is a scalar boson and the **SP** of a boson is a fermion. **SUSY** is a candidate to fix many problems in physics, some of which are; the hierarchy problem, fixing the mass of the Higgs and possibly the mystery of dark matter. There are many variants of **SUSY**, all of which introducing a set of new particles. In this thesis I will study a signal which stems from the simplest variant of **SUSY**, which is the most similar to **SM**, naimly the Minimal

⁷For a massless particle NB FIX. The handedness of a particle is defined as a relation between the direction of spin and momentum for a particle. Right means the two are directed in the same direction and left corresponds to opposite direction.

⁸Non-interacting.

Supersymmetric Standard Model ([MSSM](#)). For a more thorough explanation of [SUSY](#) and its application, the reader is referred to Refs.[\[11\]](#).

1.4 Proton-Proton collisions at the LHC

1.4.1 An Introduction to Particle Accelerators and Detectors

With a circumference of 27 km, the *particle accelerator* Large Hadron Collider ([LHC](#)) is the largest piece of scientific equipment ever built. It consists of two separate large tubes aligned with powerful magnets. The magnets are used to accelerate bunches⁹ of hadrons (specifically protons) and lead. One set of bunches are accelerated in one of the tubes, and another set is accelerated in the other direction inside the other tube. The bunches are accelerated up to close ($v=0.99999991c$) the speed of light before they collide at a rate of once every 25 nanosecond. The released energy from the collisions enable the creations of new particles. To measure the collisions, we use *particle detectors*. In this thesis I will be using data collected by the [ATLAS](#) (A Toroidal LHC Apparatus) detector. The [ATLAS](#)-detector is the largest general-purpose detector at the [LHC](#) and was first active in 2009. The detector consists of several ever-increasing cylindrical layers around the point of collision. In figure 1.1, taken from the [ATLAS](#) collaboration [\[12\]](#) the cross section of the detector along with the paths of different particles is visualized. The inside of a detector can be summarized in the following points, listed from innermost to outermost layer:

- *Inner Detector*: The inner detector consists of three layers, Pixel detector, Semi-Conductor Tracker and Transition Radiation Tracker. Its purpose is to measure electromagnetic interactions between the particles produced in the collision and the material in the layers. The measurements are made at discrete points and can be used to infer the momentum of the particles. An electromagnetic field is applied to the inner detector to curve the paths of the particles, so to measure properties of the particles like spin and charge.
- *Calorimeters*: The [ATLAS](#) detector has two calorimeters, the *Electromagnetic calorimeter* and the *Hadronic calorimeter*. The Electromagnetic ([EM](#)) calorimeter is the first layer of the two and measures the energy of particles interacting through the [EM](#) field. The hadronic calorimeter is designed to measure the energy of hadrons (i.e. protons, neutrons, mesons etc.).
- *Muon Spectrometer*: The muon spectrometer is included to detect muons, which would otherwise not be measured by the previous layers. Similarly to the inner detector, the muon spectrometer applies a [EM](#) field to curve the path of the particles which allows it to measure several properties.

1.4.2 The Kinematics

The kinematic variables of a particle collision are crucial in any High Energy Physics ([HEP](#)) analysis and are easily explained using simple geometry. In figure 1.2 I have drawn a simple axis to illustrate the kinematics of a particle in both the longitudinal (left) and transverse (right) plane. In a three-dimensional axis where the particles colliding travel along the z-axis, the zy-axis defines the longitudinal plane. The angle between the z-axis and the direction of the momentum of one of the particles, define the polar angle of said particle, θ . The xy-axis define the transverse plane and the angle between the x-axis and the direction of the transverse momentum define the azimuthal angle, ϕ . The transverse momentum and the azimuthal angle are both used in this analysis and are used to create further features. Instead of the polar angle, a preferred feature is the pseudorapidity, η . The pseudorapidity is defined as

$$\eta = -\ln \left[\tan \left(\frac{\theta}{2} \right) \right] \quad (1.1)$$

The pseudorapidity is a preferred feature to the polar angle because differences in η are lorentz invariant under boosts along the longitudinal axis. A large range of features are created using the variables described above. In the appendix I have added a summary of all the features used in this analysis (see table 2). One of said features is the distance between the particle in the $\eta - \phi$ -axis, ΔR . We define ΔR as

$$\Delta R = \sqrt{(\Delta\eta)^2 + (\Delta\phi)^2}. \quad (1.2)$$

⁹Pockets of around 10^{11} protons.

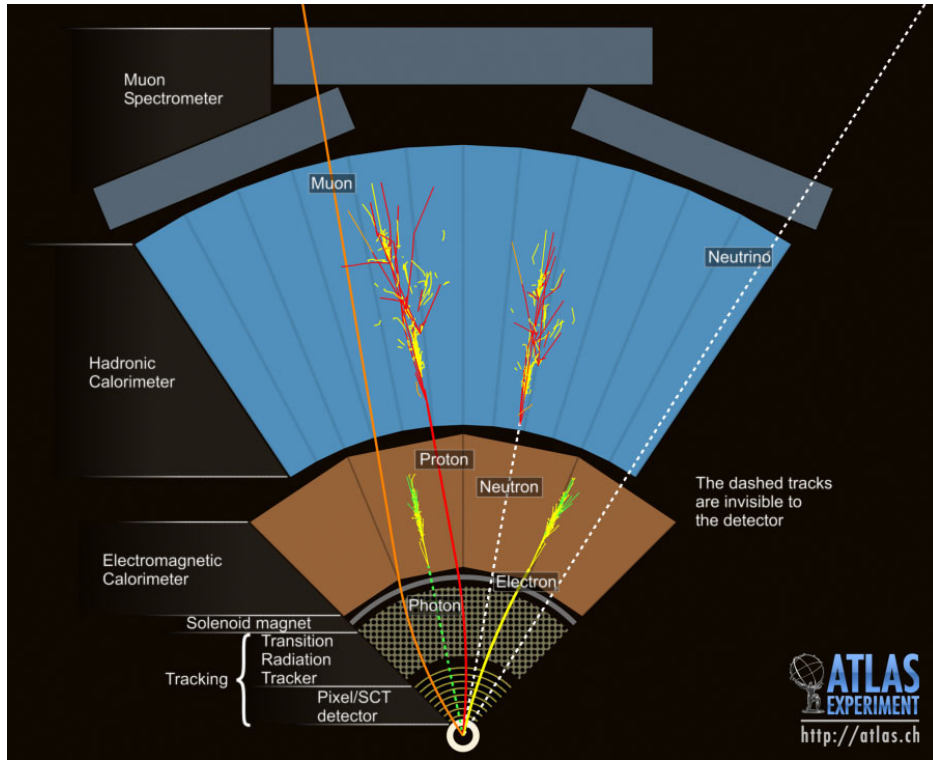


Figure 1.1: Event Cross Section in a computer generated image of the ATLAS detector [12].

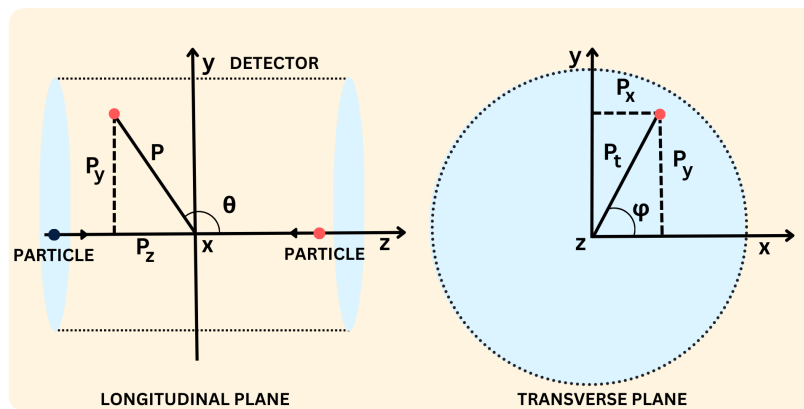


Figure 1.2: An illustration of the general kinematics in a particle-collision, inspired by the figure in the paper by Gramstad [13]. The illustration shows both the longitudinal and transverse plane.

1.5 The Background Channels

We define background as anything that is not of interest and that mimics the signals of new physics considered. As will be further explained in later sections, we will explicitly demand a 3-lepton final-state in all collisions considered in the analysis. This will remove a lot of background, but not all. Due to the imperfect nature of the reconstruction of events, a demand for 3-lepton final-state will not be without errors. This leaves room for more variation in the background than one might expect. In this section I will cover the channels¹⁰ which will be of importance during the analysis. I will also discuss which background channels are the hardest to reduce in a potential new physics signal region, also called the irreducible background. These are channels that exhibit similar trends/distribution in the features. Note that the sections below are listed by contribution to the 3-lepton final-state data (from most to least).

The processes I will describe in the section to come, are classified similarly to how they were classified in the original Monte Carlo (**MC**) simulated data I was given. For the sake of making several of the figures in the thesis more readable, I decided to merge several of the classifications. Diboson(l_{lll}), diboson(l_{ll}) and diboson(l_l) are in later figures, categorized as simply diboson. Similarly, the three smallest processes, triboson, W-jets and Higgs, are all merged to the same category, *Others*.

1.5.1 Z-jets

The Z-jets channel is the largest contribution in all the data. The channel consists of all events resulting in a Z-boson alongside jets. In the cases the Z-boson decays into two leptons, the additional jet acts as a fake lepton and the channel classifies as a 3-lepton final state. In figure 1.3a I have written the Feynman diagram of an example of such a channel. The figure shows a quark-antiquark leading to a Z-boson and gluon. The Z boson decays into two leptons (normally $e^- e^+$ or $\mu^- \mu^+$) and the gluon hadronises as a jet of hadrons which may obtain a b-hadron leading to a fake lepton.

1.5.2 Diboson (l_{ll})

Diboson channels are defined as channels resulting in two bosons. In the case of (l_{ll}), the dibosons decay into a total of three leptons. In figure 1.3b I have drawn the Feynman diagram of an example of such a channel. The figure shows a W- and Z-boson production through a quark-antiquark pair. The W-boson decays into a lepton with missing energy¹¹ and the Z-boson decays into a pair of leptons.

1.5.3 $t\bar{t}$

The $t\bar{t}$ channel is defined as a proton-proton collision resulting in a top quark-antiquark production through the strong interaction. In figure 1.3c I have drawn a Feynman diagram of an example of such a channel. The figure shows gluon-gluon fusion producing a pair of top quarks. The top-antitop pair decay into a bottom-quark and a W boson. The channel constitutes a background when both W bosons decay into a charged and a neutral lepton and one of the b-quarks leads to a fake lepton.

1.5.4 Diboson (l_{lll})

In the case of diboson (l_{lll}), the channel refers to events resulting in two Z-bosons which decay into four leptons. In figure 1.3d I have drawn a Feynman diagram of an example of such a diagram. The figure shows a quark-antiquark pair annihilating into two Z-bosons. The two Z-bosons decay into two pairs of leptons. This process constitutes a background when one of the leptons is not reconstructed in the detector.

1.5.5 Top Others

The top other channel is similar to the $t\bar{t}$ channel, in that it results in top quarks. The main difference between the two, is that the top other process does not produce a top quark-antiquark pair through strong interaction of quarks. In figure 1.3e I have drawn an example of a top other process, where a top quark-antiquark pair is produced from a bottom quark-antiquark pair collision mediated through a W boson. From this point, the top quark-antiquark pair decays to a similar state as described in section 1.5.3.

¹⁰By channels, we refer to the physical diversity which could lead to a specific final-state. Often this refers to the different particles which mediates the process from initial- to final-state.

¹¹Neutrinos very rarely interact with anything, making them almost impossible to detect. We therefore refer to neutrinos as missing energy.

1.5.6 Single Top

The single top channel, similarly to top other and the $t\bar{t}$ channel also produces a top quark, but in the case of single top it only produces the one. In figure 1.3e I have drawn the Feynman diagram of such a channel. The Feynman diagram displays a top quark produced through the strong interaction of a bottom quark and a gluon. The top quark is produced through the interaction with a W boson which decays into a charged-neutral lepton pair and the top quark decays to a W boson and bottom quark.

1.5.7 Diboson (ll)

The diboson(ll), similarly to diboson(llll) produces two bosons, but instead of ending in a four lepton final state, ends in a two lepton final state. Figure 1.3g, displays the Feynman diagram of a diboson(ll) process where a W-pair is produced through the annihilation of two fermions through a charged boson. To produce the two lepton final state, the two bosons must each decay into a charged-neutral lepton pair.

1.5.8 Triboson

The triboson channel is defined as a proton-proton collision producing three bosons. In figure 1.3h, I have drawn a Feynman diagram displaying an example of a triboson process. The Feynman diagram shows a quark-antiquark pair annihilating to three bosons, two W and one Z. The Z-boson decays to a pair of leptons, and the two W bosons each decay into a charged-neutral lepton pair resulting in a 4-lepton final state with missing energy.

1.5.9 W-jets

The W-jets is defined as a proton-proton collision producing a W boson alongside jets. In figure 1.3i I have drawn an example of a Feynman diagram for a W-jets processes. The Feynman diagram displays a pair of quarks colliding to form a W boson alongside a gluon. The gluon decays into a bottom quark-antiquark pair and the W boson decays into a charged-neutral lepton pair. Given that this Feynman diagram only produces the one lepton, it relies heavily on poor reconstruction, and is hence quite rare.

1.5.10 Higgs

Finally, we have the Higgs process, which is defined as proton-proton collision producing a Higgs boson. The Higgs boson is relatively heavy (ca. 125Gev), and is therefore the rarest process in the data set. In figure 1.3j, I have drawn a Feynman diagram of a collision producing a Higgs boson. The Feynman diagram displays a gluon pair annihilation through exchanging a virtual top quark, and producing a virtual top quark-antiquark pair. The latter pair, annihilate, producing a Higgs boson, which quickly (due to its mass) into a pair of Z bosons. The Z boson pair then further decay into a total of 4 leptons.

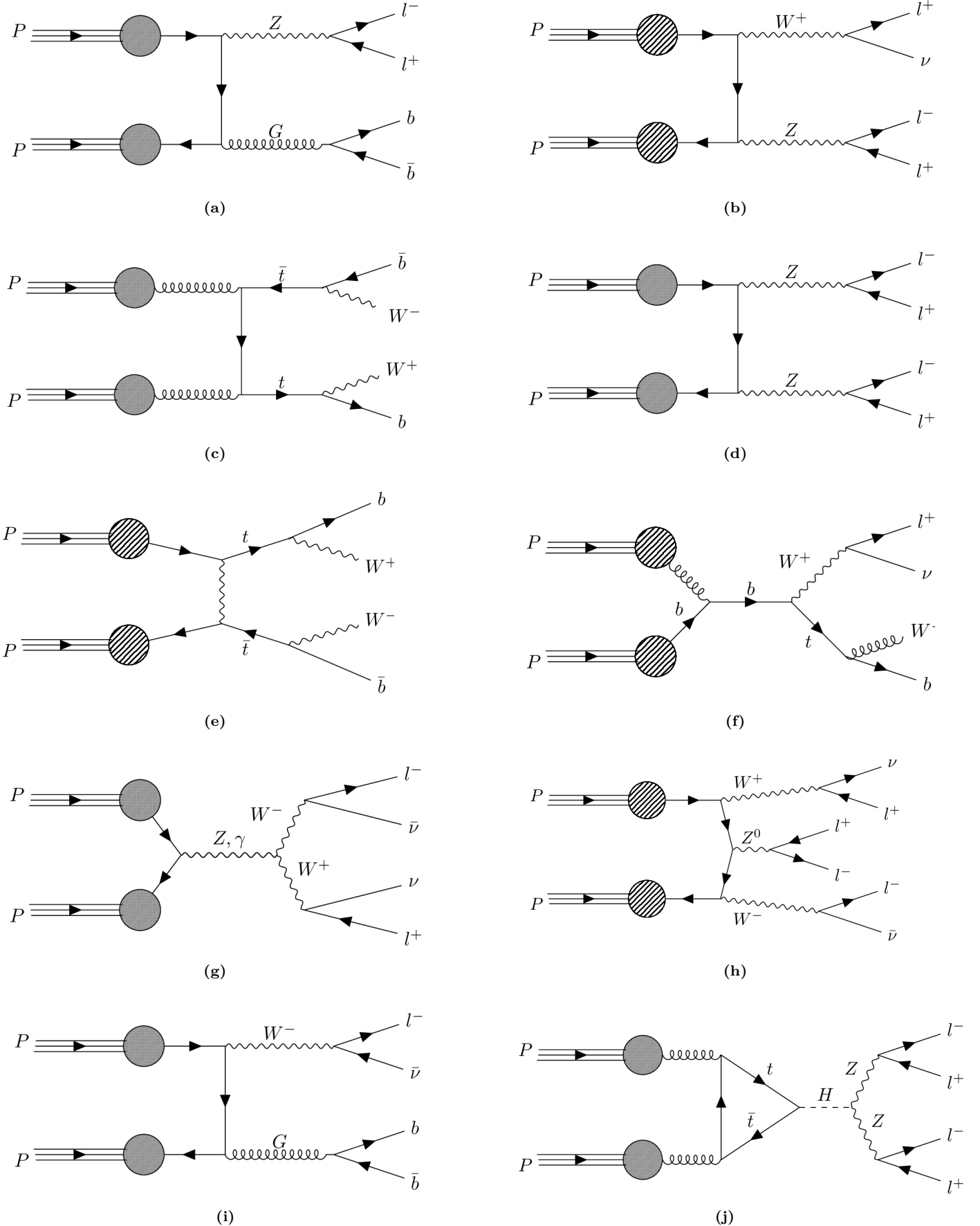


Figure 1.3: A collection of examples of Feynman diagrams for the SM background processes. The diagrams display an example of the processes $Z - jets$ (1.3a), $Diboson(l\bar{l}l\bar{l})$ (1.3b), $t\bar{t}$ (1.3c), $Diboson(l\bar{l}l\bar{l})$ (1.3d), $TopOthers$ (1.3e), $SingleTop$ (1.3f), $Diboson(l\bar{l})$ (1.3g), $Triboson$ 1.3h, $W - jets$ (1.3i) and $Higgs$ (1.3j).

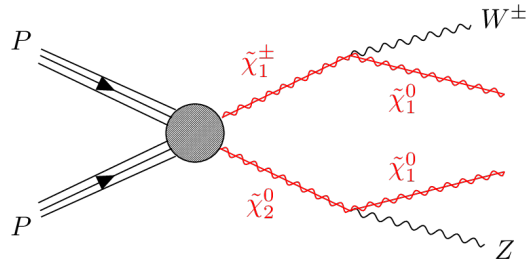


Figure 1.4: The Feynman diagram of the signal-channel.

1.6 The Signal

In this thesis, I will compare [ML](#) models in their ability to learn the trends of the data which will contribute in our ability separate the signal from the background. Specifically for this thesis, I will be studying an expansion of the [SM](#) which includes super symmetry (see section [1.3.3](#)). The signal I will aim to separate from the background, is one which produces a WZ pair, through two neutralinos. In figure [??](#), I have drawn a Feynman diagram for such a process. The Feynman diagram shows a pair of neutralinos, the two lightest neutralinos introduced by the [MSSM](#) ($\tilde{\chi}_1$ and $\tilde{\chi}_2$), and where each neutralino produces a boson (W and Z respectively) and a $\tilde{\chi}_1$.

Chapter 2

Introduction to Machine Learning and Data Analysis

Machine Learning ([ML](#)) is rapidly becoming an overwhelming presence in many scientific fields. In areas ranging from cancer research to stock-trading, machine learning is being applied to problems once thought as impossible to solve. Particle physics, like many other fields is no exception. Jet flavor classification [[14](#)], separating jets from gluons [[15](#)] or using [ML](#) to create efficient Signal region ([SR](#)) are just some examples where [ML](#) is a vital tool. The traditional approach for ML in high-energy physics is the use of supervised Deep Neural Networks ([DNN](#)). [DNN](#)'s are famous for their versatility which is partly due to their diversity in architecture and application. In later years Boosted Decision Trees ([BDT](#)) have become more and more popular, especially after the release of XGBoost in 2014. The performance of XGBoost matches that of the [DNN](#) in many cases, as well as having the advantage of being both stable and easy to use. In this section I will discuss many of the key concepts of [ML](#) as well as go into detail of specific models applied in this search.

2.1 Phenomenology

[ML](#) models differs from other analysis tools in its ability to learn. Where a purely analytical model is static in both method and performance, a [ML](#) model aims to be dynamic and self improving. [ML](#) utilizes data to leverage towards an optimal model. The extent of utilization of data defines a [ML](#) model as being either *supervised*, *semi-supervised* or *unsupervised*. In the case of supervised [ML](#), a set of *targets* are provided along with the data which allows a [ML](#) model to learn how to map a set of inputs to a target. In this thesis I will use the notation of $X = [\mathbf{x}_0, \mathbf{x}_1, \mathbf{x}_2, \dots, \mathbf{x}_N]$ to refer to a dataset, $T = [t_0, t_1, t_2, \dots, t_N]$ to the corresponding target and $Y = [y_0, y_1, y_2, \dots, y_N]$ to the output of the model where N is a number of points. The datasets contain a set of vectors with length equal to the number of features. The target and output could similarly contain vectors, but will in this thesis be restricted to scalar values. Generally, the target values can be both continuous values, in which case the [ML](#) method aims to perform a *regression*, or discrete values, in which case the [ML](#) method aims to perform a *classification*.

The goal of supervised learning is the model can apply any attained knowledge from the study of a set of inputs and targets to predict the target of a new dataset. The success of any prediction is dependent on the quality of the data used during training, or *training-data*. The training-data is required to be both representative of any trends you hope to detect in the new data set (test-data) and be of sufficient amount. The latter point stems from a phenomenon known as *over-fitting*, which is a problem where the training data becomes overly specialized to only predict the target of the training-data, and nothing else^{[12](#)}. In this thesis the main focus will be on the application of supervised learning.

In the case of unsupervised [ML](#), no target is provided. The motivation for unsupervised learning is to create a model which is independent of any target. Such models are often useful in the case where one is not certain what one is looking for. An independence of target means that the model is not overly sensitive to any specific trends or patterns, we call this being *unbiased*. Instead of learning to detect or predict specific phenomenon, unsupervised learning is often used to detect anomalies in the data, which means it relies heavily on statistics. Because of this, some use the term *anomaly detection* and unsupervised learning interchangeably.

Semi-unsupervised learning is a loose term which finds itself in the middle of the previous two. It often refers to methods where no concrete target is provided, but instead uses the data provided to create a target. The

¹²More on this in later sections.

goal is to alleviate as much bias as possible, but at the same time converge towards the usually superior performance of supervised learning.

2.2 Optimization

For a general function C dependent one a set of parameters $\boldsymbol{\theta} = \{\theta_0, \theta_1, \dots, \theta_{N_\theta}\}$, the goal of optimization is to find optimal parameters as defined by a predicated goal. In our case we are interested in finding the set of parameters corresponding to the minimum value of g . Several methods can be applied to optimization problems, all with their own advantages and disadvantages. In most methods the use of the gradient of the function, $\nabla_{\boldsymbol{\theta}}(g)$ is involved in one way or another. Many of the methods used in this analysis are based on one of the simplest optimization methods, the *gradient descent*-method.

2.2.1 Cost functions

How we define the performance of a [ML](#) model is not only important when evaluating the model, but is crucial during training. In the case of classification, it is natural to assume an appropriate metric should involve a comparison between the predicted classification and the true classification. The variation of performance metrics stems from the diversity of how one quantifies the comparison between the two. During training, we define an objective function used to guide the model towards optimal tuning. We call this function the *cost function*.

Binary Crossentropy

The *binary crossentropy* function is a very popular cost function for classification problems, as it can be used to compare the predicted probability distributions to the true probability distributions for a set of classification. It is ideal, as it heavily punishes high probabilities (high output) for wrong classification and heavily rewards high probabilities for correct classifications. For a set of predictions Y and a set of targets T , the binary crossentropy function is defined as

$$\mathcal{C}(Y, T) = - \sum_{i=1}^N [\mathbf{y}_i \log(\mathbf{t}_i) + (1 - \mathbf{y}_i) \log(1 - \mathbf{t}_i)]. \quad (2.1)$$

2.2.2 Stochastic Gradient Descent and Mini-Batches

The gradient descent method aims to obtain the optimal parameters through the application of the derivative of \mathcal{C} with respect to $\boldsymbol{\theta}$. When evaluated at a given point in the parameter space, the negative of the gradient, $-\nabla_{\boldsymbol{\theta}}(\mathcal{C})$ is used to move closer to the optimal set of parameters. The negative of the gradient corresponds to the direction for which a small change $d\boldsymbol{\theta}$ in the parameter space will result in the biggest decrease in the cost function. Finding the minimum value is an iterative process, meaning the steps in the direction of $-\nabla_{\boldsymbol{\theta}}(\mathcal{C})$ is finite. The size of the step is a hyperparameter decided by the user and is called the learning rate, η . The evolution from a step i to $i + 1$ becomes

$$\boldsymbol{\theta}_{i+1} = \boldsymbol{\theta}_i - \eta \cdot \nabla_{\boldsymbol{\theta}}\mathcal{C}(\boldsymbol{\theta}_i). \quad (2.2)$$

Choosing the η can drastically affect the performance of the gradient descent method. Too large and one risks "jumping" over the true minimum or simply never allowing for parameters to reach a high accuracy. Too small and one risks spending computation time beyond reason.

For a given data set of size N , we find the gradient $\nabla_{\boldsymbol{\theta}}(\mathcal{C})$ through the sum of the gradient for each data point \mathbf{x}_i

$$\nabla_{\boldsymbol{\theta}}(\mathcal{C}) = \sum_{i=0}^N \nabla_{\boldsymbol{\theta}}(\mathcal{C}_i(\mathbf{x}_i)) \quad (2.3)$$

The calculation of the gradient over numerous data points can be time-consuming. An alternative approach which both reduces time and introduces a randomness, is the application of *mini-batches*. Instead of summing the gradient over the full data set, one randomly samples a predetermined number of points, B creating a subset of the data which is used to update $\boldsymbol{\theta}$. The points sampled to create the subset, can be sampled both with or without replacement¹³. An epoch is completed after N/B iterations of updating $\boldsymbol{\theta}$. The added

¹³In this analysis the data is sampled with replacement.

stochastic element reduces the risk of getting stuck in local minima. Gradient decent with randomly sampled mini-batches is called Stochastic Gradient Decent ([SGD](#)).

2.2.3 Memory, Adaptive Learning and ADAM

Although [SGD](#) can be highly effective, it tends to be prone to oscillations. To alleviate this issue, we introduce momentum. The momentum aims to functions as a form of memory, conserving some momentum from the previous update. By defining the introduced difference between θ_{i+1} and θ_i as

$$v_i = \eta \cdot \nabla_{\theta} \mathcal{C}(\theta_i), \quad (2.4)$$

we can implement momentum to the algorithm as

$$v_i = v_{i-1}\gamma + \eta \cdot \nabla_{\theta} \mathcal{C}(\theta_i), \quad (2.5)$$

where $\gamma \in [0 - 1]$ is a parameter which defines the size of the momentum.

An additional flaw in the [SGD](#) optimization algorithm, is that it treats all regions in the feature space equally. Ideally, we would want the algorithm to focus on the most relevant areas (steep regions), while quickly moving past less relevant areas (flat regions). A solution to this is the introduction of an *adaptive learning rate*. By updating the learning rate based on the surface of the feature space, one can assign a prioritization in the feature space which optimizes the search for optimal parameters.

The most intuitive way to prioritize steep areas, is by introducing the second derivative of \mathcal{C} , but this can be quite time-consuming. The Adaptive Moment Estimation ([ADAM](#)) optimizer aims to create an approximation of the second derivative, through the use of momentum and an adaptive learning rate. The [ADAM](#) optimizer introduces a set of new parameters, and includes both the linear and squared derivative of \mathcal{C} with memory parameters for both (β_1 and β_2 respectively). Additionally, the [ADAM](#) optimizer holds a memory of the average of the gradient and squared gradient, which is used to create faster convergence. For a thorough description of the [ADAM](#), the reader is referred to the paper by Kingma et al. [[16](#)].

2.3 Hyperparameters

The tuning of parameters is a vital part of building an optimal [ML](#) model, though not all parameters are set during training. Parameters that are chosen prior to training are called *hyperparameters*. We differentiate between two types of hyperparameters; model hyperparameters and algorithm hyperparameters. Model hyperparameters refer to parameters used to define the architecture of the model. Examples of this could be the size and deepness of a Neural Network ([NN](#)) or the maximum deepness of a Decision Trees ([DT](#)). These parameters are not tuned during training, but will nonetheless have a great impact on the performance of the model. Algorithm hyperparameters on the other hand, do not have an impact on the performance of the model. These are parameters that mainly effect the effectiveness and quality of the training process. Examples of this are the learning rate of a [NN](#), or the batch-size used during training. Regardless of if we are discussing model- or algorithm hyperparameters, it is in our interest to find the optimal choice of parameters. The choice of parameters is made prior to the final training, and will be discussed in the following section.

2.4 Data Handling

2.4.1 Scaling

The range of values for the different data features can vary immensely, and for most cost functions, this is a problem. For some features, a deviation on the magnitude of 10^3 can be a good approximation, whereas for others it can be a vast overestimation. When a model is to define which direction it wants to tune, it is crucial that the errors across all features are weighted equally. Scaling aims levitate this problem by transforming all features to have a relatively equal range of values while simultaneously preserving all information regarding each feature. The choice of how one chooses to scale the data will heavily affect the performance of the model and is therefore a part of the model.

Standard Scaler

The *Standrad Scaler* implemented in this rapport uses Scikit-learns's *StandardScaler* [[17](#)]. The standard scaler function scales each feature individually by subtracting the mean and dividing by the standard deviation.

In doing so the resulting scaled data has a mean of 0 and a standard deviation of 1. Mathematically the standard scaler, \mathcal{S} transforms a data set, X as

$$\mathcal{S}(X) = \frac{X - \mu_x}{\sigma_x}, \quad (2.6)$$

where μ_x and σ_x are vectors with the elements being the mean and standard deviation respectively for each feature.

2.4.2 Principal Component Analysis

Principal Component Analysis ([PCA](#)) is a popular dimensionality reduction technique used in many analyses. The goal of [PCA](#) is to reduce a high-dimensional dataset while at the same time conserve as much of the variance in the data as possible. The motivation behind dimensionality reduction is rooted in two (main) reasons. The first being noise reduction. Some features could not only be non-contributing during training, but could even introduce noise. The second reason is lack of convergence. In a large data set with many features and different classifications (in our case channels), a [ML](#) could struggle to identify the most important trends. By reducing the dimensionality in the data, the hope is that this would be easier.

In simple terms, [PCA](#) finds the direction in the feature space along which the data has the largest variance. It does this in 4 steps:

- **First:** Center the data around 0 by subtracting the mean from each feature.
- **Second:** Calculate the covariance matrix to find the covariance of each feature pair.
- **Third:** Calculate the eigenvalue and eigenvectors of the covariance matrix.
- **Fourth:** Order the eigenvector by size of the eigenvalues to define the directions in the feature space with the largest variance.
- **Fifth:** Cast the data along these directions to form a new data set with the new features ranked from largest to lowest variance.
- **Sixth:** Remove the features with the least variance according to some threshold defined by the user.

In figures [2.1](#) and [2.2](#) I have plotted the distribution of 10, 100 and 500 samples for the features with the most and second most variance ([2.1](#)), and least and second least variance ([2.2](#)) after applying [PCA](#) to our data set. In this [PCA](#) I am yet to remove features, so all four features are taken from a data set where all the variance is still conserved. With this in mind, the different scales on the y- and x-axis (10^0 for figure [2.1](#) and 10^{-7} for figure [2.2](#)) show why we are able to justify removing the features. In figure [2.2](#) we observe that all channels exhibit the same trends and are practically identical. In other words, these features would not contribute in training a model to distinguish the different channels.

2.5 Regularization

In [ML](#), overfitting occurs when a model becomes overly tuned to the training data and as a consequence fails to extract trends which would allow it to predict previously unseen data. The architecture of a [NN](#), the maximum depth of a boosted-[DT](#) or even the size of the dataset can all contribute to overfitting. In the case of deep learning especially, overfitting can be a large problem and is therefore of focus in this thesis. Apart from predicting on a new data set, there are no rigid methods to detect overfitting. Instead, there exists many attempts to minimize the risk of it, we call these methods' *regularization*. In [ML](#), regularization is known as any attempt to reduce the error in a prediction by reducing overfitting. Generally one can categorize regularization as being either implicit or explicit. Explicit regularization means adding terms to the optimization problem. This is a very direct way of insuring no part of the model becomes overly dominant. Examples of this could be adding a penalty in the cost function of a [NN](#) to ensure no weights become too large. Implicit regularization is a less direct attempt of hindering overfitting. This could be changing the depth of the [ML](#)-model, varying the cost function or altering the data itself.

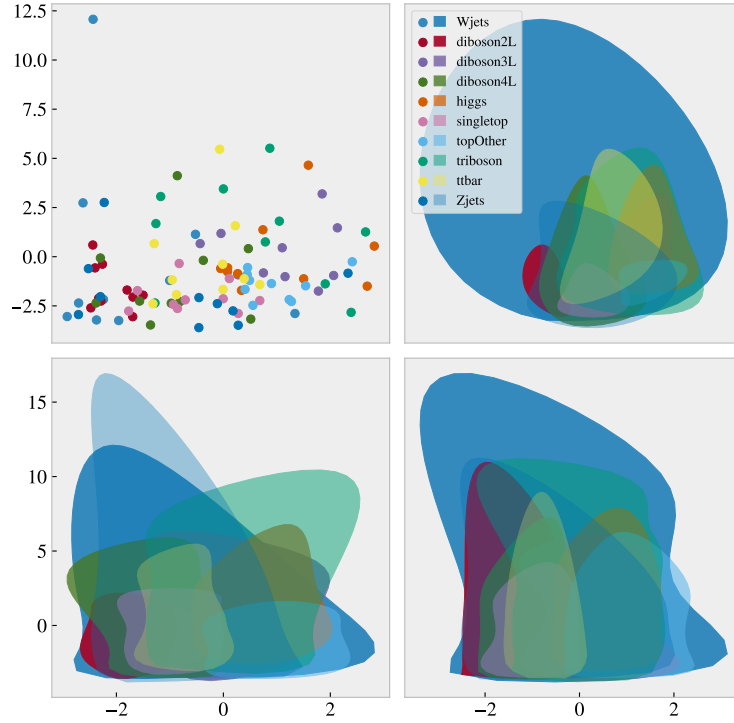


Figure 2.1: The distribution of the two PCA-features containing most variation for (left to right, up to down) 10, 10, 100 and 500 samples from each channel. Each sample filling the requirement with being less than one standard deviation from the mean of both features, respectively.

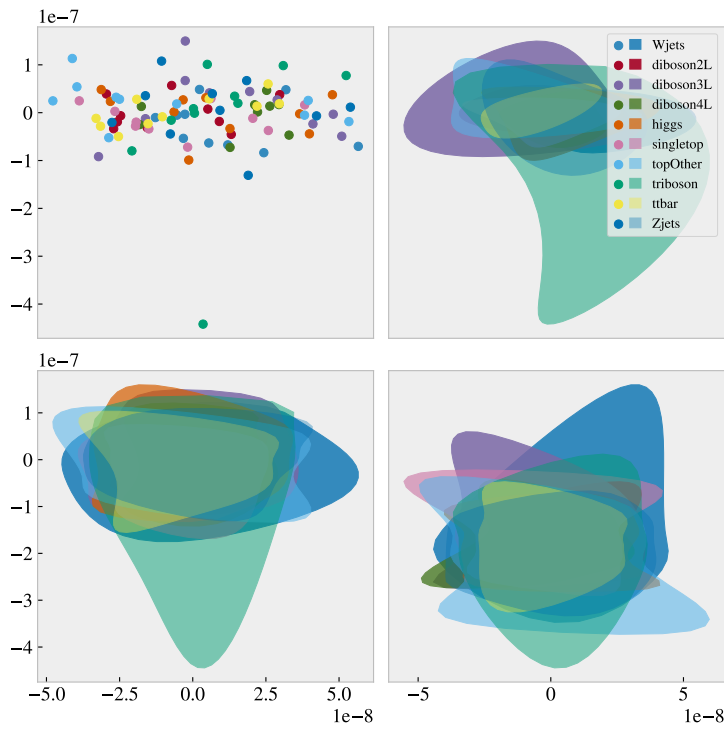


Figure 2.2: The distribution of the two PCA-features containing the least amount of variation for (left to right, up to down) 10, 10, 100 and 500 samples from each channel. Each sample filling the requirement with being less than one standard deviation from the mean of both features, respectively.

2.5.1 Early stopping

A simple implicit regularization method is to introduce *early stopping* in the training pipeline. Early stopping simply means to stop training before the parameters of the model are allowed to over tune. The usual approach is to introduce a goal for the training, which when reached, ends the training. Examples of these goals could be a predetermined loss value on the training set or training until lack of progress on a second unseen dataset. The latter approach is the one I will use in this thesis.

2.5.2 Ensembles

When comparing different **ML** methods by performance, more often than not the top performing model includes ensembling in one way or another. Like the word suggests, ensembling in **ML** means using a collection of **ML** models to create one complex model. There are many ways to create ensembles of models, most methods fall in to one of three categories; *bagging*, *boosting* and *stacking*. Creating an ensemble of models through bagging, means to use several models each trained on their own sample from the same dataset. The overarching new model is created by averaging the predictions from the ensemble of models. The method seeks to create a unique set of models through exposing each individual model to different training sets. Boosting is different to bagging in that it uses the same training data on all the models. The diversity in the models when boosting, stems from intentionally choosing the architecture of the models such that it reduces the error made by the previous ensemble of models. Finally, stacking uses a predetermined model to decide how to combine the predictions made by the ensemble. More on the specifics of bagging, boosting and stacking in later sections.

2.6 Neural Networks

The concept of a **NN** has been around for more than 80 years, and today they are one of the most popular and successful **ML** methods. The key to its popularity stems from its versatility, achieving high performance in a large range of both regression and classification problems. One of the defining qualities in a **NN** is the possibility of diverse architecture, meaning that there are many categorize of **NN**, where each category has an even deeper selection of networks. Categories ranging from Convolutional Neural Network (**CNN**), Recursive Neural Network (**RNN**) to simple Feed-Forward Neural Network (**FFNN**), where each category is specified for their own set of problems. In this section I will introduce some fundamental definitions in regard to **NN**, as well go through the underlying algorithm of the back- and forward propagation.

2.6.1 General structure

There are often drawn comparisons between the structure of the neural network, and the way the human mind operates, hence neural. Similarly to the human mind, a **NN** is composed of different neurons communicating information backwards and forwards in different regions. In the case of a neural network we call these regions layers. All layers are composed of a specified number of neurons. A **NN** has three types of layers; *input-layer*, *hidden-layer* and *output-layer*. There is only one input layer, and it has the same number of nodes equal to the number of features for each data point. There can be an arbitrary number of hidden layers, with each hidden-layer containing an arbitrary number of nodes. Finally, the **NN** has an output layer. The output-layer contains a number of nodes equal to the number of features for the target.

The neural network functions by passing information in between the different layers through nodes. The nodes are simply pockets of information, each containing a value. All the nodes in the input layer are (in most cases) connected to all nodes in the nearest hidden layer, and likewise said hidden layer is connected to the next hidden layer. This structure continues until we reach the final layer, the output layer. The structure is illustrated in figure 2.3. The figure shows a simple **NN** with a 2 dimensional data set (2 nodes in input-layer), 2 hidden layers with three nodes each and a 1 dimensional target value. It also illustrates how a **NN** aims to map from data to a prediction. In figure 2.3 we can see how all the different nodes are connected, illustrated by the arrows. The passing of values between different nodes are controlled by a set of weights and bias parameters. These parameters are defined for each connection and are what will be tuned during training. The weights and biases for a given connection of two nodes, defines the effect one node has on the other.

In a traditional **FFNN** the information is passed linearly (in figure 2.3, from left to right) in a process we call *forward-propogation*. Other variants can include the information taking a more complex route. It is often the route from input- to output-layer that categorizes the type of **NN**. In this report I used a simple **FFNN**.

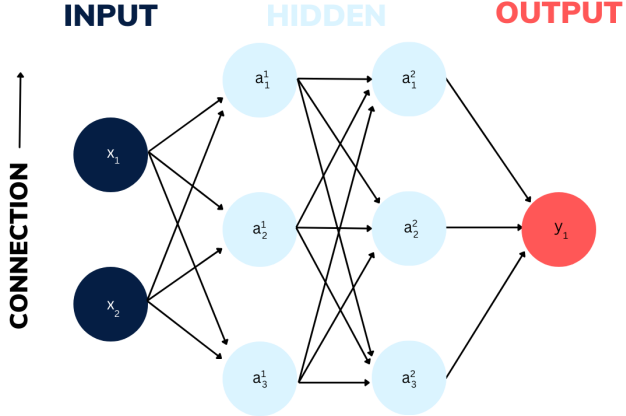


Figure 2.3: An illustration of a NN with two hidden layers.

2.6.2 Feeding Forward

With the structure described in the previous section, a trained model, \mathcal{F} produces a prediction, Y for a data set, X by passing information from input-layer, through all hidden-layers then to output-layer, which we call forward-propagation. In this section I aim to explain the underlying algorithm and math used by the NN to map input to output.

We imagine the passing from hidden-layer $l - 1$ to l , where $l \in \{2, \dots, L\}$ ¹⁴ and L is equal to the number of hidden layers. The value of a node in layer l , is defined as a_j^l (as indicated by figure 2.3), where $j \in \{0, 1, \dots, N_l\}$ and N_l is equal to the number of nodes in l . The value of a_j^l is defined as the *activated sum* of all nodes in the previous layer, a_j^{l-1} where the sum is weighted by a parameter w_{kj}^l and scaled by the bias, b_j^l for $j \in \{0, 1, \dots, N_{l-1}\}$. The activated value of a node j in layer l is defined as

$$z_j^l = \sum_{k=1}^{N_{l-1}} w_{kj}^l a_k^{l-1} + b_j^l, \quad (2.7)$$

where w_{kj}^l corresponds to the weight in \mathbf{w}_k^l specific for the connection between node k and j .

To attain the full activated value, a_j^l we pass z_j^l through the *activation function*. The activation function, σ^l is a generally non-linear function used to control the limit or expand the value range for the node values. The activation function is general for all nodes in a given layer, but can vary in between layers. Therefore, we find a_j^l by the equation

$$a_j^l = \sigma \left(\sum_{k=1}^{N_{l-1}} w_{kj}^l a_k^{l-1} + b_j^l \right) = \sigma^l(z_j^l). \quad (2.8)$$

A more detailed illustration of the information pass from one layer to a node in the next is displayed in figure 2.4. In figure 2.4, we see all steps described in the process; (1) all nodes in $l-1$ are summed with a corresponding weight, (2) the sum is shifted by a constant term (bias), (3) the scaled and weighted sum defines the inactivated value z_j^l , (4) we define a_j^l by passing the sum through σ^l . This method is used for information pass between all layers, except between the first and the second. In this case we simply replace the activated term, a_k^{l-1} in equation 2.8, by the input data, x_i for $i \in \{0, 1, \dots, N\}$, where N is equal to the number of features for the data. In the case $l = 1$, 2.8 becomes

$$a_j^1 = \sigma \left(\sum_{k=1}^N w_{kj}^1 x_k + b_j^1 \right) = \sigma(z_j^1). \quad (2.9)$$

And in the case where $l = L$, a_j^L is equal to the final output.

2.6.3 Back Propagation

The backward propagation acts as the engine that drives the training of a neural network. It has the purpose of tuning the weights and biases of the network to achieve maximum performance, as defined by some *cost*

¹⁴There is a special case for when $l = 1$ which will be addressed in the next paragraphs.

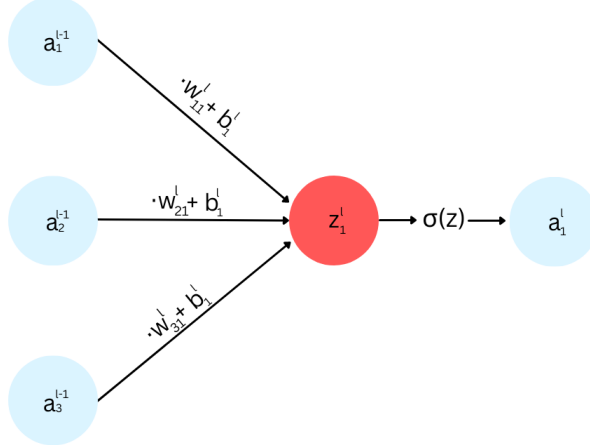


Figure 2.4: An illustration of information pass for one layer to another.

function, \mathcal{C} . The cost function defines to which metric we aim to optimize the network. When a neural network produces a prediction, Y the error in the prediction is defined by the cost function as $\mathcal{C}(Y, T)$, where T is the target. To minimize \mathcal{C} , the backward propagation utilizes the gradient with respect to the weights and biases in the network. Instead of a direct calculation of the gradient, which is very computationally heavy, the backward propagation aims to calculate the gradient through a recursive algorithm which traces the error backwards through the network. It is this algorithm I will describe in this section.

When minimizing the error defined by \mathcal{C} , we can apply several optimization algorithms described in section 2.2. Common for the algorithms is the use of the gradient of the cost function with regard to the tunable parameters. In our case these parameters are the weights and biases, $w_{k,j}^l$ and b_k^l . The goal of the backwards propagation is therefore to calculate the gradients $\partial\mathcal{C}/\partial w_{k,j}^l$ and $\partial\mathcal{C}/\partial b_k^l$.

To begin with we can derive an expression for $\partial\mathcal{C}/\partial w_{k,j}^l$. We use the chain-rule to define

$$\frac{\partial\mathcal{C}}{\partial w_{k,j}^l} = \frac{\partial\mathcal{C}}{\partial z_k^l} \frac{\partial z_k^l}{\partial w_{k,j}^l},$$

which we can simplify further by using equation 2.7 to calculate the second term, which becomes

$$\frac{\partial\mathcal{C}}{\partial w_{k,j}^l} = \frac{\partial\mathcal{C}}{\partial z_k^l} a_j^{l-1}.$$

We can redefine the first term in the equation above as δ_j^l and write

$$\delta_k^l = \frac{\partial\mathcal{C}}{\partial z_k^l} = \sum_j \frac{\partial\mathcal{C}}{\partial z_j^{l+1}} \frac{\partial z_j^{l+1}}{\partial z_k^l} = \sum_j \delta_j^{l+1} \frac{\partial z_j^{l+1}}{\partial z_k^l},$$

where we have again used the chain rule for all contributing nodes.

To calculate the final partial derivative we write

$$\frac{\partial z_j^{l+1}}{\partial z_k^l} = \frac{\partial z_j^{l+1}}{\partial a_j^l} \frac{\partial a_j^l}{\partial z_k^l} = w_{jk}^{l+1} (\sigma^l(z_j^l))'.$$

This gives the expression for δ_k^l

$$\delta_k^l = \sum_j \delta_j^{l+1} w_{jk}^{l+1} (\sigma^l(z_j^l))' \quad (2.10)$$

Finally this gives us the expression

$$\frac{\partial\mathcal{C}}{\partial w_{k,j}^l} = \delta_k^l a_j^{l-1}. \quad (2.11)$$

Next we want to derive $\partial \mathcal{C} / \partial b_k^l$. We simply use the chain rule and derive

$$\frac{\partial \mathcal{C}}{\partial b_k^l} = \frac{\partial \mathcal{C}}{\partial z_k^l} \frac{\partial z_k^l}{\partial b_k^l},$$

which from equations 2.10 and 2.11 is simply

$$\frac{\partial \mathcal{C}}{\partial b_k^l} = \delta_k^l \cdot 1 = \delta_k^l, \quad (2.12)$$

From all three derived expressions, equations 2.10, 2.11 and 2.12 we see that to calculate for all $l \in \{0, 1, \dots, N_l\}$ we must first calculate δ_k^L and apply a recursive propagation. To calculate $\delta_k^L = \partial \mathcal{C} / \partial z_k^L$ we simply multiply by $\delta_k^L = \partial a_k^L / \partial a_k^L$, and we find

$$\delta_k^L = \frac{\partial \mathcal{C}}{\partial a_k^L} (\sigma^L(z_k^L))' \quad (2.13)$$

This expression, similarly to equation 2.10 is dependent on the choice of \mathcal{C} and the activation functions. Now that equation 2.13 is defined, we can see that the gradient of the parameters in all other layers can be calculated.

2.6.4 Activation functions

As mentioned in previous sections, activation functions define how the nodes in the previous layer sum to define the value of the node in the current. There are many types of activation functions, where all have advantages and disadvantages. The choice of activation function for each layer is defined before training, making it a hyperparameter. The activation functions applied and tested in this thesis are the following:

- *Sigmoid*

$$\sigma(z) = \frac{1}{1 + e^{-z}} = a \in [0, 1]$$

,

- *Leaky ReLU*

$$\sigma(z) = \begin{cases} z, & \text{if } z \geq 0 \\ \alpha z, & \text{otherwise} \end{cases} = a \in (-\infty, \infty),$$

where α is scalar.

,

where z is an inactivated node which is activated to define a , the activation.

2.6.5 Network Ensembles, dropout and LWTa networks

So far in the thesis, I have only covered dense layers, meaning that every node in the layer before it is connected to its own nodes and likewise all its nodes are connected to the nodes in the layer that follows. This definition covers many, but not all hidden layers. Some layers do not function to pass value to and from between nodes but instead functions by dynamically changing the architecture of the [NN](#). The most popular type of layer that fits this definition, is the *dropout*-layer.

Dropout

The dropout-layer functions by assigning a predetermined probability to each neuron in a given layer. Based on the probability, a number of neurons (dependent on the probability) is dropped in each forward pass. By doing this the dropout-layer creates an architecture for the network for every round of training. Each unique architecture represents its own network in what becomes an ensemble of networks.

As mentioned in previous sections, creating ensembles of models is a form of regularization. In the case of dropout, it minimizes the risk of overfitting by hindering a phenomenon known as complex co-adaptation.

Complex co-adaptation happens when a neuron becomes overly dominant such that neighboring neurons no longer contribute (relative to the dominant neuron) and therefore lack the motivation to tune. When this happens, networks become fragile and overly specialized to the training data. By randomly dropping neurons, the neighboring neurons are no longer allowed to be passive and are forced to tune to compensate. During evaluation, the dropout layers no longer take action. Instead, the dropout rate (fraction of neurons to drop in the layer) r is used to scale the weights by a factor $1 - r$. The prediction made by the resulting model can therefore be seen as the average of all the smaller networks. In other words, a neural network containing dropout-layers as a bagging ensemble (see subsection 2.5.2).

Channel-Out

Dropout-layers are not the only layers to dynamically change the architecture of a network. In this thesis I additionally explored the lesser known, *Channel-Out*-layer as found in the paper by Srivastava et al. [18]. Channel-out, similarly to dropout creates an ensemble of networks by removing a set of nodes for each round of training. Contrary to dropout, channel-out does not choose the nodes to drop at random, but instead creates local *units* by grouping the nodes, and removes all nodes except the node with the largest activation in each respective unit. The goal of channel-out is to create an ensemble of networks where each network is specialized for a given trend in the data. In this thesis I have implemented the layer such that upon prediction, the redimensionalization is still active. This means that for each data point, a neural network is chosen based on the specific activations in each of the nodes. In other words, the channel-out layer creates something resembling a stacking ensemble (see subsection 2.5.2).

Stochastic-Channel-Out

As I will describe in further detail in sections to come, I choose to implement channel-out layer myself. A consequence of this was that I was able to experiment. In section 2.6.5, I described the issue of complex co-adaptation. I also described a possible solution to the issue, the dropout layer. Although dropout and channel-out function rather similarly, they do not deal with this issue similarly. Where the dropout layer will force dormant nodes to contribute in the training by allowing for dominant nodes to be dropped, the channel-out would instead allow for dominant nodes to take further control inside their respective unit. To remedy this issue, I proposed a new layer, the Stochastic-Channel-Out (**SCO**). **SCO** functions similarly to channel-out, with the exception of the units. Where the channel-out utilizes static local units¹⁵ throughout training, the **SCO** instead utilizes dynamic units which changes for each data point. In other words, for each data point, each node would potentially have a new group of nodes to compare with when finding the largest activation. The goal of the **SCO** is to capitalize on the randomness of the dropout layer, and the trend specific paths' aspect from the channel-out layer.

In the same manner as for channel-out, the redimensionalization is active during prediction and training a like for the **SCO**. This means that also the **SCO** creates an ensemble resembling a bagging ensemble.

Maxout

Additionally, to the channel-out I will be applying a second layer proposed by the paper by Srivastava et al. [18], the *Maxout* layer. The maxout layer functions very similarly to the channel-out with a small difference in the dropping of nodes. In the dropout layer, nodes are dropped by neglecting all contributions from said node, or in other words by multiplying the activation by all dropped nodes by zero. This is replicated in both the channel-out layer and the **SCO** layer. In doing so, all nodes, activated and dropped alike, possesses their own set of weights and biases. This is not the case for the maxout layer. In the maxout layer, each unit possesses just one set of weights and biases. For each forward pass in the network, the largest activated node will contribute to the nodes in the following layer using the same weights and biases as the rest of the nodes in the units. However, note that the nodes only share parameters connected to the layer in front, not behind. This allows for the maxout layer to have fewer parameters to tune, while at the same time building trend specific pathways similar to channel-out and **SCO**.

In figure 2.5 I have illustrated a maxout network. The figure shows a **NN** with two hidden layers with 8 nodes each. In the first hidden layer the maxout layer creates 4 units, each containing two nodes and in the second layer the maxout creates two units with 4 nodes each. The resulting output from the first layer is the 4 nodes with the highest activation in their respected unit, likewise the second layers output is 2 nodes. To the right of the network in figure 2.5, I have illustrated how the different configuration of paths through the network creates an ensemble of networks with their own architecture. Note in the figure how, as described in the previous section, each node possesses its own connections to the previous layer, while sharing the

¹⁵I.e. the nodes are placed in local units in the beginning of training and held constant throughout.

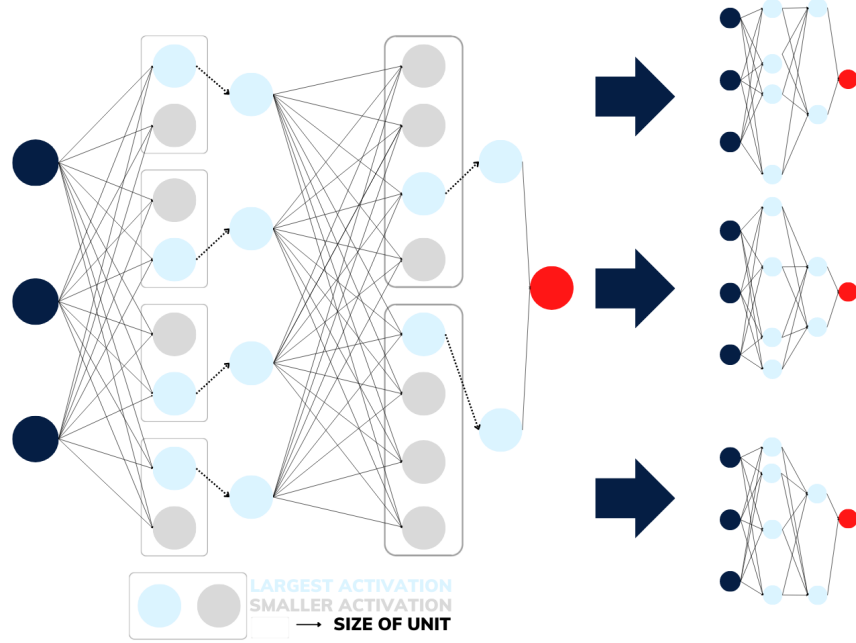


Figure 2.5: An illustration of a Neural network with two hidden layers, each with 8 neurons. The first hidden layer has a maxout activation layer with 4 units, the second has 2. The figure also illustrates the resulting ensemble of smaller neural networks as a consequence of the maxout activation layers.

connections with the rest of the unit, to the next. In figure 2.6 I have drawn a separate illustration to show how this differs from both channel-out and **SCO** in this regard. Figure 2.6 illustrates how all three layers redimensionalize the network, how channelout and **SCO** differ from maxout in regard to the relationship between units and parameters and finally how channel-out differs from **SCO** in choice of units¹⁶

2.6.6 Parametrized Neural Network

In this thesis I will be studying Beyond Standard Model (**BSM**)-simulations with a diversity in choice of free parameters. This means that my signal is in it of itself diverse. The free parameters studied in this thesis are the mass of new particles. The mass of a particle in a collision can greatly alter the feature space spanned by a channel. This means that a **ML**-model could potentially struggle to tune according to all trends in the signal. The obvious solution to this problem is simply to implement one model per mass combination, or

¹⁶In figure 2.6 this is highlighted by the different colors surrounding the nodes in **SCO**, where each color represents a unit.

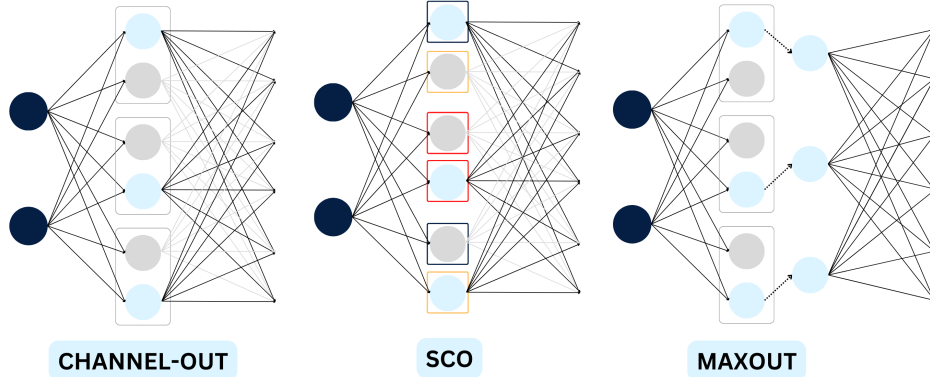


Figure 2.6: An illustration of three different layers, channelout, **SCO** and maxout. The figure shows how each layer redimensionalize the network and how channelout and **SCO** differ from maxout in regard to the relationship between units and parameters.

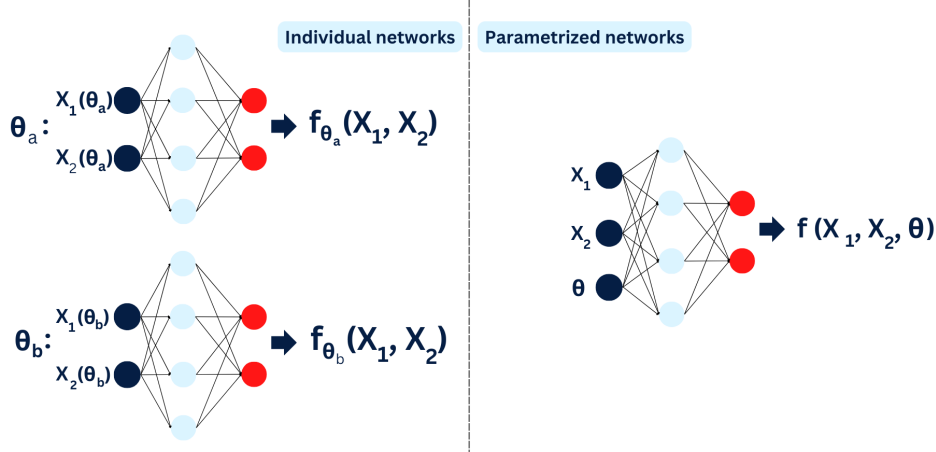


Figure 2.7: An illustration of a comparison between the parameter individualistic network approach and the PNN.

choice of mass and simply reusing the background. Although this approach is very popular, I have decided not to use it for (mainly) three reasons:

- This approach has been carefully studied for many years, and leaves little room to further explore.
- Some signals overlap in the feature space. This means that by neglecting signal with relative similar mass, you could be neglecting statistics which could help tune to your original signal.
- By including two signals with relatively similar masses, some¹⁷ suggest that the model would be able to interpolate between the masses and cover a larger search area.

When the data set is dependent on a set of free parameters, $\theta = [\theta_0, \theta_1, \theta_2, \dots, \theta_N]$, we can write $X(\theta)$. For a single neural network trained on a set of parameters, we define the model as $\mathcal{F}(X(\theta))$. In the case we build one model for each choice of parameter, we get a set of models defined as $\{\mathcal{F}_j(X(\theta_j)), \mathcal{F}_k(X(\theta_k)), \dots, \mathcal{F}_l(X(\theta_l))\}$, where j, k and l are indices which correspond to individual choices of parameters respectively. In the paper by Baldi et al. [19], they propose a separate solution to the problem than the one proposed above, the Parametrized Neural Network (PNN). By simply including the parameters as additional features, we can write $\mathcal{F}(X, \theta)$. In doing so, we can utilize all the statistics at the same time, while also aiding the NN in its effort to recognize all individual trends for all signal. In practice, it is aiding the NN by adding a shift to the total output from the initial layer according to the discrete distribution of the parameters. The hope is that each discrete shift will motivate a separate individualistic tuning for each choice of parameter. For the SM background, adding a parameter representing the mass of a BSM particle is meaningless. Therefore, the background is randomly assigned values according to the same distribution used in the signal data. In doing so, one is essentially assigning each set of signal its own portion of background data.

2.7 Decision Trees and Gradient Boosting

2.7.1 Decision Trees

DT are, similarly to NN one of the most popular ML methods used today. Contrary to NN, DT are famously easy in theory. Despite the simplicity of DT, they are capable of solving a large range of complex problems. In this section I will cover the use of DT as applied to a supervised classification problem. The goal of decision trees are to create a flowchart-like tree structure from input to output. Similarly to the traditional cut-and-count method used in particle physics, a DT places *rectangular-cuts* on a data set. It does so to create a collection of thresholds $\mathcal{C} = \{c_1, c_2, \dots, c_{N_c}\}$, which when applied to a new data set and target, \tilde{X} and \tilde{T} will sort \tilde{x}_i to a \tilde{y}_i .

In figure 2.8, I have illustrated a simple DT classifying a 4-dimensional input data to one of three classifications. As is visualized in figure 2.8, the DT applies a set of thresholds on the data to find the route applicable to a target. For each applied cut, the data split into what we call *branches*. Each branch represents a subset of the data. The final subset, after a sufficient amount of cuts ends in what we call *leaves*. The leaves are the

¹⁷See the paper by Baldi et al. [19].

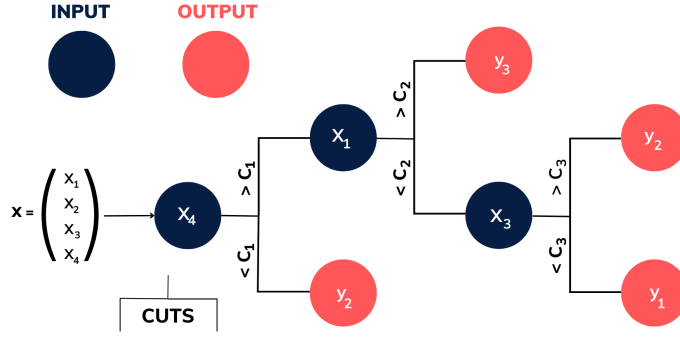


Figure 2.8: An illustration of a simple DT, mapping a 4 dimensional input to one of three values in the target space.

label we assign the subset of data contained in this branch.

Just like most ML-methods, there are many kinds of DT each with their own architecture and benefits. In the case of DT the defining qualities can be summarized in its choice of *Deepness* and *Optimization*. When provided with a data set, \mathcal{D} a DT can in theory create as many cuts needed to map each individual data point, \mathbf{x}_i to the corresponding target, t_i . Doing so would not only be very computationally heavy, but would almost certainly lead to overfitting if applied to any new data. Instead, when building a DT one defines a maximum deepness. This means that we must define a limit to the length of \mathcal{C} , which subsequently leads to the need for a prioritization of cuts.

Building a DT and choosing which cuts to apply at what point, is the equivalent of training a network. How to decide by what standard one chooses to building the hierarchy of cuts is again the equivalent of choosing an optimizer.

2.7.2 Gradient Boosting in Decision Trees

Gradient-boosting is an algorithm which uses a collective of "weak" classifiers in order to create one strong classifier. In the case of gradient-boosted trees the weak classifiers are a collective of shallow trees, which combine to form a classifier that allows for deeper learning. As is the case for most gradient-boosting techniques, the collecting of weak classifiers is an iterative process.

We define an imperfect model \mathcal{F}_m , which is a collection of m number of weak classifiers, estimators. A prediction for the model on a given data-points, x_i is defined as $\mathcal{F}_m(\mathbf{x}_i)$, and the observed value for the aforementioned data is defined as y_i . The goal of the iterative process is to minimize some cost-function \mathcal{C} by introducing a new estimator h_m to compensate for any error, $\mathcal{C}(\mathcal{F}_m(\mathbf{x}_i), y_i)$. In other words we define the new estimator as:

$$\tilde{\mathcal{C}}(\mathcal{F}_m(\mathbf{x}_i), \mathbf{y}_i) = h_m(\mathbf{x}_i), \quad (2.14)$$

where we define $\tilde{\mathcal{C}}$ as some relation defined between the observed and predicted values such that when added to the initial prediction we minimize \mathcal{C} .

Using our new estimator h_m , we can now define a new model as

$$\mathcal{F}_{m+1}(\mathbf{x}_i) = \mathcal{F}_m + h_m(\mathbf{x}_i). \quad (2.15)$$

Similarly to how we define a deepness of trees, we can define the degree of boosting. We define this as the amount of trees used in the iterative process, or M . This means that the final classifier becomes

$$\mathcal{F}_M(\mathbf{x}_i) = \sum_{i=0}^M h_i(\mathbf{x}_i) \quad (2.16)$$

The XGBoost [20] framework used in this analysis enables a gradient-boosted algorithm, and was initially created for the Higgs ML challenge. Since the challenge, XGBoost has become a favorite for many in the ML community and has later won many other ML challenges. XGBoost often outperforms ordinary decision trees, but what it gains in results it loses in interpretability. A single tree can easily be analyzed and dissected, but when the number of trees increases this becomes harder. For more detailed explanation on the XGBoost framework, the reader is referred to Ref.[21]

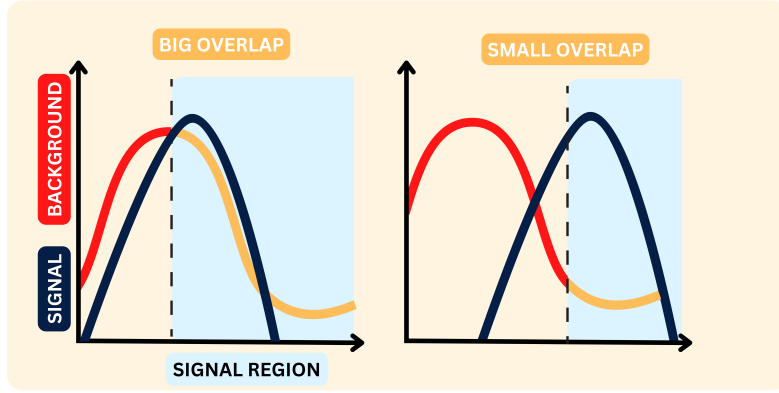


Figure 2.9: An illustration of a traditional cut-and-count approach as well as the motivation for creating a [ML](#) variable.

2.8 Machine Learning Applied to a BSM Search

So far I have presented the goal of my analysis (to discover new physics) as well as the tools ([ML](#)) I will be using to achieve it. In this section I will discuss how [ML](#) is applied to the problem as well as how it compares to traditional methods.

2.8.1 The Traditional Approach

As discussed, I have been presented with two sets of data; the measured collision data from [ATLAS](#) and the simulated [MC](#) data. The origin of the latter data set will not be covered in great detail in this thesis, but it is worth mentioning that the simulations are based on [SM](#) theory. In other words, by comparing the measured collision data with the [SM](#) simulations, we are essentially comparing what is predicted by the [SM](#) to what is measured by experiment. If the two differ in ways not explained by simulation error or other non physics related errors, one could interpret the deviation as a new physics.

To summarize, a search for new physics, is a search for deviation between simulation and experiment. At first thought, this might seem like a simple task. And if said deviation was large, it would be easy. In reality, any new physics which predicts large contributions in the data currently measured by [ATLAS](#) has been excluded a long time ago. Today, any promising extension of the [SM](#) predicts to contribute rarely in any detector. As will be presented in later section, some theories that will be searched for in this thesis, only contribute to a total of 6 events in a data set consisting of more than 3800000 events ($< 0.002\%$). Not only would such a deviation be incredibly hard to detect, but it would be close to impossible to determine if such a deviation is rooted in new physics or simply noise.

The traditional approach to this problem, is to study the data in physics motivated regions. For example, in section 1.6 I presented the Feynman diagrams of the signals I searched for in this thesis. As mentioned, this type of final state is expected to exhibit large amounts of missing transverse energy¹⁸. The traditional approach is to neglect all the data with small amounts of missing energy, and only consider events of interest. By applying these kinds of constraints on the data, you are creating a region where you expect to find as much of the signal as possible and as little of the background. After applying a sufficient amount of demands (or cuts), you would count the remaining data in your *search region* and check for deviation. This approach is called Cut-and-Count ([CC](#)).

2.8.2 The Machine Learning Approach

For a signal which greatly differs from the [SM](#), the [CC](#) method could be sufficient. But, in cases where the signal is similar to background, it becomes harder to create effective¹⁹ cuts. In figure 2.9, I have drawn an illustration of two different feature distributions both displaying the distribution for a hypothetical signal and background. Additionally, I have drawn a threshold in both distributions which represents the cut made

¹⁸Due to the neutralinos being both heavy and neutral.

¹⁹By effective cuts I mean cuts which removes large amounts of the background while at the same time preserves as much of the signal as possible.

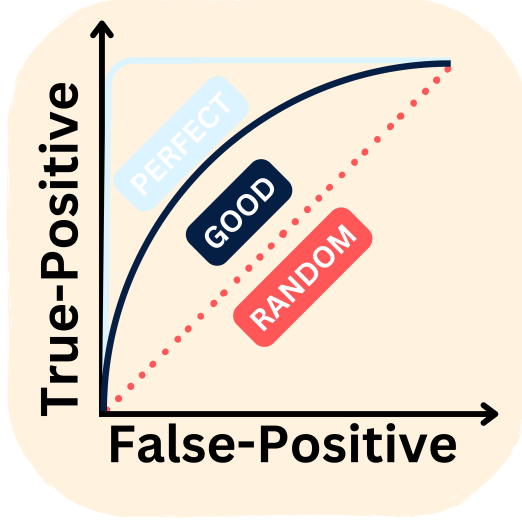


Figure 2.10: An illustration of a ROC curve.

to create a search region. In the first figure (left) the distributions of signal and background are relatively similar, and the signal region contains large amounts of background. In the second (right), the distributions of signal and background are greatly different, and this variable would allow for a much more effective signal region.

The goal of introducing **ML**, is to create a new feature in the data set where background and signal exhibit as little overlap as possible. This is very similar to how we introduce physics motivated high-level features like $H_t(l\bar{l})$ or $M_l l\bar{l}$, but instead of using an analytical function grounded in physics, we apply the output of a trained **ML** model. Then, once the **ML**-variable is created, we apply a cut (similar to **CC**) which will define an effective search region.

How we create the **ML**-variable can vary depending on the type of **ML**. In the case of unsupervised **ML**, one aims to perform a type anomaly detection. One unsupervised approach is to overfit on the background, then hope that said overfitting is reflected when a new process is introduced. An effective unsupervised approach would be incredibly beneficial, as it would be totally model independent. In other words, the same model could be applied to all signal. As mentioned in earlier sections (see section 2.1), the focus of this thesis will not be on unsupervised **ML**, but supervised. The largest difference between the two is the introduction of an additional data set, the signal. By simulating and training on what we expect the new physics to look like, we are able to achieve a much more effective output, but the output would be tailored to the signal it's been exposed to and not much else²⁰.

2.9 Model assessment

2.9.1 The Rate of True-Positive - ROC Curve

A Receiver Operating Characteristic (**ROC**) curve is a tool used to measure and visualize a binary classifiers' ability to predict trends. In figure 2.10 I have plotted an illustration of a **ROC** curve. The curve is plotted on an x-, y-axis where the x-axis represents false-positive rates and the y-axis represents true-positive. The different values for the curve are the rate of true positives with different thresholds, i.e. the value deciding whether an event is 1 or 0, signal or background. If a classifier has learned nothing and is simply guessing, the **ROC** curve will be a linear curve going from 0 to 1. This line is often drawn in **ROC** curve. The better the classifier is, the higher the **ROC** curve will bend towards the upper-left corner of the graph. The worse it is, the more it will bend to the lower right corner.

A metric often used to measure a classifiers' ability to create an output which effectively separates two categories, is the Area Under the Curve (**AUC**). The higher the area, the larger the separation. An ideal classifier which perfectly separates two categories will achieve a **AUC** of 1. A classifier which simply guesses, will achieve an **AUC** of 0.5. Both these cases assume an equal weighting of both signal and background.

²⁰Except for overlapping signals or models which are able to interpolate between regions.

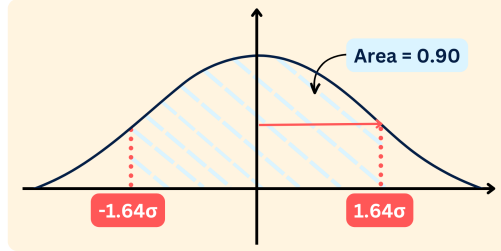


Figure 2.11: An illustration of a Gaussian distribution and the area under the curve defined by a significance equal to 1.64.

2.9.2 Statistical Assessment - Discovery & Exclusion

The statistical aspect of the analysis will not be of focus in this analysis, nonetheless there are some expressions which would be helpful to define. Let us assume that we expect to see no new physics in the collision data, we can call this hypothesis the b(background)-hypothesis. To expect no new physics, is not the same as expecting no deviation between SM simulations and experiment. We still assume a statistical uncertainty, or noise to effect the simulations which will lead to some deviations. If these deviations are random, we can assume that the noise can be described as sampling from a Gaussian distribution (which is a good approximation for large statistics), which has a mean of 0 and a standard deviation equal to \sqrt{b} , where b is the number of SM simulations. Using this assumption, we can state that the higher the deviation between the two, i.e. the further away from the mean, the less likely such a deviation is explained by our b-hypothesis. Given a large enough deviation, we can even define the hypothesis as rejected.

We measure the deviation between the observed collision data and the simulated SM data in units of significance, Z. For a given signal region with n_{obs} events of measured collision data and b simulated SM data, we define the significance of a deviation as

$$Z = \sqrt{2 \left[n_{obs} \ln \frac{n_{obs}}{b} - n_{obs} + b \right]} \text{ or } Z = \sqrt{2 \left[(s+b) \ln \left(1 + \frac{s}{b} \right) - s \right]}, \quad (2.17)$$

where we have defined the signal, s as $s = n_{obs} - b$. In the case of large statistics ($b \gg s$), we can write Z as

$$Z = \frac{n_{obs} - b}{\sqrt{b}} = \frac{s}{\sqrt{b}}. \quad (2.18)$$

By studying equation 2.18 we observe that the significance of a deviation, is simply the signal measured in units of standard deviation of the Gaussian distribution. In physics, one often deems the results a discovery, or the b-hypothesis as rejected if Z is larger than 5.

In the case we are not interested in discovering physics, but simple to measure the sensitivity of a model, we can also use significance. In this case we do not have n_{obs} . Instead we simply define s as the number of events for the simulated signal inside the signal region. This number would be specific for each mass combination and will be a measure for how sensitive the model is for that exact combination. In physics, we define a model as sufficiently sensitive, if it is able to achieve a significance of 1.64. This number is chosen based on its relation to the b-hypothesis. A significance of 1.64, equals the distance from the mean of the Gaussian distribution which sums to an area of 0.90 (see figure 2.11). There are many ways to interpret this. A layman interpretation (which is sufficient for this thesis), is that given the b-hypothesis is true, there is a 90% probability that we will measure a signal which produces a significance of less than 1.64. Therefore, there is only a 10% probability that the b-hypothesis can explain the deviation. For more information on significance and discovery in physics the reader is referred to the slides [22].

Chapter 3

Implementation of the Analysis

3.1 Tools and Data

Every year technology for generating and measuring particle collisions is improving. As a consequence, the amount of data increases drastically. The ATLAS experiment is one of the largest particle detector experiments currently operating at the CERN laboratory near Geneva. ATLAS alone generates approximately 1 petabyte of raw data every second from proton-proton collisions at the LHC. With amounts of data this large, data handling and storing is a big challenge. Therefore, taking advantage of sophisticated numerical tools and data frameworks is pivotal if scientific development is to keep up with technological development. In this section I will cover some tools and frameworks I have used to complete my analysis. Large amounts of details and explanations will not be covered. Instead, this section will highlight which tools were used and some motivation for choosing them. Additionally, I will cover some details regarding the data being used, both MC-simulations and real collision data.

3.1.1 Monte Carlo Data

Up to this point in the thesis, I have discussed two data sets: the measured collision data and the simulated data. As far as my relation to the latter data set, I have only used it directly in my analysis and have not been involved in production. The simulations applied in the creation of our simulated data set are all based on Monte Carlo (MC) simulations²¹, produced by the popular framework INSERT WHICH ONE. Through simulation, we are able to (among other things): test our understanding of the detector, model the expected SM background events in different regions or model new BSM physics. The pipeline for producing simulated events, closely mimic the pipeline from real collision to data set. The pipeline for simulating collision events can be summarized in the following steps

- **Generate events:** Simulate each event in the collision, marking each event with the corresponding process (see section 1.5)
- **Simulate detection of events:** Simulate the detection of each event in the different layers of the detector described in section 1.4.1
- **Digitization:** Translate the interaction between the events and the detector to real signals
- **Reconstruct events:** Go through the same steps applied to real collisions to reconstruct particles from signals

3.1.2 ROOT, RDataframe and Pandas

ROOT [24] is at its core a large C++ library and data structure made specifically for big data analysis and computing, as well as data visualization. Today, all ATLAS data is stored as a ROOT-file along with more than 1 exabyte (10^{12}) of data worldwide. ROOT has many High Performance Computing (HPC) qualities which makes it ideal for particle physics analysis which demands heavy computations. Additionally, many particle physics-specific packages have been developed to make it an even better tool. Any function not already in library, can easily be added in a HPC-effective manner through C++.

All distribution plots made for this thesis were created using ROOT. ROOT has implemented a highly intuitive and effective Application Programming Interface (API) for data comparison and visualization.

²¹For more information on MC simulation, the reader is referred to [23].

ROOT allows for quick and direct comparison between data through an advanced graphical user interface. Additionally, a lot of functionality for creating complex stacked histogram are implemented in the ROOT API, such as uncertainty calculations, ordering of histograms and statistical analysis tools.

As for the data structure, the raw data was loaded as a ROOT-file. To easier handle the data and add new features, I used the RDataFrame structure [25]. RDataFrame allows for easy addition of new columns as well as filtering of events through native functionality. As a consequence I used RDataFrame to calculate all higher-level features such as the transverse mass (M_{T2}), invariant mass of 3 leptons (M_{lll}) etc. An example is shown in the following section.

After all data handling was complete, I used ROOT's *AsNumpy* function to translate the data frame as a numpy object, which then allowed me to transform it to a Pandas-data frame [26]. This is done because Pandas, like most ML-tools work in a strict Python environment. Pandas, similarly to RDataFrame includes many deep computational libraries, and is optimal for analysis of big data. When the full ML pipeline (data-handling, training, validating etc.) is completed, the data is transformed back to RDataFrame, to take advantage of the plotting functionality in ROOT.

3.1.3 Computing features in ROOT: Example

In this section I will cover a simple example to highlight the steps taken in generating the dataset I used in the analysis. As mentioned earlier, the two main frameworks used were RDataFrame and Pandas. In this example I will cover the case of a feature not already in the ROOT file, namely the trilepton invariant mass. All loading of data is done using the ROOT framework and is quickly transformed into a RDataFrame. To effectively generate new features, we want to stay in ROOT and RDataFrame. Therefore, we create our C++-file, *helperfunction*. The helperfunction contains all additional ROOT functions that are used in the analysis and are not already native to ROOT. In the case of computing the trilepton invariant mass, the C++-function is created like shown in listing 3.1.

In listing 3.1, we see a couple of measures taken to uphold to the ROOT environment. The first is the typecasting to *VecF_t*. *VecF_t* is created to wrap floats in the native ROOT vector object, *RVec*. The same is done in other cases such as float and integers, *VecI_t* and *VecB_t*. The second measure was using *TLorentzVector* [27] to calculate the invariant mass. *TLorentzVector* is a class native to ROOT with many built-in functions. In this case we use the class to create three vectors through the variables, P_t , η , ϕ and M . Then, through the *TLorentzVector* class we can simply add all three vector together, and extract the invariant mass of the 3 leptons.

```

1 // Compute the trilepton invariant mass
2 float ComputeInvariantMass(VecF_t& pt, VecF_t& eta, VecF_t& phi, VecF_t& m) {
3     TLorentzVector p1;
4     TLorentzVector p2;
5     TLorentzVector p3;
6     p1.SetPtEtaPhiM(pt[0], eta[0], phi[0], m[0]);
7     p2.SetPtEtaPhiM(pt[1], eta[1], phi[1], m[1]);
8     p3.SetPtEtaPhiM(pt[2], eta[2], phi[2], m[2]);
9     return (p1 + p2 + p3).M();
10 }
```

Listing 3.1: C++-function for M_{lll} .

With a helper function created in C++ we can move over to a Python and RDataFrame environment for calculation and plotting. In the code written in listing 3.2, I have shown a simple example of loading new C++-functions, filtering out bad events, calculating new features and adding said features to a histogram. The first three lines of code both process and include the helperfunctions into the ROOT framework. Then I loop over all keys in the data frame, which in my case are the different channels (i.e Diboson, $t\bar{t}$ etc.). For each channel I select 'good' events, based on the criteria from section 3.2.1. Then, I use RDataFrame's *Define* function to calculate and add a new feature using our *ComputeInvariantMass*-function. Finally, I save the feature as an *Histo1D* object, which I plot later using ROOT plotting API's.

```

1 R.gROOT.ProcessLine(".L helperFunctions.cxx+");
2 R.gInterpreter.Declare('#include "helperFunctions.h"')
3 R.gSystem.Load("helperFunctions.cxx.so")
4
5 for k in df.keys():
6     # Define good leptons
7     isGoodLepton = "feature1 < cut1 && feature2 >= cut2"
8
9     # Define good leptons in dataframe
10    df[k] = df[k].Define("isGoodLepton", isGoodLepton)
11
```



Figure 3.1: A visual summary of the workflow and framework use for the computational analysis.

```

12 # Define number of good leptons
13 df[k] = df[k].Define("nGoodLeptons", "ROOT::VecOps::Sum(isGoodLepton)")
14
15 # Demand 3 good leptons
16 df[k] = df[k].Filter("nGoodLeptons == 3")
17
18 # Define Invariant Mass (l1l1)
19 df[k] = df[k].Define("mll1", "ComputeInvariantMass(lepPt[isGoodLepton],
20                      lepEta[isGoodLepton],
21                      lepPhi[isGoodLepton],
22                      lepM[isGoodLepton])")
23 # Add to histogram
24 histo["mll1_%s"%k] = df[k].Histo1D(("mll1_%s"%k,
25                                         "mll1_%s"%k, 40, 50, 500),
26                                         "mll1",
27                                         "wgt_sg")

```

Listing 3.2: Python-file for calling dataframe and calculating M_{lll} .

In this example I chose the trilepton invariant mass, but in the analysis all high-level features were calculated using a similar method. The workflow of the method is visualized in figure 3.1. We load data in ROOT format, data handling and plot feature distribution in RDataFrame, perform ML- analysis in Pandas and plot results in RDataFrame.

3.1.4 The Signal

As I have mentioned in previous sections I will be searching for a large range of signals, all related to the same physics, but with different set of parameters. In figure 3.2 I have drawn a grid showing the different mass combinations searched for in this analysis. The figure shows the data set containing masses ranging from $M_{\tilde{\chi}_1} \in [0, 400]$ and $M_{\tilde{\chi}_2} \in [100, 800]$. In the beginning of my analysis I only received a subset (which will be referred to as the *original* data set.) of the full signal set. In the figure I have marked the original data set with a white label in the top right corner of the box. In the first data set I received (which will be referred to as the *original* data set.) there are a total of 30 different mass combinations in the range from $M_{\tilde{\chi}_1} \in [0, 400]$ and $M_{\tilde{\chi}_2} \in [400, 800]$. In the full signal data set there are a total of 90 different mass combinations.

Given that I received the original signal data set many months before receiving the full set, most of my results were found using the original set. Therefore, I choose to use the original data set to compare the models in performance, then finally use the full set when aiming to either exclude or discover new physics.

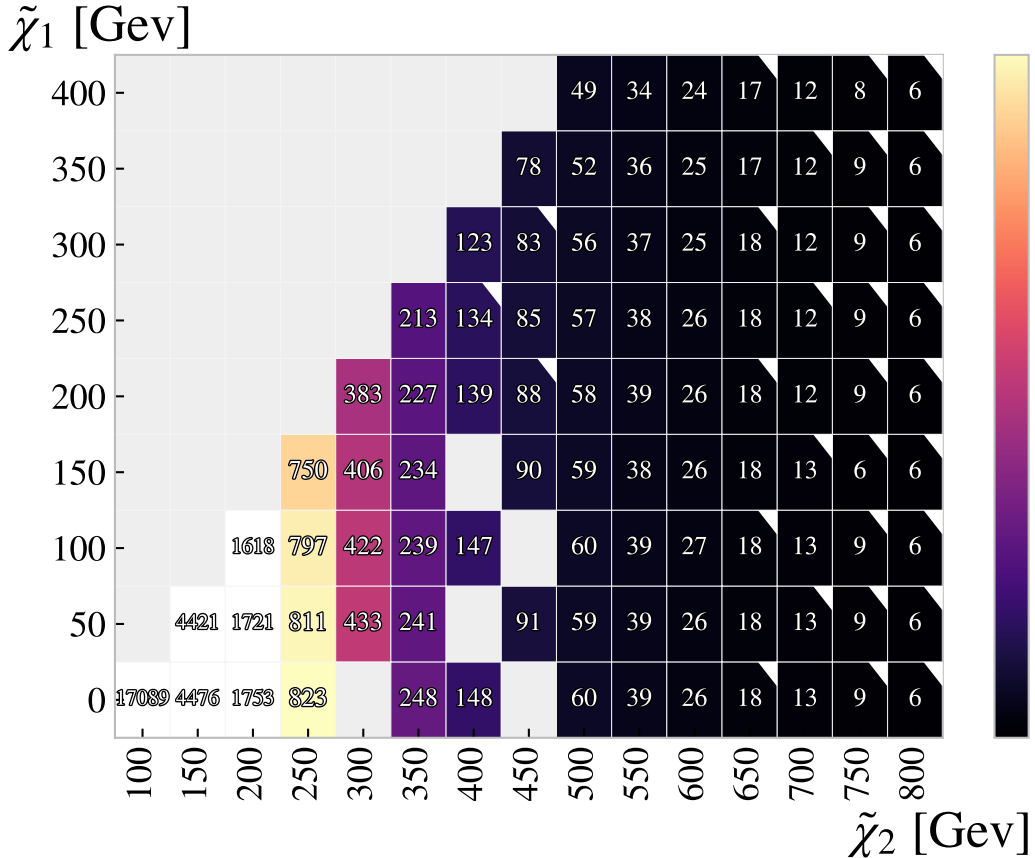


Figure 3.2: A depiction of all mass combinations in the full signal data set.

3.2 Features

The choice of which features to study and which to neglect is crucial in a search for new physics. This is particularly true in the case of applying machine learning. The general motivation for including a given feature can be based on several factors. The first being its ability to provide a trend which we as researchers can exploit when creating our signal search regions. By this I mean that it is a variable where there is diversity in distribution between the different channels. The second motivation is grounded in physics. Often we as physicists tend to lean towards variables we know have some effect on the physics we are studying. For example the missing transverse energy, E_T^{miss} can be directly used to either include or discard events where we do or do not expect final states with sufficient missing energy. The final motivation is grounded in the **MC**-simulations ability to represent the variable. If there seems to be a clear deviation between the real and **MC**-data which does not stem from any new physics, we tend to discard them from the analysis.

3.2.1 Cuts and triggers

To allow for deep learning and a thorough analysis one must try and keep as much of the data as possible. At the same time, including large amounts of irrelevant data can be both redundant and destructive²². Therefore, preselection cuts are necessary. The cuts applied in the analysis were grouped in two definitions, baseline and signal. The baseline requirements are written in table 3.1 and the signal requirements are written in table 3.2. Both sets of requirements were taken from the ATLAS article from 2022 [28]. Given the definitions we demand that each event contains exactly three signal (3.2) and three baseline leptons (3.1), thereby removing any event with more or less.

Leptons are identified in the detector by using a likelihood-based method combining information from different parts of the detector. The criteria of Loose or Tight identification are simply different thresholds in the discriminant, where Loose is defined as a lower threshold than Tight [29]. The overlap removal is

²²By including large amounts of irrelevant data, you risk the **ML**-model tuning unnecessarily to remove easily reducible background, which could compromise performance on irreducible background.

Requirement	Baseline electrons	Baseline muons
Identification	—	Loose
Overlap Removal	lepPassOR	lepPassOR
$\eta - \text{cut}$	$ \eta < 2.47$	$ \eta < 2.7$
$ z_0 \sin(\theta) \text{ cut}$	$ z_0 \sin(\theta) < 0.5 \text{ mm}$	$ z_0 \sin(\theta) < 0.5 \text{ mm}$

Table 3.1: Requirements for baseline electrons and muons.

Requirement	Signal electrons	Signal muons
Baseline	yes	yes
Identification	Tight	—
Isolation	LooseVarRad	LooseVarRad
$ d_0 / \sigma_{d_0} \text{ cut}$	$ d_0 / \sigma_{d_0} < 5.0$	$ d_0 / \sigma_{d_0} < 3.0$

Table 3.2: Requirements for signal electrons and muons.

used to solve any cases where the same lepton has been reconstructed as both a muon and an electron. The boolean of *lepPassOr* simply applies a set of requirements to avoid any double counting. The cut for the longitudinal track parameters, z_0 is applied to ensure that the leptons originate from the primary vertex. As for the requirements for the signal leptons, we require all baseline requirements are passed with the addition of a few more. We require Loose isolation for both electrons and muons. This means requiring isolation criteria for a cone around the lepton is used to suppress QCD-background events and reduce fake leptons. Similarly to the z_0 -cut, the transverse track parameter is also used to ensure origin from primary vertex. In addition to the simple cuts, we must insure a good comparison between MC- and real data. Often one finds large deviation between the two in the case of either very large or very small transverse momentum, P_t . The latter case can often be caused by poor reconstruction or miss identification. These are issues we aim to solve by checking different triggers.

In the earlier parts of the analysis, I discovered that the data set I was given, did not contain the correct information regarding the triggers. After spending some time trying to compensate for this, my Supervisor (Eirik Gramstad) suggested an alternative. Instead of filtering using the triggers, an additional criterion of at least two leptons containing $P_t > 20\text{Gev}$ was placed on the data, as it was suggested that this would be relatively equivalent.

3.2.2 Lepton Variables

Now we will have a look at lepton variables that were included in the analysis. All low level information on the momentum of the leptons were added into the dataset: i.e. the transverse momentum P_t , the pseudo rapidity η and the azimuth angle ϕ . All momentum features were represented individually for each lepton. For example P_t was added as three columns, $P_t(l_1)$, $P_t(l_2)$ and $P_t(l_3)$, where the ordering of the leptons were based on the momentum from highest (l_1) to lowest (l_3). Similarly, I added information regarding the charge (\pm) and flavor (electron, muon) of each lepton. Based on the momentum variables the transverse mass m_t of each lepton was calculated and included along with the energy E_t^{miss} and azimuth angle ϕ^{miss} of the missing transverse momentum.

The variables described in the section above are often considered as low-level features. These are very useful in many (if not all) searches and contribute little to no bias to your analysis. But, in the case of final-state specific searches such as this, one can allow one self to add physics motivated higher-level features. The higher level features used in this thesis were inspired by the publication of ATLAS in 2022 [28].

Firstly I added different mass variables, namely m_{lll} and $m_{ll}(\text{OSSF})$ (Opposite Sign Same Flavour (OSSF)). The first being the trilepton invariant mass and the latter being the dilepton invariant mass of the pair with OSSF. In the case of more than one possible OSSF-pair, the pair with the highest invariant mass was chosen. Secondly I added variables composed of the sum of different set of momenta. These variables are the sum of all three leptons $H_t(lll)$, of the pair with Same Sign (SS) $H_t(SS)$ and the sum of the momentum for all three leptons added with the missing transverse energy $H_t(lll) + E_t^{\text{miss}}$. Finally, I added the significance of the E_t^{miss} , $S(E_t^{\text{miss}})$.

3.2.3 Jet Variables

Now we can have a look at the jet-features. Given the final-state of interest should be independent of jets, there are not many features added with jet information. But, given the risk of miss identification and errors

	Feature	Reference
	$\phi(\text{miss})$	34b
	M_{lll}	34c
	$M_{ll}(\text{OSSF})$	34d
	Sig E_T^{miss}	33a
	$H_t(\bar{l}l)$	34f
	$H_t(SS)$	35a
	$H_t(l\bar{l}) + E_T^{\text{miss}}$	35b
	ΔR	34a
	Nr of signal Jets	35c
	M_{jj}	35d
	Nr of B-jets(77)	35e
	Nr of B-jets(85)	35f
Feature	l_1	l_2
p_t	—	31b 31a
η	—	31c 31d
ϕ	32a	32b 32c
M_T	32d	32e 32f
Charge	33a	33b 33c
Flavor	33d	33e 33f

(a)

(b)

Figure 3.3: References to figures for all event specific feature distribution.

in reconstruction, some features were added. The first features were the number of jets, both all signal jets and number of b-jets. The latter information was divided in two columns based on the efficiency of a multivariate analysis used to separate jet-flavors. The efficiencies used for b-tagging are 77% and 85%. The last information added for the jets were the mass of the leading pair (based on p_t di-jet mass, m_{jj}).

3.2.4 Validation

As mentioned in previous sections, the comparison between **SM MC** and real data is a crucial part of the analysis, and we must therefore insure an adequate reconstruction of the real data before we begin the analysis. This is not only true for the low-level features, but for all features used in the analysis to create a new **ML** variable. Therefore, we will in this section compare both sets of data for all features included in the analysis. In figure 3.4, I have drawn the event distribution for the P_t (3.4a) and η (3.4b) for the leading lepton, as well as the E_T^{miss} (3.4c) and flavor combination (3.4d) of the final state. The error bars in each bin are set by default to (#events per bin). The distribution of the remaining features have been added in the appendix A.2.1. I have added two tables with references to each feature not in the main thesis, in the case the reader is interested in studying specific features. Table 3.3a contains all lepton specific features and table 3.3b contains all event specific features.

Under each figure I drew the ratio between the measured collision data and the **MC** for each bin. By studying the ratio-plots for each figure we observe that the ratio for all bins for all features are between 1.2 and 0.8. Most bins even lying closer to 1. The bins displaying the largest errors are in the higher P_t -range. This is exemplified in figures 3.4a and 3.4b²³.

In the P_t figures we can observe that for (relatively) small P_t ($< 100\text{GeV}$) all events lay well within a range of [0.9 – 1.1] ratio. Whereas for higher P_t ($> 200\text{GeV}$), the errors move closer to a range of [0.8 – 1.2] ratio. The difficulty of simulating **SM** processes in high P_t range is a known phenomenon, and not specific to this analysis. Thankfully, a smaller portion of the data lays in the high P_t -range and therefore most of the simulation exhibits a solid comparison to measured data. By studying the figures in the appendix A.2.1, we can deduce that this trend continues thought the full feature set. Additionally to studying the ratio for each features in different bins, we can read from the labels that there are a total of 381873 measured collisions in the data, compared to 381860 simulated events. Simply put we observe that the **MC** seems to adequately imitate the trends of the observed data for all features used in the analysis.

Apart from the excellent agreement between observed and simulated data, we can note a couple of other expected but interesting points. The first being the size of each channel. $Z - \text{jets}$ is by far the largest channel followed by the *Diboson(l_{lll})*. Although $Z - \text{jets}$ is the largest channel, by comparing the Feynman-diagrams of each channel (section 1.5), *Diboson(l_{lll})* should be the hardest background to separate due to the similarities in the final-states of the signal²⁴. Another point of interest is the differneces in distribution between the different **SM** proccesess as displayed by the simulated data. By studying the P_t in figure 3.4a, we observe that some channels exhibit a distribution peak for low P_t (ca. 50 GeV) and then rapidly drop for higher values. This is the case for $Z - \text{jets}$ and *Dibson(l_{lll})*. On the other hand some processes seem to have a much slower decrease in distibution. This is true for *Diboson(l_{lll})*, *Top – Other* and $t\bar{t}$. The exact same trend

²³Due to η 's dependence on the polar angle (see equation 1.1), the larger the P_t the higher the absolute value of η

²⁴I.e. *Diboson(l_{lll})* has a 3 lepton final state with large missing energy.

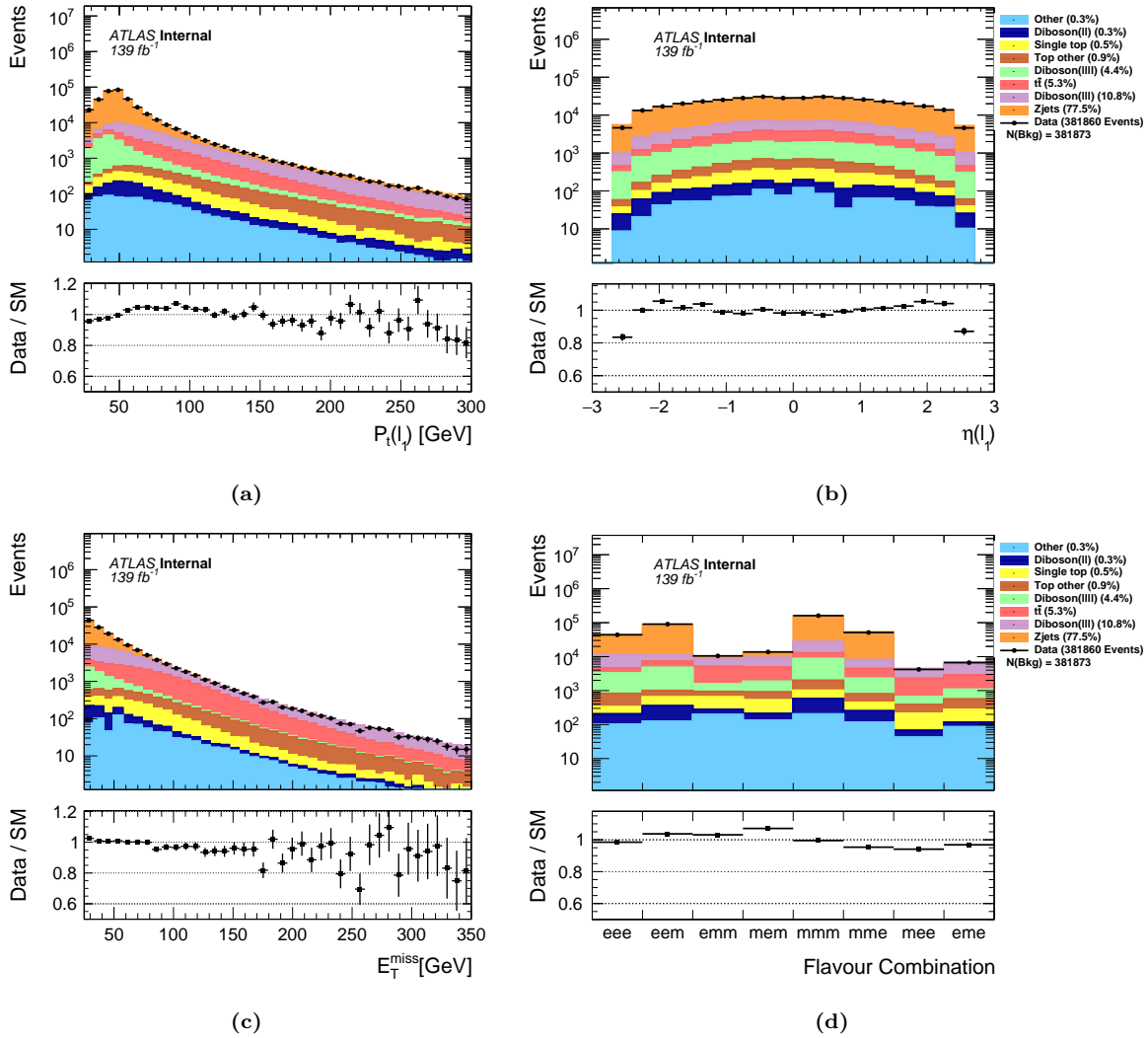


Figure 3.4: MC and real data comparison and event distribution for each channel over P_t 3.4a and η 3.4b for the first lepton. Similarly, the distribution over the E_T^{miss} 3.4c and flavor combination of the three leptons 3.4d.

is true also for E_T^{miss} , where $Z - \text{jets}$ and $\text{Diboson}(llll)$ rapidly drop for high values whereas $\text{Diboson}(lll)$, $\text{Top} - \text{Other}$ and $t\bar{t}$ decrease much slower. High amounts of missing energy is an indicator that $\text{Diboson}(lll)$, $\text{Top} - \text{Other}$ and $t\bar{t}$ could deem hard to separate from our E_T^{miss} heavy signal.

3.2.5 Negative Weights

The negative weight problem is a well known problem in the world of ML-analysis for HEP, and is a consequence of higher perturbative accuracy. For the purpose of visualizing distributions and training a NN, negative weights are not a problem. But, when using the weights in the training of the XGBoost classifier, the algorithm does not work²⁵.

Before deciding how to mediate the issue, I decided to plot the distribution for a small subset of features for all the events with negative weights. In figure 3.5a and 3.5c I plotted the distribution of the leading lepton for the features P_t and ϕ , but only including events with negative weights. Additionally, I drew the distribution for the full data set for the same features. By comparing the distributions, we can observe that the full data set and the negative weights' subset are very similar. There are differences in distributions when comparing the SM individually, but when studying the background as a whole, the two sets exhibit the same trend across all regions. This means that the negative weights essentially scale the background uniformly over the full feature space, which motivates treating the negative weight problem uniformly over the full feature space. How one chooses to deal with this problem can heavily effect results and many solutions are suggested as

²⁵Upon further research in the codebase of XGBoost, it seems as though negative weights are not allowed as it interfere with XGBoost's use of the hessian matrix. Due to time constraints, I decided not to pursue this further.

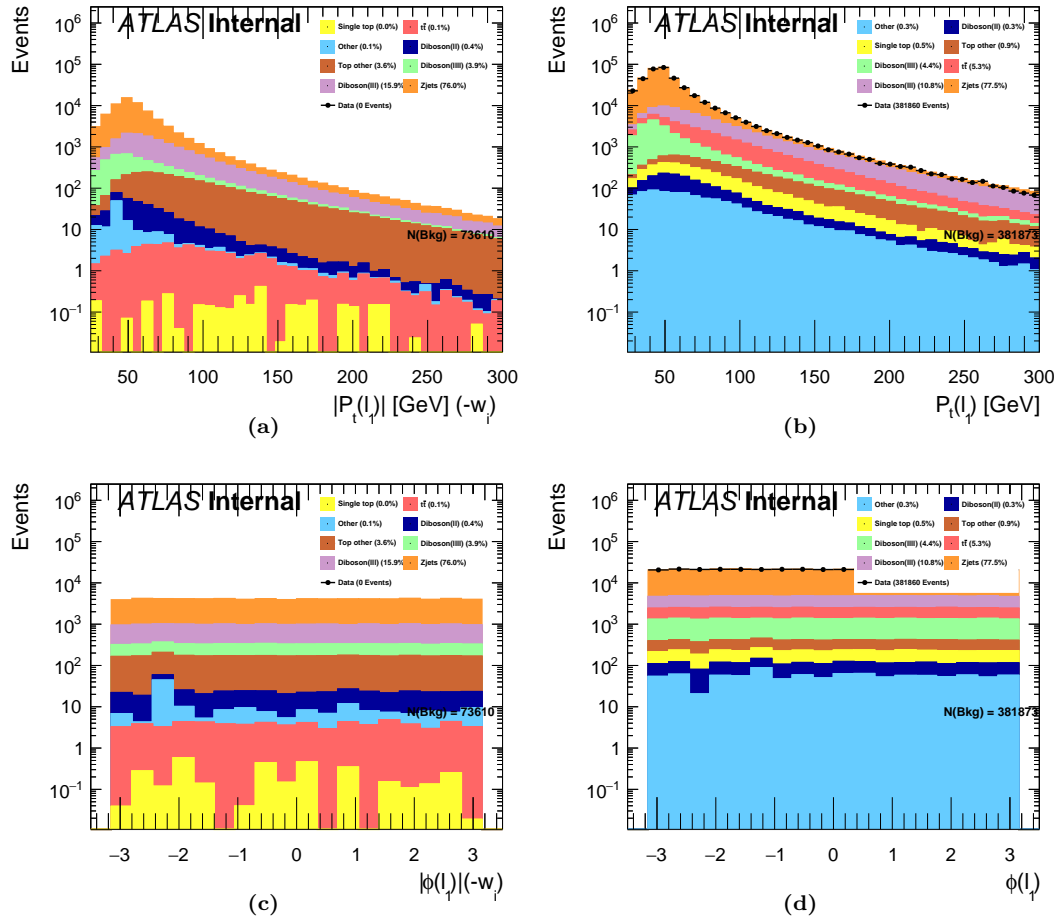


Figure 3.5: The event distributions of the leading lepton for the features P_t and ϕ . Figures 3.5a and 3.5c display only the events with negative weights (for P_t and ϕ respectively) whereas 3.5b and 3.5d show the full data set.

a consequence. Given the main focus of this rapport, the simplest solution was chosen. The solution was motivated by the internal notes of the ATLAS article [30], who introduced the solution when faced with the same problem. The solution is to take the absolute value²⁶ and normalize all the weights, conserving the total sum of the weights and at the same time changing all negative signs. The simple procedure is shown bellow in equation 3.1,

$$w_i = P | w_i | \quad (3.1)$$

$$P = \sum_{j=0}^{N-1} \frac{w_j}{| w_j |}, \quad (3.2)$$

where w_i is the weight of an event i , $i \in [0, N - 1]$ and N equals the total number of events.

3.3 The Machine Learning Models

3.3.1 Model selection

In this analysis I have chosen to compare 4 different "types" of **ML**-models, ordinary dense Neural Network (**NN**), Parametrized Neural Network (**PNN**), ensemble and Boosted Decision Trees (**BDT**). The first three methods are all types of **NN**. I have deliberately chosen to focus on **NN** given that there is far more freedom in the design of the architecture of a **NN**, than compared to a XGboost. Additionally, this was motivated by the selfish reason being that I found the networks more interesting to study and dissect. Therefore, most of the analysis, comparisons and discussion is focused on the networks, while XGBoost is included as a loose benchmark.

The choice of the three network architectures is motivated in wanting to compare a simple deep network, a network ensemble and a **PNN**. I would assume that the optimal architecture would be a network which combines elements from each, but for the purpose of discussion and research I have chosen to keep them somewhat separate.

3.3.2 Creating custom layers

The field of **ML** is one of the most dynamic and fastest growing fields of research today. This means, that regardless of the brave attempt made by voluntary contributors and the people at Google²⁷, there will always be new and exciting **ML** tools and algorithm, not yet implemented in their library. This was certainly the case in this thesis. For several of the non-dense layers I was forced to dive into the world of **ML** development and create my own implementation.

All ensemble methods described in section 2.6.5 (except for dropout), channel-out, **SCO** and maxout, resemble a layer already implemented by Tensorflow. This layer is called MaxPooling1D²⁸. But, to allow for experimentation I decided to not use MaxPooling1D, but instead implement my own custom layers. All custom layers were implemented by creating new functions inside TensorFlow's dense layer, which are called when the network makes a prediction. In the following sections I will describe the algorithms underlying the implementation of each layer.

Channel-out

In algorithm 1 I summarized the implementation of channel-out used in this analysis. For each input which is to be passed through a forward-pass, the function first passes it through the weights and biases as described in section 2.6.2. This is true for all the other layers as well. In line 7 I reshape the input to add a dimension which creates the units. In line 10 I create a new variable, *Output* by reducing each unit to the largest activated node. Further I set each node to 0 which is not equal to the largest activation. Finally, I reshape the output to the original shape and return the output.

SCO

In section 2.6.5 I described how **SCO** is an extension of channel-out. This is certainly also the case for the algorithms explaining the implementation. In algorithm 2 I have described algorithm used in the

²⁶Thereby removing all negative weights.

²⁷The developers of TensorFlow

²⁸For more information on MaxPoolind1D, the reader is referred to the documentation (https://www.tensorflow.org/api_docs/python/tf/keras/layers/MaxPool1D, accessed 24.03.2023).

Algorithm 1 The pseudocode for implementing the channel-out layer in TensorFlow

```

1: def Channel-out(Input):
2:   % Pass input through weight kernel and adding bias terms.
3:   Input  $\leftarrow$  Input  $\times$  Weights
4:   Input  $\leftarrow$  Input + Bias
5:
6:   % Reshape input into units
7:   Input  $\leftarrow$  Reshape(Input, (Nr Units, Size of Units))
8:
9:   % Reduce input to the largest activation in each unit.
10:  Output  $\leftarrow$  Max(Input)
11:
12:  % Set original activation where activation is largest and 0 where it's not.
13:  Output  $\leftarrow$  Where(Input == Output, Input, 0)
14:
15:  % Reshape to original size.
16:  Output  $\leftarrow$  Reshape(Output, (Input's Original Shape))
17:  return Output

```

implementation of **SCO** in this analysis. Similar to channel-out, the algorithm begins by passing input through weights and biases. Then, contrary to channel-out the nodes of the input are shuffled. This is to ensure that when the input is reshaped (in line 10), the units are made differently for each pass through the function. Again the maximum activation is found to create a new variable, this time called *OutputShuffle*. In line 16 *InputShuffle* and *OutputShuffle* are compared such that where *InputShuffle* is equal to the largest activation, the value is set to 1 and otherwise set to 0. *OutputShuffle* is then unshuffled, and reshaped to the original shape. Finally, the input which has been passed through the weights and biases, is multiplied with *Output* and returned.

Max-out

In algorithm 3 I have summarized the algorithm behind the implementation of the maxout layer. Off the three layers (channel-out, **SCO** and maxout), maxout was the simplest to implement. After passing the input through the weights and biases and reshaped to form the units, the input is reduced to only include the largest activation in each layer. Finally, the output is reshaped to the original shape and returned.

3.3.3 Model Architecture

When choosing a network architecture, there are several ways to proceed. One way is to apply a grid search. A grid search is simply defining a grid of parameters to test, then running through all combinations and choosing the highest performer. With a sufficient amount of tests, a grid search should converge towards an optimal architecture. Grid search is very common and there exists a large range of very complex varieties [31]. For my analysis I chose not to perform a grid search, for several reasons. The first being interpretability. Understanding a **NN** is already hard, allowing for complex and unique architectures would only add another layer of mysticism. The second is the size of the data set. The larger the data set, the larger the amount of data would be needed to adequately perform tests for each combination of parameters. Not only is this time-consuming, but trying to mediate this issue could lead to poor performance. The third and most important reason is that I wanted to experiment with the architectures. By manually tuning the parameters, I was able to achieve a far better understanding of the final architecture.

Dense Neural Network and PNN

The purpose of the simple dense **NN**, is to compare the more complex networks to what is usually considered an ordinary dense **NN**²⁹. All layers are dense layers, meaning that all nodes in the previous layer are connected to the current layer, and likewise the current layer is connected to the next. The general structure of the network is summarized in figure 3.6, with the network label **NN**. The figure shows a dense **NN** with three hidden layers, all with 600 nodes each. All hidden layers utilize the *LeakyReLU* activation (see section

²⁹Note that for the remaining part of this thesis, I will refer to this architecture as a 'dense **NN**', 'ordinary dense **NN**' and in some plots, just **NN**

Algorithm 2 The pseudocode for implementing the SCO layer in TensorFlow

```

1: def SCO(Input):
2:     % Pass input through weight kernel and adding bias terms.
3:     Input  $\leftarrow$  Input  $\times$  Weights
4:     Input  $\leftarrow$  Input + Bias
5:
6:     % Shuffle all the values
7:     InputShuffle  $\leftarrow$  Shuffle(Input)
8:
9:     % Reshape input into units
10:    InputShuffle  $\leftarrow$  Reshape(InputShuffle, (Nr Units, Size of Units))
11:
12:    % Reduce input to the largest activation in each unit.
13:    OutputShuffle  $\leftarrow$  Max(InputShuffle)
14:
15:    % Set 1 where activation is largest and 0 where not.
16:    OutputShuffle  $\leftarrow$  Where(InputShuffle == OutputShuffle, 1, 0)
17:
18:    % Un-shuffle all the values
19:    Output  $\leftarrow$  UnShuffle(OutputShuffle)
20:
21:    % Reshape to original size.
22:    Output  $\leftarrow$  Reshape(Output, (Input's Original Shape))
23:
24:    % Multiply input with output to set all input that are not the largest, to zero.
25:    NewOutput  $\leftarrow$  Input  $\times$  Output
26:
27:    return NewOutput

```

Algorithm 3 The pseudocode for implementing the maxout layer in TensorFlow

```

1: def MaxOut(Input):
2:     % Pass input through weight kernel and adding bias terms
3:     Input  $\leftarrow$  Input  $\times$  Weights
4:     Input  $\leftarrow$  Input + Bias
5:
6:     % Reshape input into units
7:     Input  $\leftarrow$  Reshape(Input, (Nr Units, Size of Units))
8:
9:     % Reduce input to the largest activation in each unit
10:    Output  $\leftarrow$  Max(Input)
11:
12:    % Reshape to size equal the number of units.
13:    Output  $\leftarrow$  Reshape(Input, (Nr Units))
14:    return Input

```

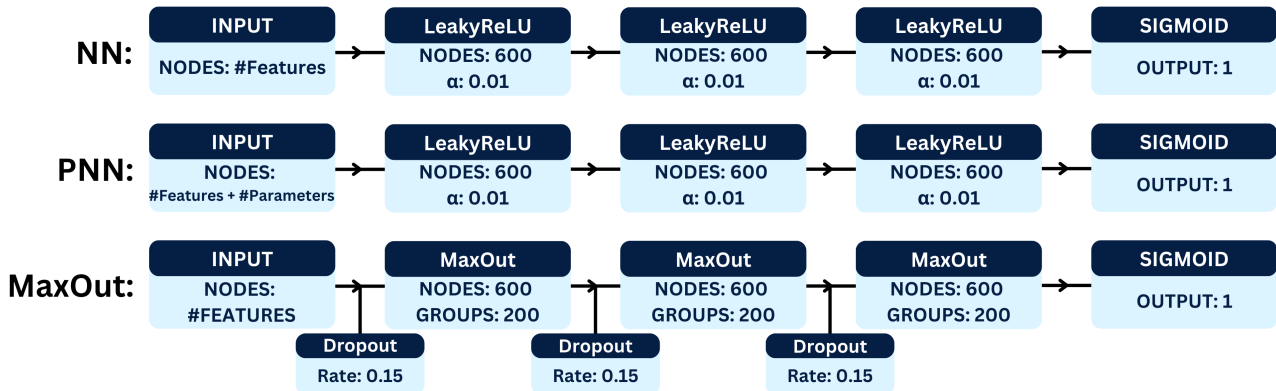


Figure 3.6: A visual summary of the workflow and framework use for the computational analysis.

2.6.4) with an $\alpha = 0.01$. The architecture is designed to perform deep-training, and will train on a training set where all mass combinations are included³⁰.

The **PNN** architecture is like the name suggests, included to represent the model proposed by the article by Baldi et al. [19]. The architecture is illustrated in figure 3.6, with the label PNN. The figure shows a practically identical structure to the dense-**NN**, with the only difference being in the input-layer. As was discussed in section 2.6.6, the **PNN** includes the new physics signal free parameters³¹ alongside the features in the input layer.

MaxOut, Channel-Out and SCO

The ensemble methods are slightly more complex than both the dense **NN** and **PNN** in terms of architecture. To limit the complexity for comparison reasons I choose to build an identical architecture for maxout, channel-Out and **SCO**, with the only difference being which of the three layers is used. In figure 3.6 I have illustrated the MaxOut architecture, with the label MaxOut. The figure shows a network with 6 hidden layers, 3 MaxOut and 3 dropout. The network alternates between drop out and MaxOut, starting with dropout and finishing with MaxOut. The MaxOut layers have 600 nodes each which reduce down to the 200 nodes with the largest activation in their respective groups. Each dropout layer has a dropout rate of 0.15. Channel-out and **SCO** have the same architecture to maxout, but replacing maxout with each of the two respectively.

XGBoost

The main motivation to apply XGBoost is simply to benchmark my analysis, and therefore not a lot of effort has been put into the design of the architecture. As a consequence, the default parameters³² of XGBoost have been used. The main parameters of the model are summarized as the following:

- η (learning-rate) = 0.3
- Max depth = 6
- Maximum number of trees = 100

3.4 Model Training and Validation

3.4.1 Training and Validating data

When building a **ML**-model, the usual approach is to divide your data into three sets; training, validation and testing. The training set is used to tune the internal parameters of the model, i.e. the weights and biases of a **NN** or the cuts of a **DT**. The validation set is used to tune the hyperparameters of the model, i.e. the architecture of the **NN** or the maximum depth of the **DT** etc. The test set should only be used when the

³⁰Contrary to training one network for each mass combination.

³¹In our case, the masses of the BSM-particles.

³²See <https://xgboost.readthedocs.io/en/stable/parameter.html> for a complete overview of default parameters.

model is finished, and is used to benchmark the models' performance. In our case, the performance we are interested in, is the performance on the full MC-backgroundset and its comparison to the measured collision data.³³. Therefore, in this analysis only two sets of data will be used, training and validation where both are sampled from the simulated MC data set. In theory, one could even just use one data set (training) including all the data, but the second was added as a precaution to reduce overfitting when applied to the measured collision data.

The overarching strategy is summarized in the following points:

- Shuffle the data set.
- Split the data set in two, training (80%) and validation (20%)
- Scale the two data set such that the sum of the weights of the background is equal to the sum of the weights of the signal in each data set.
- Scale both data sets using the Standard Scalar approach (see section 2.4.1) using the parameters of the training set on both sets.

The first step ensures an equal distribution of processes in both data sets. The 80 – 20% is a popular practice in ML (see [32]) and was chosen here for convenience. The third step is done to ensure an equal prioritization for background classification and signal classification. In other words, if there was a large imbalance between signal and background, the model would be motivated to tune more towards one trend than another. The final step is motivated in the section regarding data handling 2.4.1.

3.4.2 Training Strategy

To best compare the different ML-models, I decide to apply the same training strategy to all (including the BDT). The strategy is simply to train the model with the training set, then apply an early-stoppage algorithm (see section 2.5.1) with a cut-off based on the performance on the validation set. For every epoch, the model makes a prediction on the validation data set, and logs the results. If more than 10 epochs go by without improving on the epoch with the best result, training stops and the weights of the best epoch are reset. This strategy was repeated for the BDT, but logging for each new additional tree instead of epoch. The performance from each epoch was measured in AUC (see section 2.9.1), where the AUC was calculated with the same weighting as in training (50% signal and 50% background). The distribution of signal vs background is important when studying AUC, as it will greatly affect the value. For example, a classifier which predicts all data to be background is a poor classifier. But, the larger the amount of background relative to signal, the higher the AUC would be measured for such a classifier.

³³See section 2.8.

Chapter 4

Results & Discussion

In this chapter I will present the results from my analysis. First, I will present and discuss my results by comparing different [ML](#)-models.

4.1 Benchmarking the Analysis with Boosted Trees

Boosted trees have been an essential part of [HEP](#) analysis for many years (see [33] and [34]). The XGBoost framework has likewise been used as the benchmark for all [ML](#) analysis, often chosen for its performance in sensitivity and extreme [HPC](#) attributes. Another reason for its popularity is the incredibly simple [API](#), allowing to create and predict a model in two lines of code. Additionally, its incredible boosting capabilities mean that it is little effected by variation in its structure. This leads many to the conclusion that the default parameters (see section 3.3.3) are often the best.

I choose to perform a sensitivity analysis for the original signal data set using a XGBoost model. The results will act as a benchmark when performing further testing with [NN](#)-variants. In figure 4.1 I have presented a grid displaying the achieved significance (see section 2.9.2) for each mass combination in the original signal data set. In the figure we can observe that the XGBoost model performs better for smaller masses. This results can be somewhat counterintuitive, due to signal with smaller masses having a larger resemblance to background than signal with large masses. The explanation is simple that there is much more of the smaller mass signal than there are larger mass signals. By studying figure 3.2 we know that there are a total of 134 events with $(\tilde{\chi}_1 = 200, \tilde{\chi}_2 = 400\text{GeV})$ compared to 6 events with $(\tilde{\chi}_1 = 400, \tilde{\chi}_2 = 800\text{GeV})$. Not only does this mean that the model will have had more small mass signal to train on than large mass, but also that a potential signal region would have to keep far more of the large mass signal to achieve a high significance.

To further investigate the performance of the XGBoost model, I have drawn the distribution of the output for the entire background data set as well as for signal with 4 different mass combinations. The result is found in figure 4.2. The figure shows the output of the XGBoost model with the full output range 4.2a and the output ranging from 0.9-1.00 (4.2b). From the figure we observe a clear separation between signal and background, where most of the signal is given high values (> 0.9) and most of the background is given small values (< 0.1). To further support the effect of statistics in the signal, we can take note of the amount of signal in the higher range of the output (0.975-1). Although the model is able to achieve a much higher effectiveness (is able to preserve more of the signal) for higher masses, there is still at least 4 times as much signal with $(\tilde{\chi}_1 = 200, \tilde{\chi}_2 = 400\text{GeV})$ (the lightest mass combination in the figure) then there are of any other.

A final observation from figure 4.2, is the study of which [SM](#) processes contribute the most for higher model output. In figure 4.2b, we can see that in the output range of $[0.975 - 1]$, the highest contributing processes are *Diboson(l_ll_l)*, *Top – Other* and *t_l*. On the other hand *Z – jets*, which is originally the largest contributing processes, is almost removed in the higher output range. This aligns with my predictions made when studying the distribution of E_T^{miss} (see section 3.2.4).

4.2 Dense Neural Networks

4.2.1 Deep vs Shallow

In previous sections, I have discussed the reasoning for not wanting an automated process for building network architectures (otherwise known as hyperparameter searches). Although, I found manually choosing the architecture for each model to be preferable in this analysis, there are some downsides to that decision.

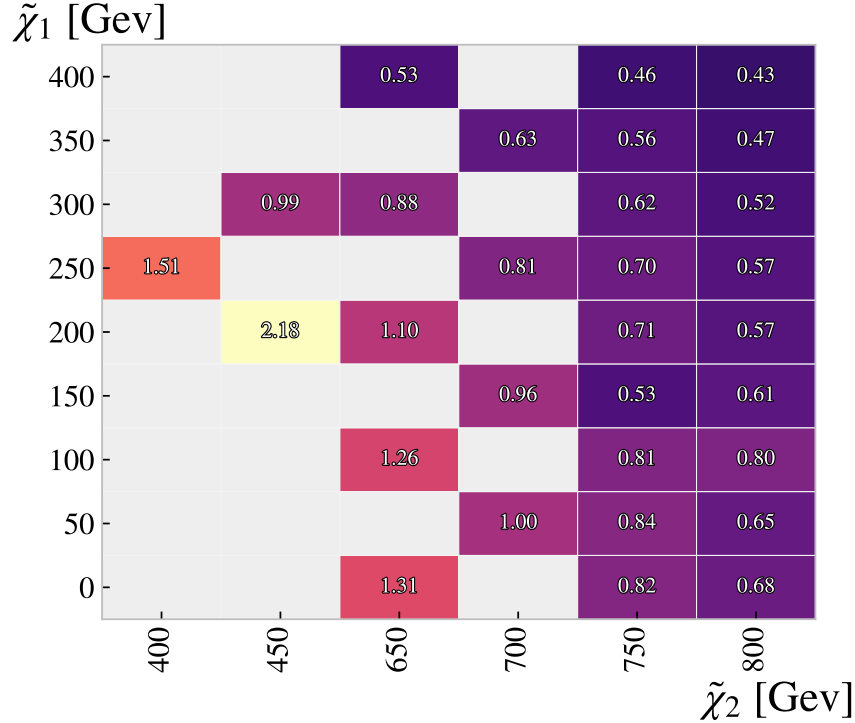


Figure 4.1: A grid displaying the achieved significance on the original signal set, using the signal region created by the *XGBoost* network.

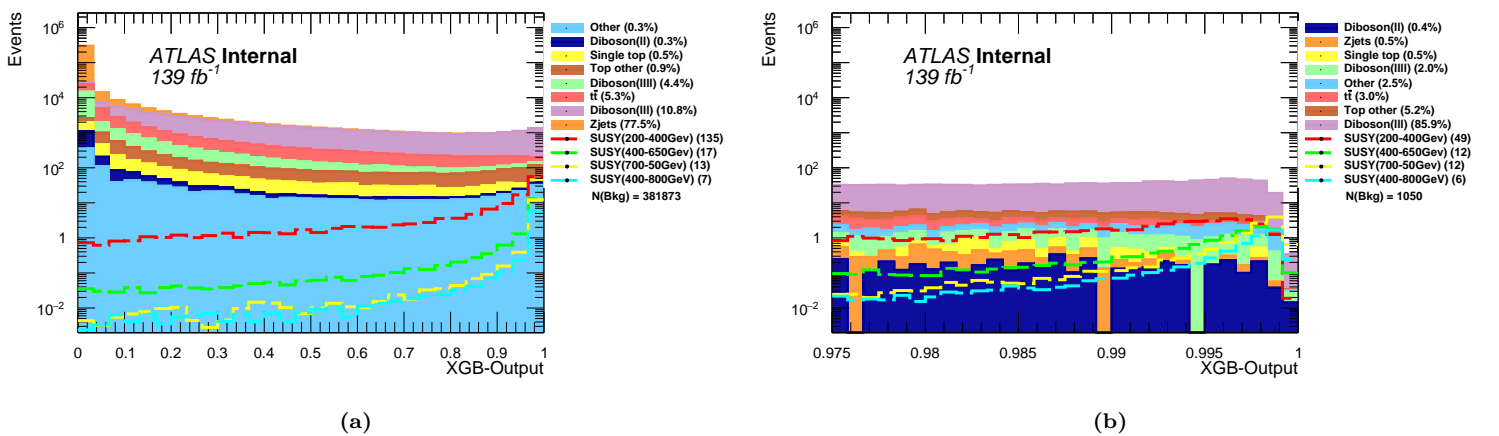


Figure 4.2: The output distribution from a trained XGBoost model for the background and signals with 4 different mass combinations: $(\tilde{\chi}_1 = 200, \tilde{\chi}_2 = 400\text{GeV})$, $(\tilde{\chi}_1 = 400, \tilde{\chi}_2 = 650\text{GeV})$, $(\tilde{\chi}_1 = 700, \tilde{\chi}_2 = 50\text{GeV})$ and $(\tilde{\chi}_1 = 400, \tilde{\chi}_2 = 800\text{GeV})$. The figure includes the full output range (4.2a) and the output ranging from 0.9-1.00 (4.2b).

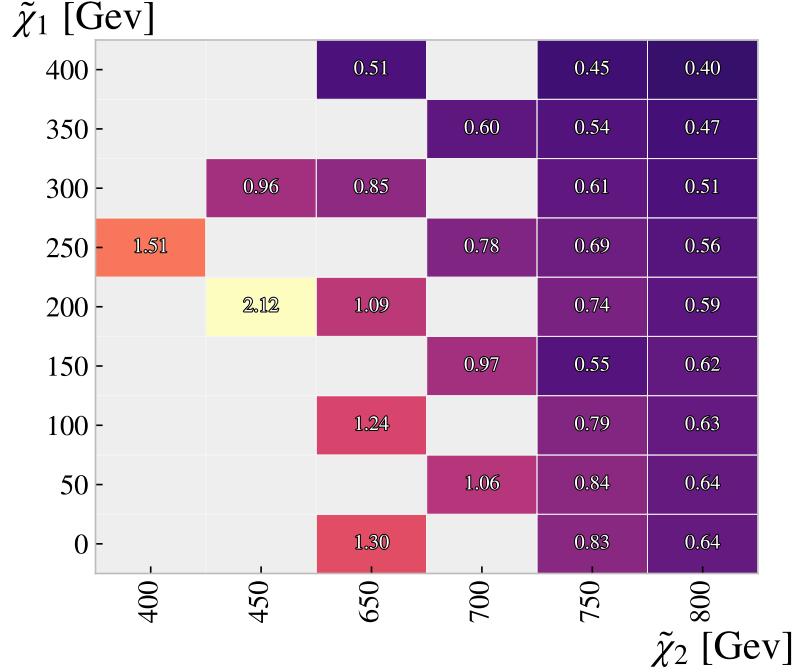


Figure 4.3: A grid displaying the achieved significance on the original signal set, using the signal region created by the shallow NN.

When building each model I wanted to ensure that the performance of said models was representative of the category of models I wanted to build. In other words, I wanted to ensure that any drawbacks were related to the type of model and not a result of poorly chosen number of layers or nodes. Therefore, I wanted to relieve as much randomness in the choice of architecture as possible.

In this section I present a comparison between the results from two dense NN, one deep and one shallow. The deep network uses the dense NN architecture described in 3.3.3, while the shallow network uses the same amount of hidden layers, but with only 20 nodes in each. The comparison represents a sample of networks I choose to compare when deciding the number of nodes and hidden layers would be used in the analysis. Both networks, deep and shallow utilized the training strategy described in section 3.4.2. In figure 4.3, I drew a grid displaying the achieved sensitivity for the shallow network. By comparing with the results achieved by the XGBoost model in figure 4.1, we can observe that the shallow network performs very similarly to the XGBoost model. In fact, the XGBoost model seems to outperform the shallow network ever so slightly.

In figure 4.4, I present the same grid as described above, but using the deep network. By comparing the results from the shallow network in figure 4.3, we can discern that the deep network outperforms the shallow network for every single mass combination in the original signal set. This result motivated the choice of layers and nodes for all networks used in the sections to come.

4.2.2 Parameter Specific Networks and Interpolation

As I have touched upon in earlier sections, one possible solution to a diverse signal set (in my case a signal set with many potential mass combination) is to implement one model for each individual signal set. Initially one might assume that although this approach demands more work, it also produces the strongest performances for all mass combinations individually. I have already discussed how by including different mass combinations in the same signal, we hope to reduce overfitting and potentially allow the model to interpolate between the different mass combinations. However, I have not yet discussed how by moving from a one mass combination signal set to a diverse set would affect the performance on the original signal. In this section I will present the results from an analysis which aims to test the affirmation affect.

In figure 4.5, I present the results from two models who have each trained on two different amounts of signal. The training used to produce the results aligns with the strategy described in section 3.4.2. Figure 4.5a presents the achieved sensitivity from a dense NN which has only trained on one mass combination (which will hence force be referred to as One-Mass-Model (OMM)), ($\tilde{\chi}_1 = 250$, $\tilde{\chi}_2 = 550\text{GeV}$), while figure 4.5b presents the achieved sensitivity (using the same architecture) after training on a large set of mass combinations (which will hence force be referred to as Several-Mass-Model (SMM)). Specifically, the latter

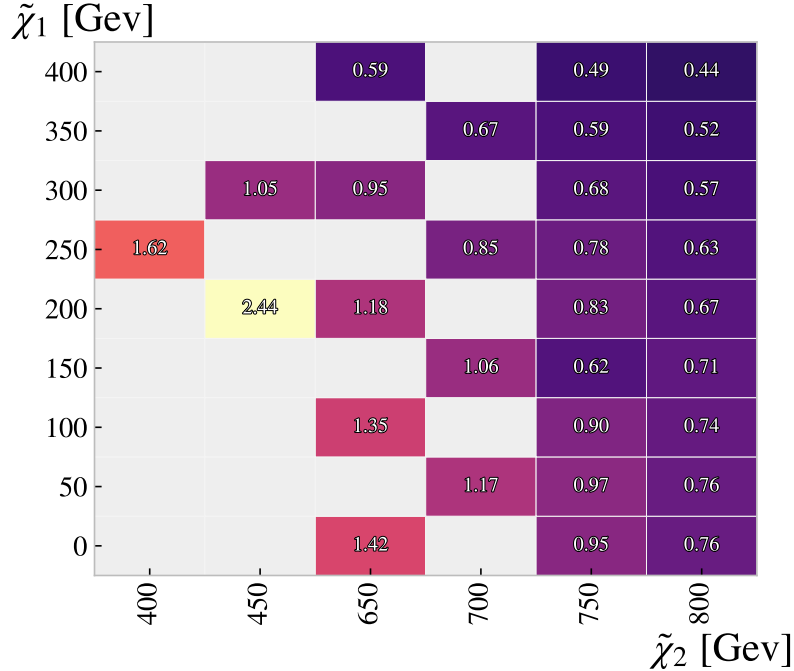


Figure 4.4: A grid displaying the achieved significance on the original signal set, using the signal region created by the dense NN.

figure shows the results after training on all signals on the outer square in the figure 4.5b and ($\tilde{\chi}_1 = 250$, $\tilde{\chi}_2 = 550\text{GeV}$).

My initial prediction of this comparison, was that the **OMM** would outperform the **SMM** for the signal with ($\tilde{\chi}_1 = 250$, $\tilde{\chi}_2 = 550\text{GeV}$), while underperforming on all other data points. The expectation was that **OMM** would learn the trends of the only signal it had seen, while the **SMM** would do the same but for more mass combination and at the same time interpolate the results for the masses in between. By comparing figures 4.5a and 4.5b we see that my prediction was not completely true. We can observe that the model which has trained on several-masses outperformed the **OMM** on every single signal. At first, I believed this to be caused by the **OMM** overfitting a lot sooner than the other model, therefore being stopped earlier in training by the early-stopping criteria described in section 3.4.2. To test this theory, I drew the training history of each training session.

In figure 4.6 I drew the **AUC** score made after each epoch on both the training and validation set for the **OMM** (4.6a) and the **SMM** 4.6b. By comparing the two figures, we observe that the **OMM**'s performance on the validation set peaks in the first epoch, therefore stopping training after 10 epochs, while the **SMM** peaks after 6 epochs. This is a clear indication that training on one mass combination, leads to overfitting.

Given the **OMMs** performance is reduced by the early-stopping criteria, I wanted to explore if it would be able to outperform the **SMM** given it was allowed to train deeper. In figure 4.7, I display the achieved significance of the **OMM** in the case where early-stopping has been removed, and the model was allowed to train for 15 epochs. By comparing figures 4.5b and 4.7, we can observe that even when early-stopping is removed from the **OMM**, it is still outperformed by the **SMM**. This indicates that overfitting is not the only reason for the **OMM**'s disappointing performance.

The most probable explanation for the underwhelming performance of the **OMM**, is that nearby mass combinations (i.e. mass combination with relatively similar masses) exhibit a lot of overlap in terms of feature trends. In other words, nearby mass combinations (in this example, mass combinations differ by 100GeV) often contribute to the same type of training. This means that by including a larger range of signals, which are similar in mass, we are essentially increasing the amount of data for each individual signal.

4.3 Ensemble methods

4.3.1 Visualizing Sparse Pathways

As mentioned in section 3.3.2, the channel-out, **SCO** and maxout layers applied in this analysis were created by me using the TensorFlow API's. As such, I found it imperative to make sure that the layers worked as

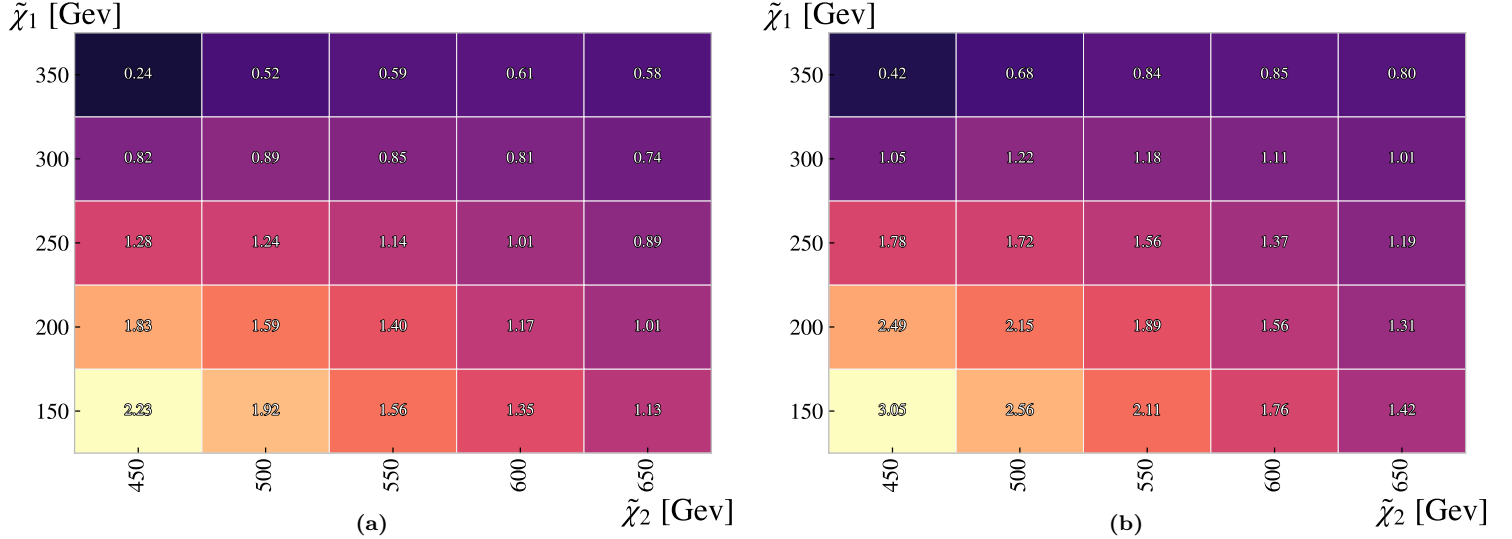


Figure 4.5: Two grids displaying the achieved significance on a subset of the full signal set, using the signal region created by the NN. Figure 4.5a presents the results from a model who has only seen one mass combination during training, ($\tilde{\chi}_1 = 250$, $\tilde{\chi}_2 = 550$ GeV). Figure 4.5b presents the results from a model who has seen all mass combinations in the grid, but for the inner square of masses.

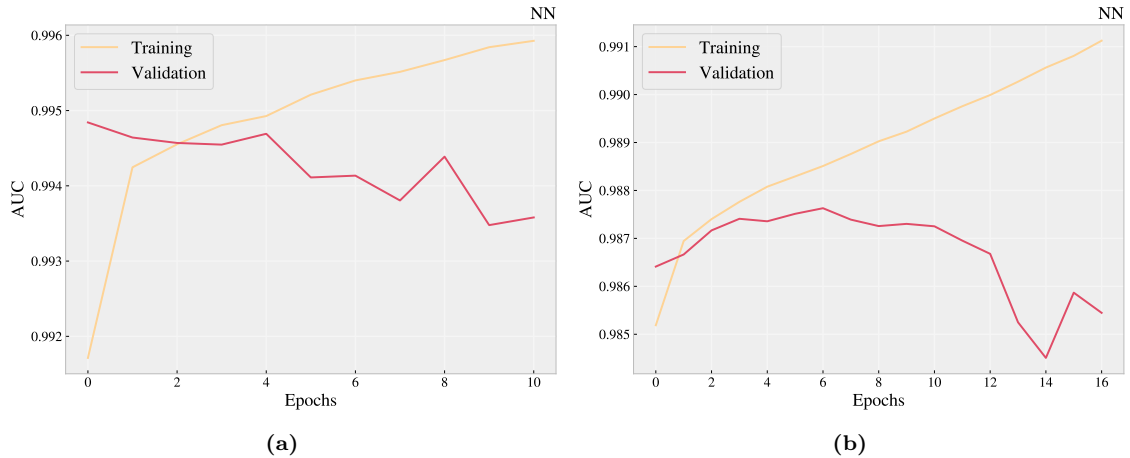


Figure 4.6: A plot displaying the AUC score made after each epoch on both the training and validation set. Figure 4.6a shows the results from the one-mass model and figure 4.6b shows the results from the several-masses model.

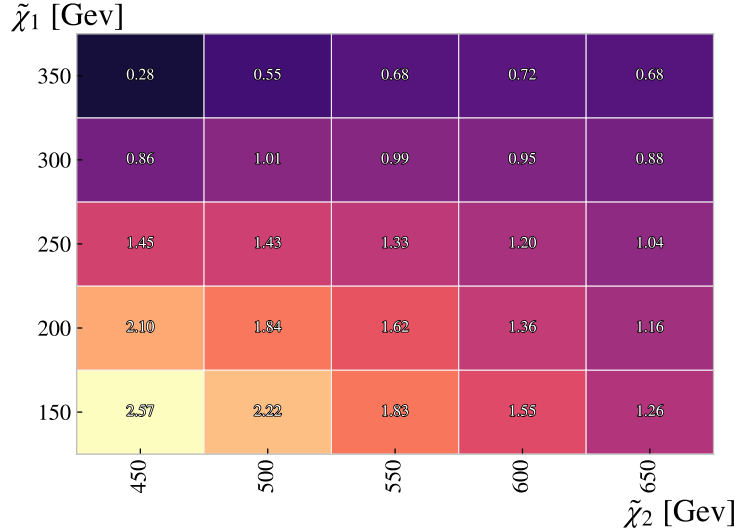


Figure 4.7: A grid displaying the achieved significance on a subset of the full signal set, using the signal region created by the [NN](#). The figure presents the results from a model who has only seen one mass combination during training, ($\tilde{\chi}_1 = 250$, $\tilde{\chi}_2 = 550$ GeV) and was allowed to train for 15 epochs without early-stopping.

intended. To do this I created a small network with three layers, with 8 nodes each, all applying MaxOut layers with 4, 2 and 4 groups respectively. In this section I will dissect the activations of said network before and after training.

In figure 4.8a, I have plotted the activation of 100 randomly sampled collisions, 50 background and 50 signal for an untrained model. Adjacent, I plotted the resulting distribution of the output. From the figure we observe little to no deviation between the activation from the signal and the background. This is mirrored in the distribution of the output which is centered around the middle of the range. A small exception can be found for larger output values, where we observe a small distribution of signal values. This is due outliers in the signal data set.

In figure 4.8b, I plotted a similar plot as described above, but using a trained model. In this figure the output is far more separated, and we see noticeable differences in the activation of nodes. To highlight the difference in activation, I drew two new figures where the signal (4.9a) and background (4.9b) were drawn individually. In the two figures we notice that there is still a noticeable variation in the activation for both signal and background. This is due to outliers in the data, but also the variation of trend. Regardless, there are still clear trends in activation which lets us know that the model has found specific paths in the network for signal and background separately. Most noticeably, the two group in the middle hidden layer highlight this fact. In the case of the signal, the upper group show a clear favoritism to the second bottom node. For the background this is also partly true, but with far more spread in the other nodes. Similarly, in the bottom group (in the same layer), the background shows large activation in the uppermost node, while the signal data does not.

4.3.2 Training History and Overfitting

In section 2.5 I described how creating ensembles of networks is a form of regularization. Therefore, it is of interest to study the relationship between performance on the training set and the validation set for our ensemble methods. In figure 4.12 I drew plots displaying the performance on the training and validation scores after each epoch (50 in total), as measured in [AUC](#) for both a dense [NN](#) (4.12a) and maxout (4.12b). In figure 4.12a we can observe that a deep, dense [NN](#) reaches a maximum in performance for the validation set after only a couple epochs. This peak is then followed by a quick drop in performance, while the training set increases in performance. The drop in performance for the validation set and increase in performance for the training set is a sure sign of overfitting.

In figure 4.12b we observe that an ensemble method (in this case the maxout) displays a different trend. For the first 10 epochs the model increases in performance for both data sets. After this, the validation set does not decrease in performance, but simply holds stable while the training set increases. This is a sign that the model is not experiencing overfitting.

In section 3.4.2, I discussed the training strategy used when training all models in this analysis. I mentioned the implementation of an early-stopping criteria which makes sure that the model only continues to train as

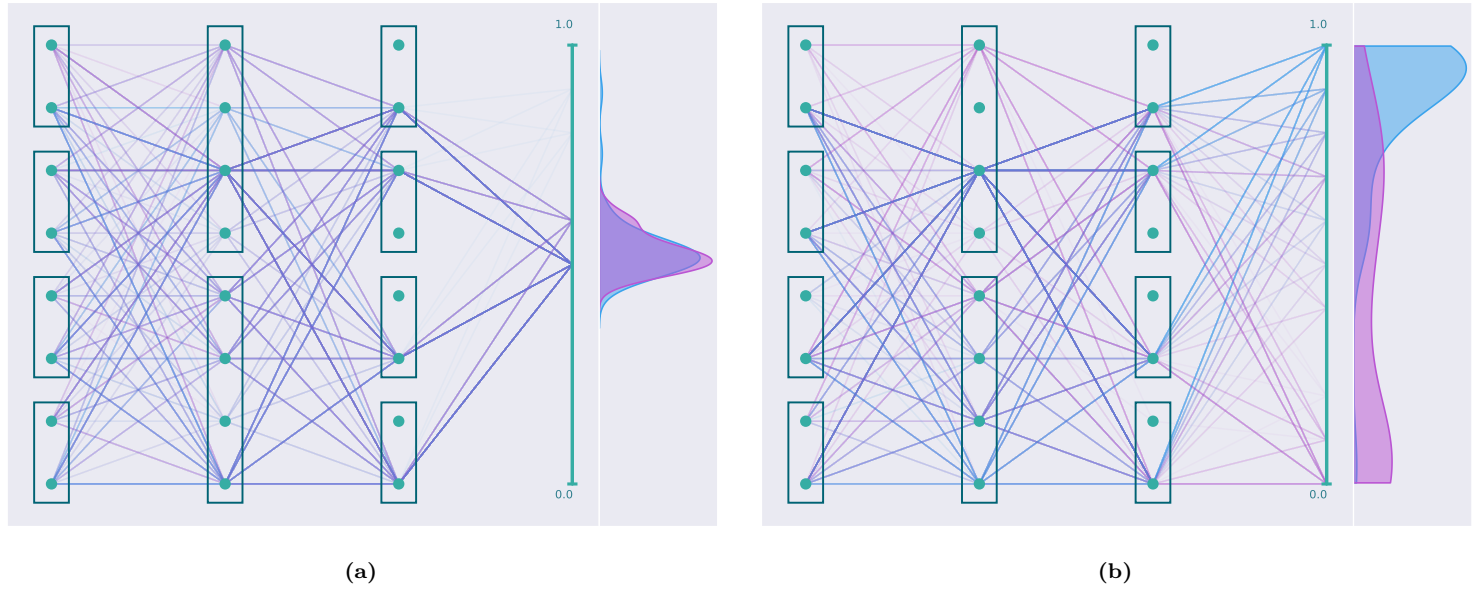


Figure 4.8: A calculated visualization of a 3 layer MaxOut network. Each path represents a data point where all connected nodes were the largest activation in their respective group. The distribution on the far right represent the output distribution. The figure to the left (4.9a) is the result before training and the figure to right (4.9b) is after.

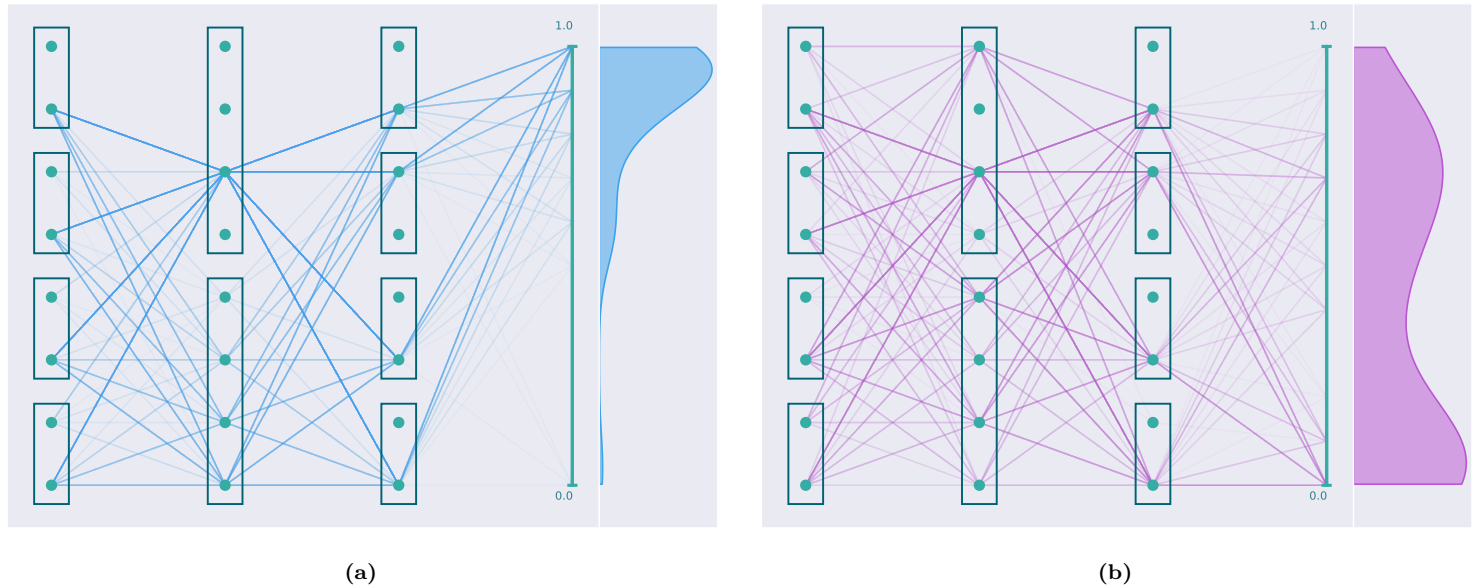


Figure 4.9: A calculated visualization of a 3 layer MaxOut network. Each path represents a data point where all connected nodes were the largest activation in their respective group. The distribution on the far right represent the output distribution and the figure with blue paths 4.9a is the result of signal and the figure pink 4.9b.

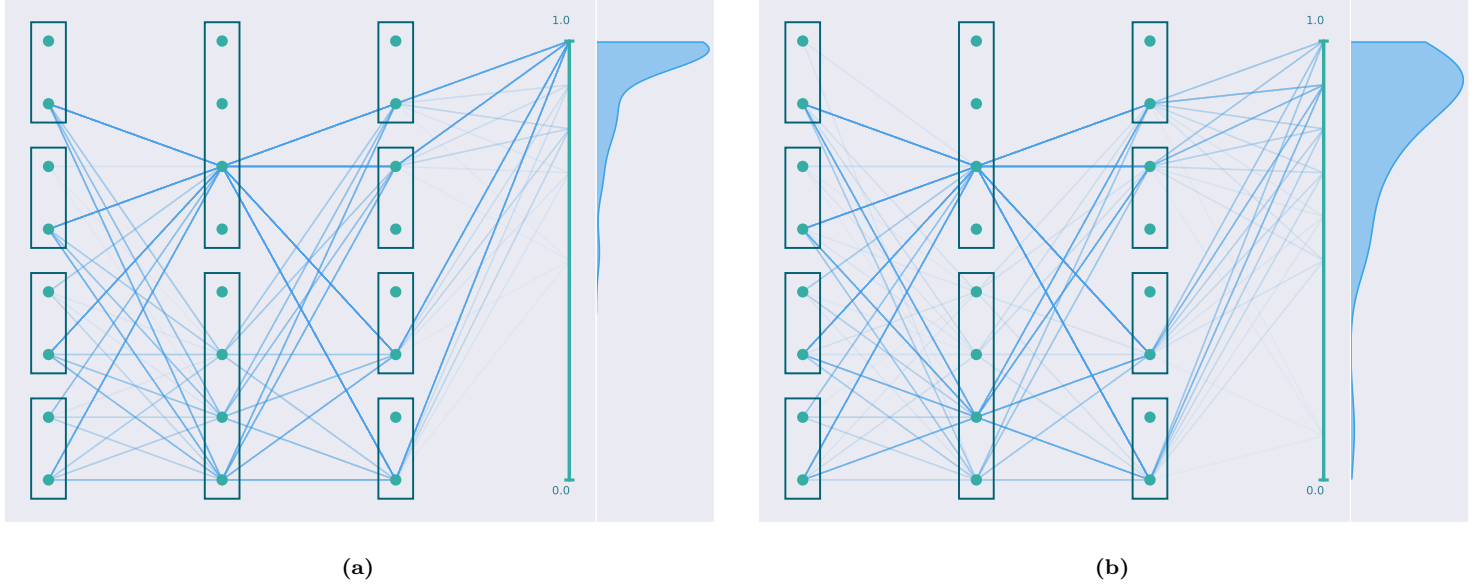


Figure 4.10: A calculated visualization of a trained MaxOut network with 3 hidden layers. Each path represents a data point where all connected nodes were the largest activation in their respective group. The figure to the left (4.10a) is a result of signal with ($\tilde{\chi}_1 = 50$, $\tilde{\chi}_2 = 250\text{GeV}$) and the right (4.10b) ($\tilde{\chi}_1 = 200$, $\tilde{\chi}_2 = 300\text{GeV}$).

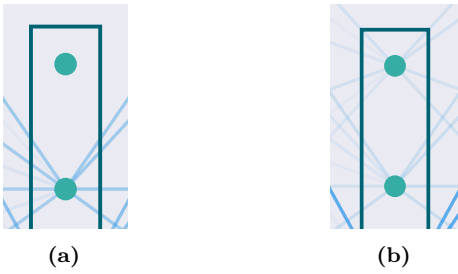


Figure 4.11: A cut-out of the fifth and sixth neuron (counting from the top) in the second hidden layer, activated by the signal with ($\tilde{\chi}_1 = 50$, $\tilde{\chi}_2 = 250\text{GeV}$) 4.11a and ($\tilde{\chi}_1 = 200$, $\tilde{\chi}_2 = 300\text{GeV}$) 4.11b.

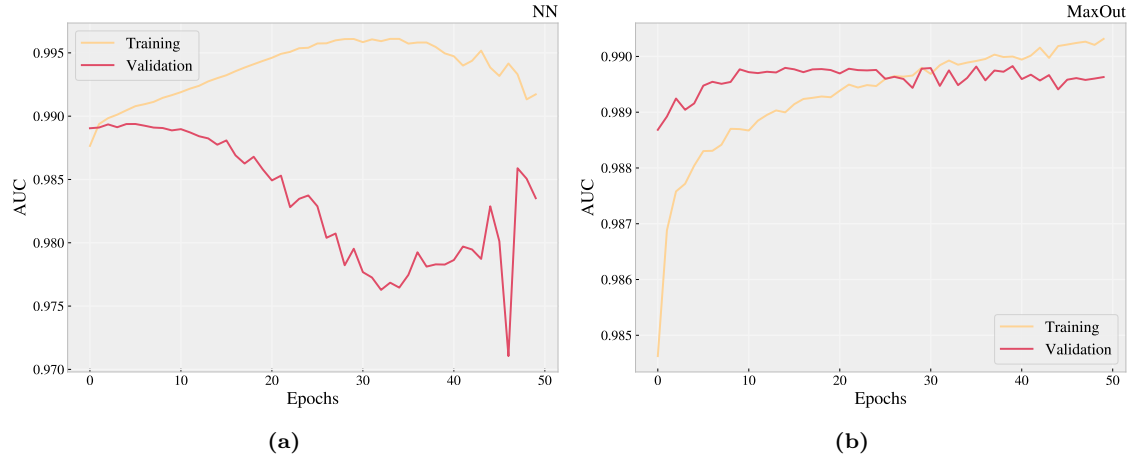


Figure 4.12: A plot displaying the AUC score made after each epoch on both the training and validation set. Figure 4.12a shows the results from the dense NN and figure 4.12b shows the results from a maxout network.

long as the performance on the validation data set increases. By studying the subfigures in figure 4.12, we can deduce that the ensemble methods will not only be able to avoid overfitting, but will as a consequence be allowed to train much longer than the other models.

4.3.3 Comparing achieved Sensitivity between Ensemble methods

In this section I will present and discuss the performance of the three different networks discussed in section 2.5.2, channel-out, SCO and maxout. The results presented in this section were made using the original signal set (see section 3.1.4), the training strategy described in section 3.4.2 and the architectures described in section 3.3.3.

In figure 4.13, I present the achieved sensitivity of the maxout model using the original signal set. The grid shows the same trends as the previous models, i.e. the preference in the higher statistics mass combinations. By comparing the results from the maxout model to the deep, dense network presented in figure 4.4, we discern that the dense network outperforms the maxout model (ever so slightly) for the higher statistic mass combinations. It is plausible that this is due to the difference in depth. The dense network utilizes 3 hidden layers of 600 nodes each, while the maxout, although built with the same architecture, only utilizes 200 nodes per layer when propagating input through the network. This could result in the dense network being able to more deeply tune for the trends in the higher statistics combinations.

However, the most interesting result for the maxout model, is its ability to tune for all mass combinations. Although the dense network outperformed the maxout model for the high statistics combinations, the maxout model outperformed the dense for most other combination (26/30). This result can be credited to two factors. The first being maxout's effect as a form of regularization. In the previous section (see section 4.3.2), I presented how through maxout's regularization abilities, it would be able to uphold the early-stopping criteria for a larger number of epochs. The second factor is maxout's innate training memory³⁴ which was tested in section 4.3.1. From figure 4.13, we are able to deduce that although the maxout model is not able to train to the same depth for the lower masses, it is able to achieve a large level of generalizability through reducing overfitting and increasing training memory.

In appendix A.1.1 I have included grids displaying the achieved sensitivity for both channel-out and SCO. Both models demonstrate similar performance to the maxout layer. To compare the three methods, I created a "pie-plot". A pie-plot compares the achieved sensitivity between several models and display the results for each individual mass combination. In figure 4.14 I present the pie-plot comparing maxout, channel-out and SCO. Each mass combination includes a pie, where the size of each "slice" represents the relative size of the significance compared to the other methods. The color surrounding each pie marks which method achieved the highest sensitivity for the respective combination.

By studying the pie-plot in figure 4.14, we can deduce that maxout model outperforms the other two in most of the mass combination (24/30). From the sizes of each "slice", we can observe that all three models seem relatively equal in performance, maxout only outperforming the others by a small fraction. The most interesting observation from the pie-plot is the performance from the SCO, as this model was in-part created by me. Except the mass combinations where maxout was the most sensitive, SCO outperformed the rest.

³⁴By training memory, I refer to the models' ability to tune towards several trends without reducing in performance.

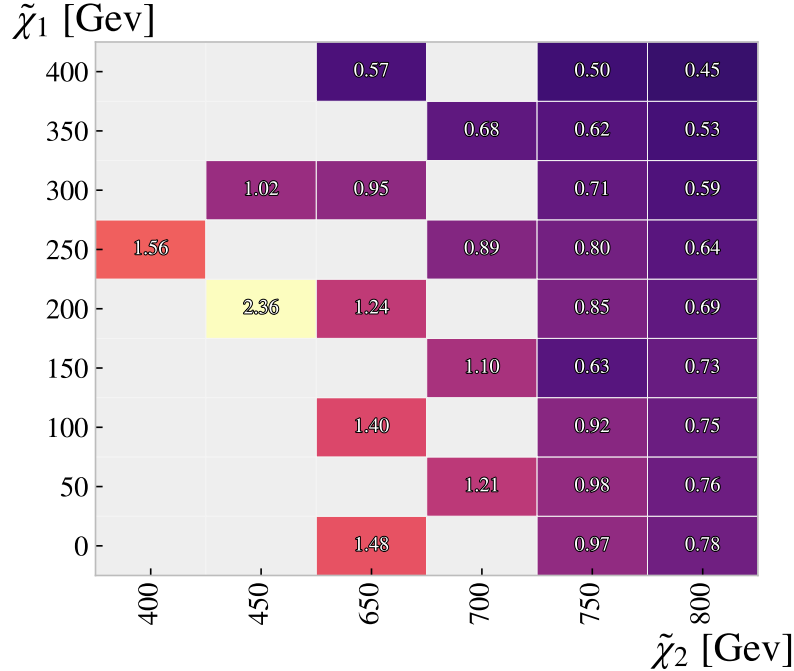


Figure 4.13: A grid displaying the achieved significance on the original signal set, using the signal region created by the *MaxOut* network.

This is an indicator that although the method seemed not to be the most optimal ensemble method for this analysis, it does indeed show great promise and should be further explored in further analysis.

4.4 Parametrized Neural Network

4.4.1 Discriminating Masses

When introducing the **PNN** in section 2.6.6, I mentioned that by including the masses of the introduced particles in the feature set, we motivate and individualistic tuning for each mass combination in the signal set. To test if this is indeed what happens, I will in this section present results where I manually assign different mass combinations the same label. The hope is that if indeed the **PNN** has been able to tune individually for each mass combination, then the **PNN** should perform best when the events are correctly labeled compared to when they are not.

In figure 4.15a I have drawn the distribution of the output from the trained **PNN** architecture (see section 3.3.3). The model was trained using the Full Statistics Minus Low Masses (**FSMLM**) data set. In figure 4.15a, 4 signals have been included; $(\tilde{\chi}_1 = 50, \tilde{\chi}_2 = 250\text{GeV})$, $(\tilde{\chi}_1 = 100, \tilde{\chi}_2 = 200\text{GeV})$, $(\tilde{\chi}_1 = 200, \tilde{\chi}_2 = 300\text{GeV})$ and $(\tilde{\chi}_1 = 150, \tilde{\chi}_2 = 250\text{GeV})$. All data, including both signal and background were given the labels of 50 and 250. In figure 4.15a the full output range is included, whereas in figure 4.15b only the output in the range $0.975 - 1$ has been included. From studying the figures and the corresponding legends, we can deduce that the signal which is given the correct label is also the signal which has the highest percentage of conserved events when applying a simple cut off 0.975³⁵.

In section 4.1 I presented results indicating that some signals were easier to separate from background than others. This leads me to the question; did the **PNN** perform better on the signal with $(\tilde{\chi}_1 = 50, \tilde{\chi}_2 = 250\text{GeV})$ because of the labeling, or simply because this particular signal was easier to separate. To answer this question I conducted a second test. In figure 4.16 I repeated the analysis described in the paragraphs above, but where all the signals were given the label $(\tilde{\chi}_1 = 200, \tilde{\chi}_2 = 300\text{GeV})$. Similarly to the previous results, I drew the output for the full output range (4.16a) and after a cutoff off 0.975 (4.15b). Via the examination of the two figures, we can indeed see that my assumption was right. By giving events with $(\tilde{\chi}_1 = 50, \tilde{\chi}_2 = 250\text{GeV})$ the wrong label, the **PNN** still achieved the highest performance when predicting on said mass combination.

To further study this result, I created a table of the efficiencies of each mass combination after applying

³⁵This is further evident when studying the efficiency rates in table 4.1.

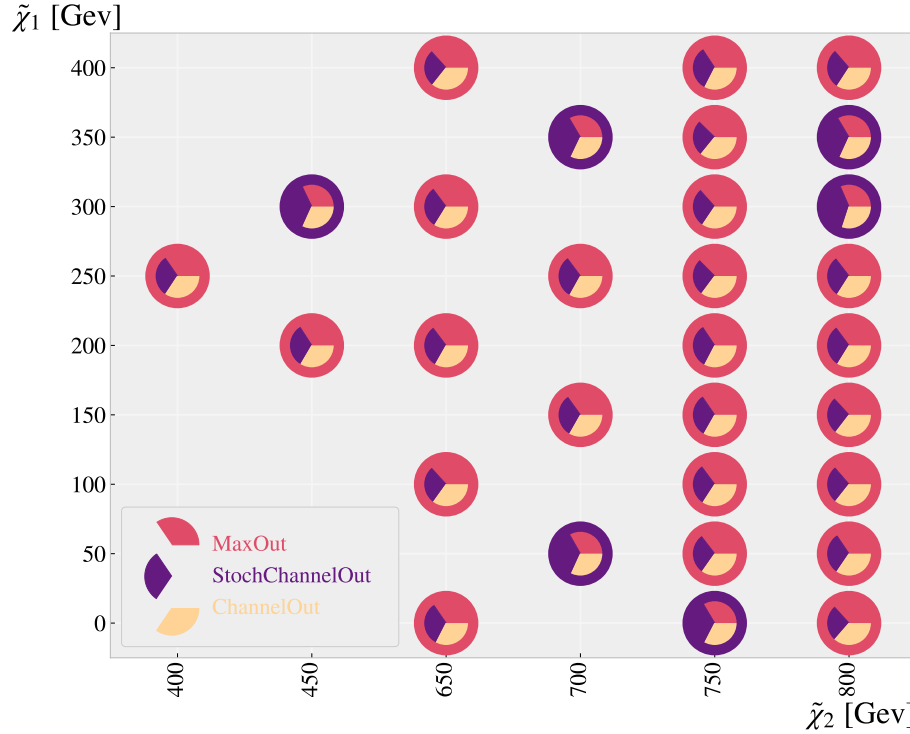


Figure 4.14: A sensitivity comparison between the ensemble methods (maxout, SCO, channel-Out) on the original signal data. The size of the "pie" represents the relative size of the significance and the color around each point displays the method with the largest sensitivity for the respective combination.

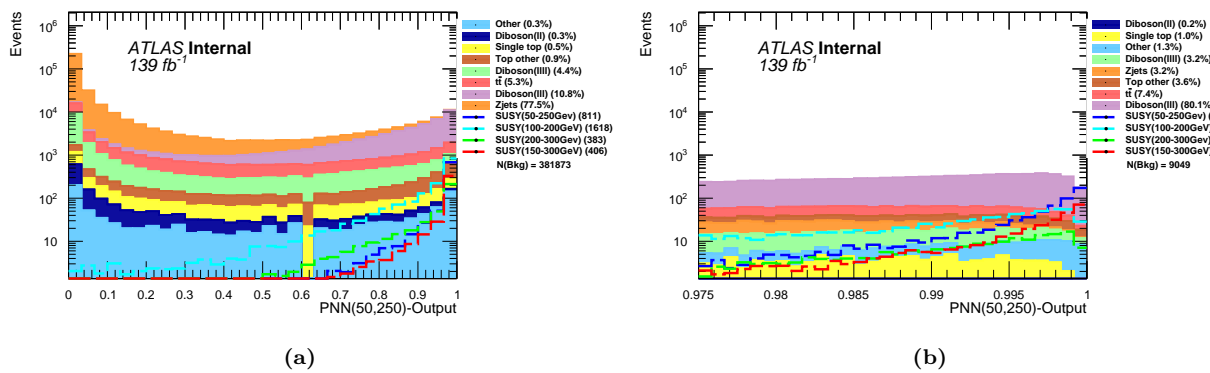


Figure 4.15: The output distribution from a trained PNN model for the background and signals with 4 different mass combinations: $(\tilde{\chi}_1 = 50, \tilde{\chi}_2 = 250\text{GeV})$, $(\tilde{\chi}_1 = 100, \tilde{\chi}_2 = 200\text{GeV})$, $(\tilde{\chi}_1 = 200, \tilde{\chi}_2 = 300\text{GeV})$ and $(\tilde{\chi}_1 = 150, \tilde{\chi}_2 = 250\text{GeV})$, and where all the data were given the parameter features of $(\tilde{\chi}_1 = 50, \tilde{\chi}_2 = 250\text{GeV})$. The figure includes the full output range (4.15a) and the output ranging from 0.975-1.00 (4.15b).

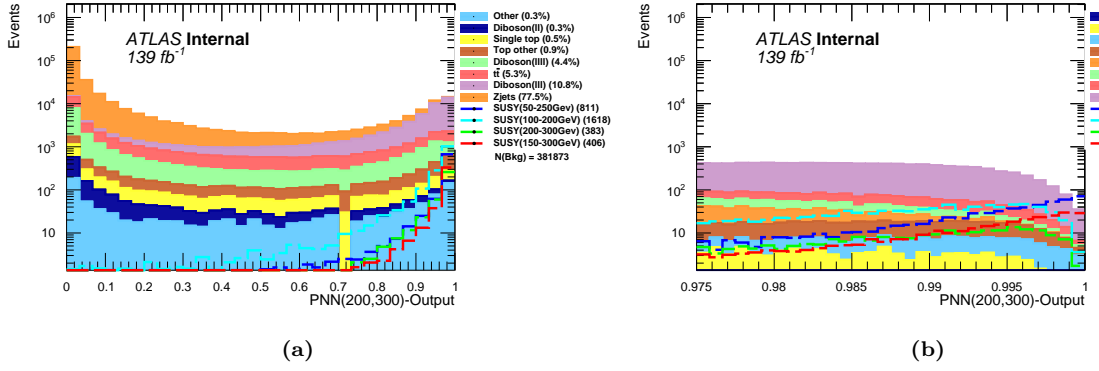


Figure 4.16: The output distribution from a trained PNN model for the background and signals with 4 different mass combinations: $(\tilde{\chi}_1 = 50, \tilde{\chi}_2 = 250\text{GeV})$, $(\tilde{\chi}_1 = 100, \tilde{\chi}_2 = 200\text{GeV})$, $(\tilde{\chi}_1 = 200, \tilde{\chi}_2 = 300\text{GeV})$ and $(\tilde{\chi}_1 = 150, \tilde{\chi}_2 = 250\text{GeV})$, and where all the data were given the parameter features of $(\tilde{\chi}_1 = 200, \tilde{\chi}_2 = 300\text{GeV})$. The figure includes the full output range (4.15a) and the output ranging from 0.975-1.00 (4.15b).

Label	Channel			
	(50, 250)	(100, 200)	(150, 300)	(200, 300)
(50, 250)	80.8%	45.8%	77.5%	50.1%
(200, 300)	77.3%	54.6%	76.3%	59.0%

Table 4.1: A listing of the remaining procentage of each mass combination in the output range 0.975-1.00 using the labels $(\tilde{\chi}_1 = 50, \tilde{\chi}_2 = 250\text{GeV})$ and $(\tilde{\chi}_1 = 200, \tilde{\chi}_2 = 300\text{GeV})$ respectively.

a simple cut of 0.975. The results are represented in table 4.1. It is evident from table 4.1 that the PNN achieves the highest performance when events are given the correct label, although not by much. Another interesting observation is that events with $(\tilde{\chi}_1 = 100, \tilde{\chi}_2 = 200\text{GeV})$ seem to prefer the label of $(\tilde{\chi}_1 = 200, \tilde{\chi}_2 = 300\text{GeV})$ over that of $(\tilde{\chi}_1 = 150, \tilde{\chi}_2 = 250\text{GeV})$, despite the latter mass combination being closer in mass. A possible explanation is that the difference in mass ($\Delta m = |\tilde{m}_{\tilde{\chi}_1} - \tilde{m}_{\tilde{\chi}_2}|$), influences the trends in the data, similarly to what we saw that size of mass does. Regardless, from 4.1, we can deduce that the PNN does in fact discriminate between mass combinations and tune for them independently.

4.4.2 Sensitivity Result

In this section I will present the achieved sensitivity by the PNN on the original signal set. In figure 4.17, I present a grid displaying the sensitivity of the PNN on the original signal set. Similarly to the previous models', the figure indicates that the PNN is able to achieve a much higher sensitivity on the lower masses. The most notable difference to the previous models, is the range of significance. The PNN almost doubles the highest significance achieved by any previous model (from 2.44 to 4.14), and simultaneously achieves the lowest significance (now 0.30). The most probable explanation to this result is the distribution of parameters for the background. In section 2.6.6, I described how the background is randomly assigned parameters such that the percentage of background with a given label is equal to the percentage of the signal with said label. In other words, the higher the statistics for a given mass combination, the higher the amount of background will be "linked" to it. In the same section I also described the hope that the parameters would shift the output from the initial layer in a way that motivates individualistic training. If this is true³⁶ it means that masses with larger statistics, are given larger amounts of background to train with. This could explain the uneven performance by the PNN.

In this analysis I choose to follow the methodology described in the article by Baldi et al. [19], but other variants of the PNN could be of interest in future studies. An alternative to the current setup for distributing parameters to the background, is to distribute the parameters evenly. In other words, for N different mass combinations, each set of parameters will be distributed to $1/N$ parts of the background. This would most likely produce more consistent results. I considered using an even approach, but found that the current setup was more aligned with the rest of the analysis where a 1-1, signal- background ratio approach has been

³⁶For a network of this depth, it is very hard to explain what happens during training. Lack of explainability is in fact one of the biggest downsides to deep networks.

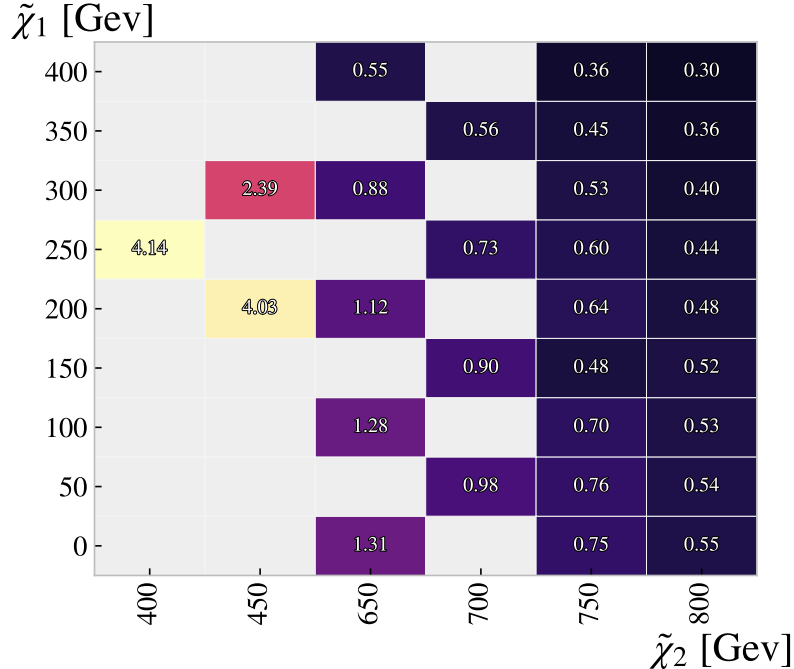


Figure 4.17: A grid displaying the achieved significance on the original signal set, using the signal region created by the [PNN](#) network.

made³⁷. The more interesting alternative would be to assign the background most similar to a given mass combination, the same parameters. This would focus the training of the [PNN](#) on the set of events which should be hardest to separate. Due to time constraints of this thesis, I decided not to test this approach, but would be an interesting area to explore.

4.5 Comparing Models on Original Signal Set

So far in the thesis I have presented results from two branches of [ML](#), Boosted Decision Trees ([BDT](#)) and Neural Network ([NN](#)). In the case of the latter, I tested three further variations, a dense [NN](#), ensemble networks and [PNN](#). In figure 4.18 I have drawn a pie-plot comparing the sensitivity on the original signal set for the four different models. By assessing figure 4.18, we can deduce that the maxout network outperforms all other models in most mass combinations (24/30), although not by much. Additionally, we can discern that the [PNN](#) is far more sensitive than the other models for higher statistics mass combinations, and underperforms for low statistic mass combinations.

On the other hand, the XGBoost model is outperformed in all but one combination, implying that the networks are more ideal for this analysis. It is worth noting however, that not a lot of time was spent improving the XGBoost model. While for the networks, I experimented with different layers and tested for different architectures, no effort was put in deciding the architecture of the XGBoost. Likewise, the solution to the negative weights (see section 3.2.5) could by all means be optimized if given more attention. Therefore, it is worth saying that the results in this analysis do not imply that deep networks are a better analysis tool for [BSM](#) searches than [BDT](#)'s, but rather exemplify the advanced capabilities of deep networks.

4.6 Increasing Sensitivity through PCA

So far in the analysis, all features have been given an equal weighting in the beginning of training. But, as mentioned in section 2.8, not all features contribute to an effective signal region. In section 2.4.2, I explained how through the use of [PCA](#), we are able to create a new set of features which can be ordered by amount of variance. In this way, we can reduce the dimensionality of the data set, while at the same time preserving most of the variance. In this section I will present the results of training on a data set which has gone through such a [PCA](#).

³⁷In section 3.4.1 I discuss how I have chosen to scale the weights such that sum of the weights of the background is equal to the sum of the weights of the signal.

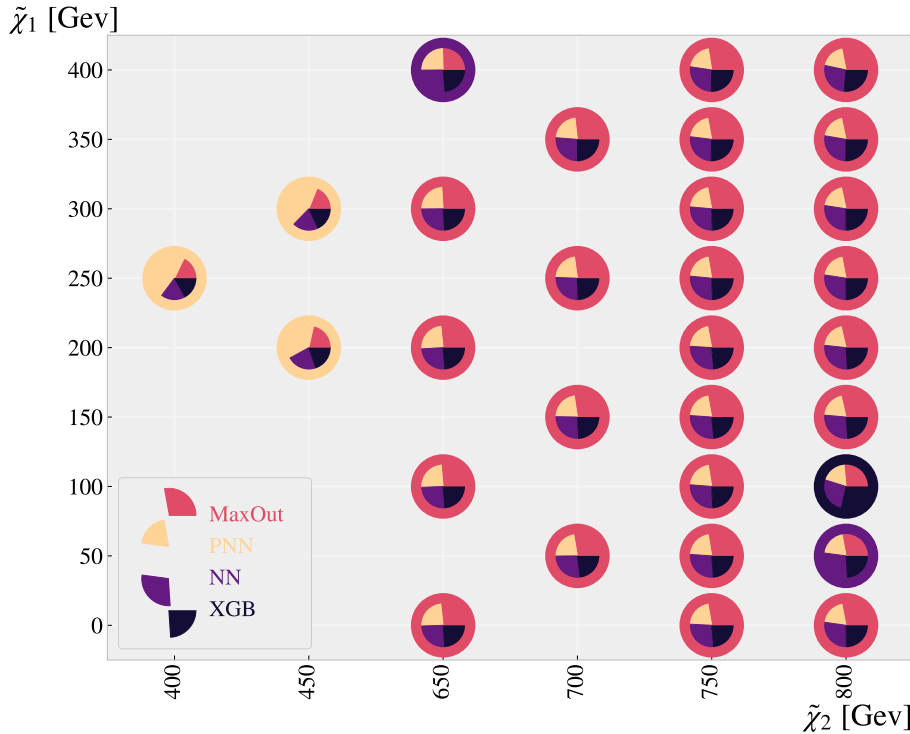


Figure 4.18: A sensitivity comparison between a dense **NN**, **PNN**, maxout and XGBoost on the original signal data. The size of the "pie" represents the relative size of the significance and the color around each point displays the method with the largest sensitivity for the respective combination.

In this analysis I performed a **PCA** on the data set, and demanded that 99.99% of the variance should be preserved. In doing so, 5 features were removed. In appendix A.1.2, I have included the grids displaying the new sensitivity for the original signal set, using data which has gone through a **PCA**. In figure 4.19, I have included two pie-plots comparing the sensitivity of the maxout (4.19a) and the (4.19b) with and without a **PCA**.

In figure 4.19a, we can observe a relatively similar behavior with and without the **PCA**. There seems to be no obvious trends in regard to improvement or decrease in performance for any of the mass combinations. But, to simplify the comparison between the two, we can treat all mass combinations equally. With this in mind, maxout achieves a higher sensitivity *with* a **PCA** in 21/30 combinations, indicating that **PCA** indeed increased performance. Similarly, the **PCA** increased performance for the **PNN**, but contrary to maxout it did so for every combination in the original signal set. Additionally, through closer study of the ratio's for each "pie", the **PCA** not only increased a larger number of combinations for the **PNN**, but also increased the performance by a larger degree. Through a similar analysis, I deemed the **PCA** to decrease performance for the **NN**, only improving 11/30³⁸.

To compare all three models discussed above with the **PCA** included, I created a pie-plot which is displayed in figure 4.20. By comparing the pie-plots made with and without **PCA** (see figure 4.18), we notice that maxout now outperforms the dense **NN** in combinations previously preferred by the dense **NN**. Similarly, the **PNN** now outperforms the maxout in three new combinations. By chance, all three of said combinations were combinations where the maxout model preferred no **PCA**. This is yet another indication that building models to be sensitive to a large range of signals can sometimes lead to changes which improve performance for some combinations, and are destructive for others. Like I mentioned in the paragraph above, I decided to treat all combinations equally, but with the previous point in mind, weighting the importance of certain combinations based on scientific promise/interest could be a better approach.

4.7 Comparing Models on Full Statistics Signal

So far in the analysis I have only tested on a subset of the signal, which I have called the original signal set. In this section I will extend my search to include the full signal set displayed in figure 3.2. The full signal set consists of 89 mass combinations compared to the original 30, and extends the mass ranges to

³⁸The pie-plot comparing the dense **NN** with and without a **PCA** is included in the appendix A.1.2.

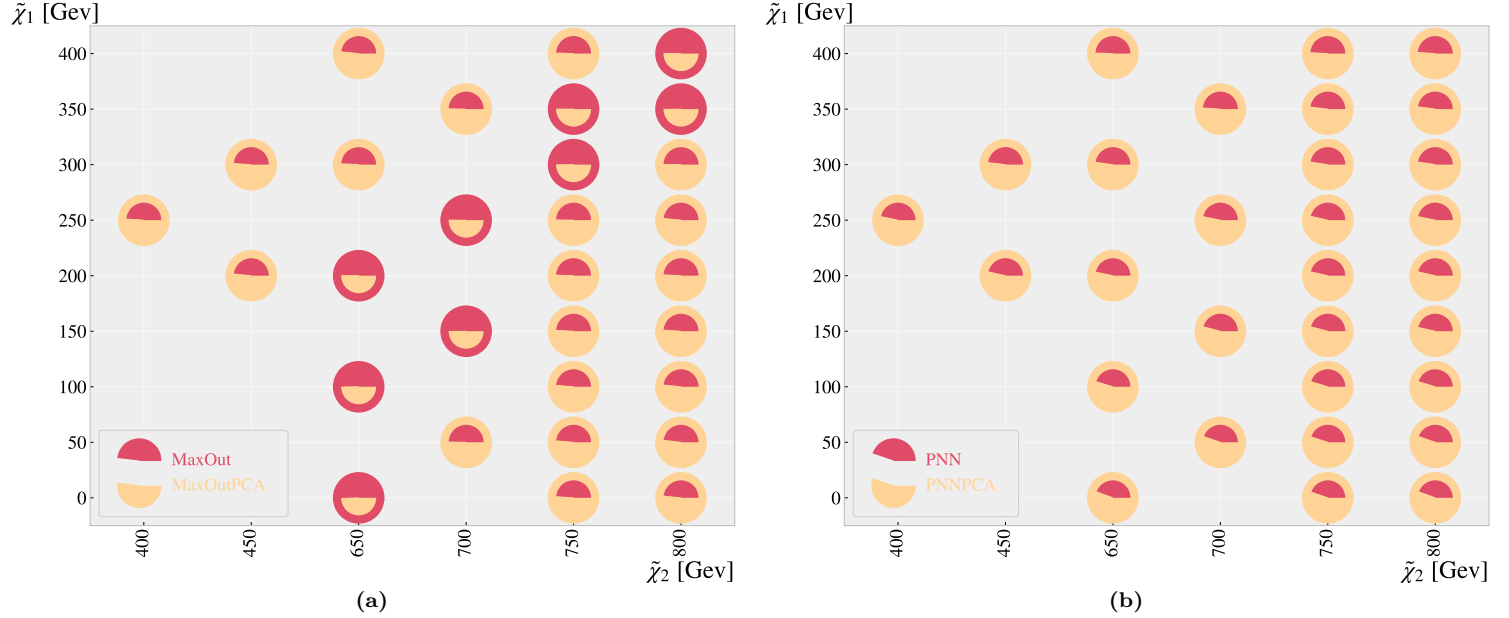


Figure 4.19: Two pie-plots comparing sensitivity on the original signal set, where each figure shows the comparison between a model training on data with and without a PCA. Figure 4.19a displays the comparison for the maxout model, and likewise figure 4.19b for the PNN. The size of the "pie" represents the relative size of the significance and the color around each point displays the method with the largest sensitivity for the respective combination.

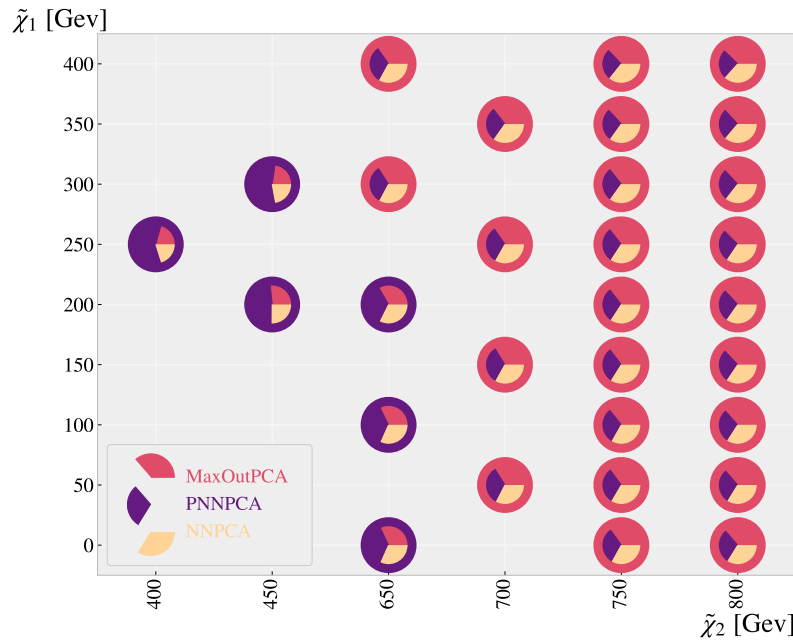


Figure 4.20: A grid displaying the achieved significance on the original signal set, using the signal region created by the NN network. A PCA analysis has been applied to the data being utilized in this result.

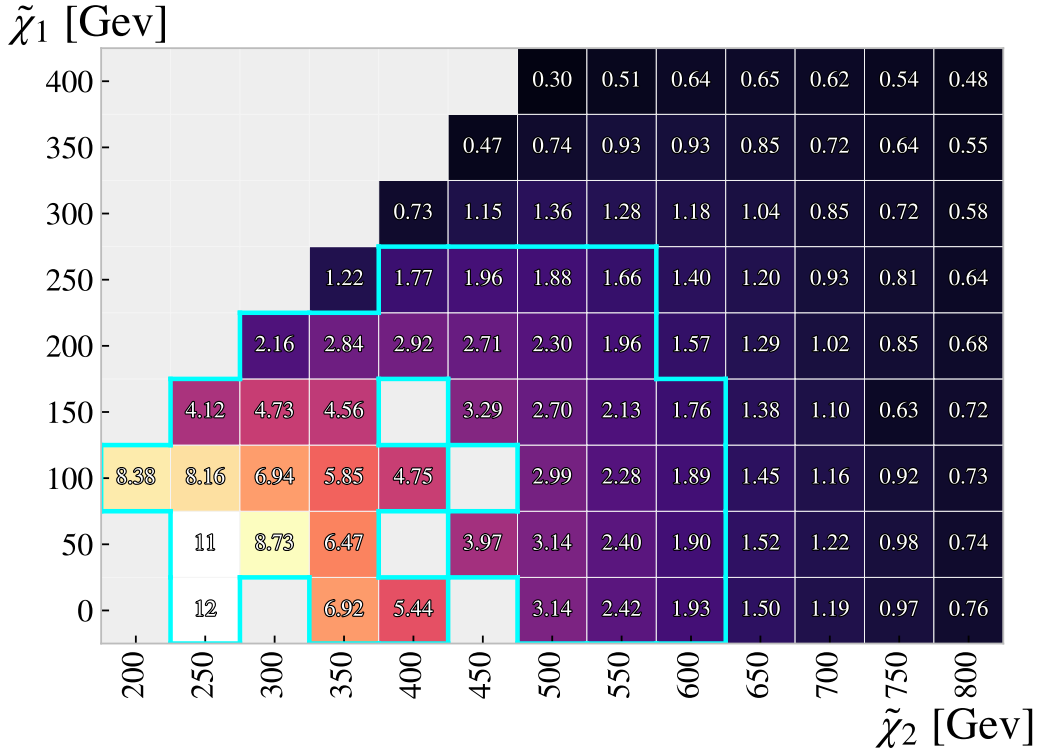


Figure 4.21: A grid displaying the achieved significance on the full statistics signal set, using the signal region created by the [NN](#) network.

$\tilde{\chi}_1 \in [0 - 400]\text{GeV}$ and $\tilde{\chi}_2 \in [200 - 800]\text{GeV}$. In the figures to come, I have included a turquoise band around all combinations with a significance of over 1.64 (see section 2.9.2). When comparing the results, we are not only interested in how sensitive the models are for each combination individually, but also with how many combinations they were able to achieve a sensitivity of over 1.64. However, similarly to previous results, the significance does not include any uncertainty.

I will not apply all previously tested models to the full statistics signal set. Instead, I will only apply the models I found most ideal for this analysis, based on the tests performed in the previous sections. I decided to choose one model from each "type"³⁹ of network. Based on the results in section 4.3, where I compared the different ensemble methods, I found the maxout model to be the top performer. Likewise, in section 4.6 I found that both maxout and the [PNN](#), preferred to utilize data with a [PCA](#). Therefore, I will utilize the maxout model and [PNN](#) model defined in section 3.3.3, with the use of [PCA](#). Finally, I will include the ordinary dense [NN](#) for the sake of diversity.

In figure 4.21, I have drawn a grid displaying the sensitivity of an ordinary dense [NN](#), on the full statistics signal set. Again, we observe that higher statistics mass combinations, result in a higher significance. Additionally, the dense [NN](#) was able to achieve a sufficient significance for over 38 mass combinations, all between the ranges of $\tilde{\chi}_1 \in [0 - 250]\text{GeV}$ and $\tilde{\chi}_2 \in [200 - 600]\text{GeV}$. What is even more interesting, is that by comparing the results on the full set with the results on the original set (see figure 4.4), we notice that the network was able to improve its sensitivity on every single mass combination from the original signal set. This is yet another indication that the deep networks are able to exploit overlapping regions in the feature space between nearby combinations.

Figure 4.22 displays a grid presenting the sensitivity of the maxout model using the full statistics signal set. The data used to train this model, has been through a [PCA](#), and the architecture is the same as described in section 3.3.3. Similarly to the dense [NN](#), by including the full statistics, the maxout model improved performance on all combinations in the original set. Also, the maxout model upholds the sensitivity criteria (> 1.64) for the same mass combinations. Contrary to the tests performed on the original signal set however, when using the full statics, the dense network outperforms the maxout model in most of the signals (74/89). A possible explanation to the shift in performance, could be that the dense [NN](#) lacked the statistics when training with the original signal set. When the full statistics is included, the dense [NN](#) (which is deeper than the maxout model) is able to train much deeper, which in turn increases sensitivity. However, the maxout

³⁹By network type, I am referring to either the ordinary dense network, the [PNN](#) or an ensemble.

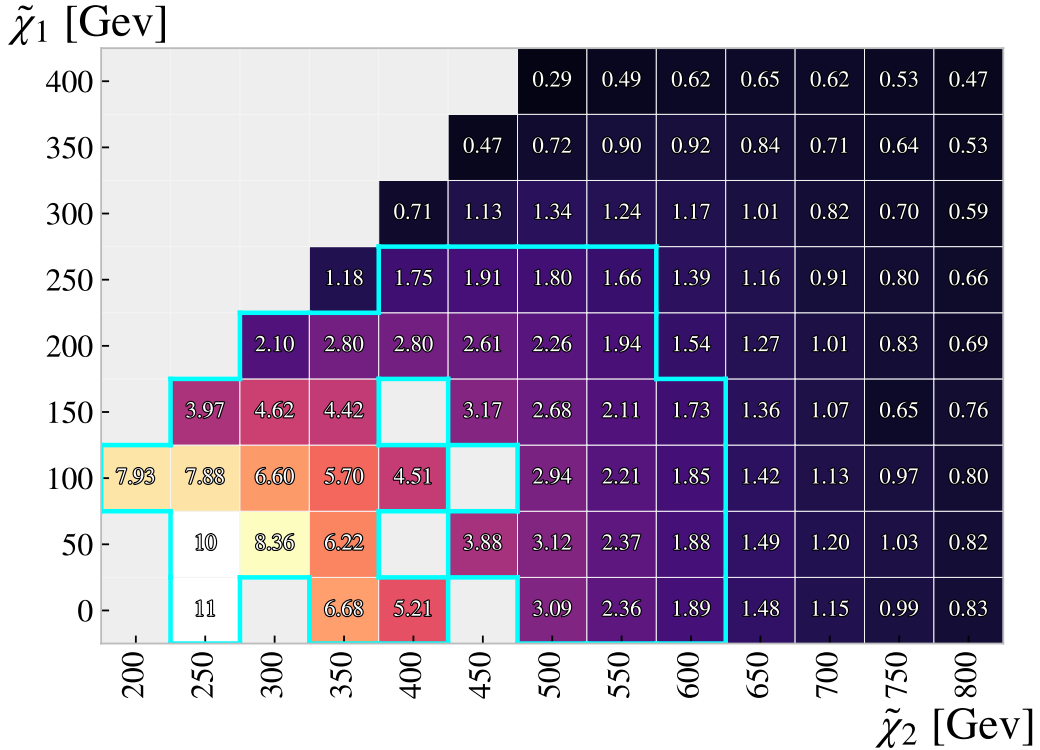


Figure 4.22: A grid displaying the achieved significance on the full statistics signal set, using the signal region created by the *MaxOut* network.

model outperforms the dense network for the low statistics combinations, again indicating the maxout layers ability to increase training memory⁴⁰.

Finally, I applied the **PNN** to the full statistics signal set. The results are found in the grid presented in figure 4.23. Similarly to the tests performed with the original signal set, the **PNN** is able to achieve an incredible sensitivity for the high statistics mass combinations ($\tilde{\chi}_2 < 400$). For the combinations with the highest statistics ($\tilde{\chi}_2 < 300$), the **PNN** more than doubles the achieved significance. For the lower statistics combinations, the **PNN** drops in performance. In comparison to the ordinary dense network and the maxout model who both achieved sufficient sensitivity for 38/89 combinations, the **PNN** only did so for 33/89. Moreover, the performance of the **PNN** on the combinations with the highest statistics in the original signal set ($[\tilde{\chi}_1 = 250, \tilde{\chi}_2 = 400\text{GeV}]$ and $[\tilde{\chi}_1 = 200, \tilde{\chi}_2 = 450\text{GeV}]$), has decreased by more than half. This is an indication that including further trends in the data was destructive for training. In other words, the **PNN** suffered from poor training memory.

To summarize the comparisons on the full statistics signal set, I created a pie-plot in figure 4.24. As shown in the figure, the ordinary dense **NN** achieved the highest sensitivity in most of the combinations (49/89), followed by the **PNN** (25/89) and the maxout model (15/89). From the tests we can conclude that the **PNN** network achieves the highest sensitivity, but struggles for unbalanced data sets. On the contrary the ordinary dense neural network performs best with larger amounts of training data, achieving the highest sensitivity on the most amount of combinations, but never attains the same degree of sensitivity as the **PNN**. The maxout layer underperforms on most combinations, but exhibits impressive training memory when attaining the highest significance on the lowest statistics combinations.

4.8 Comparing Exclusion Limits between ML Models and Previous Analysis

In the previous section I compared the achieved significance between the three optimal models for the full statistics signal set. In this section I will do the same, but with the introduction of a flat uncertainty in the background. Additionally, I will compare the achieved exclusion limits (the mass combinations with an achieved significance of over 1.64) by the models created in this thesis, with the limit set in the paper by

⁴⁰In an unbalanced data set, smaller trends can tend to be ignored due to "memory loss".

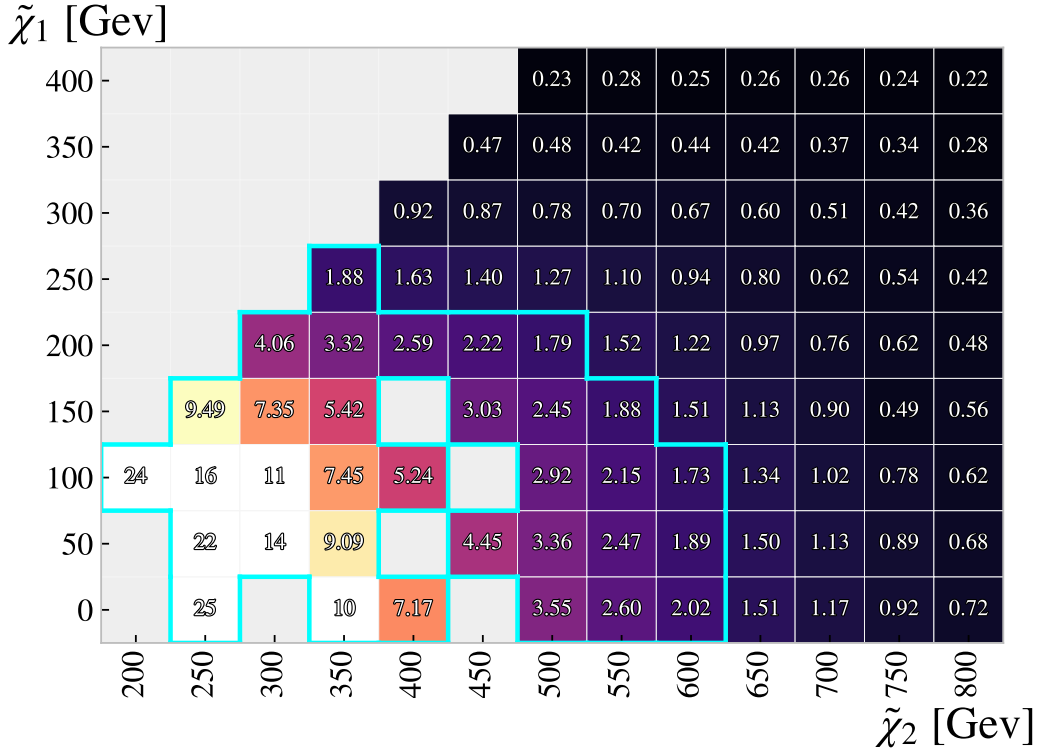


Figure 4.23: A grid displaying the achieved significance on the full statistics signal set, using the signal region created by the *PNN* network.

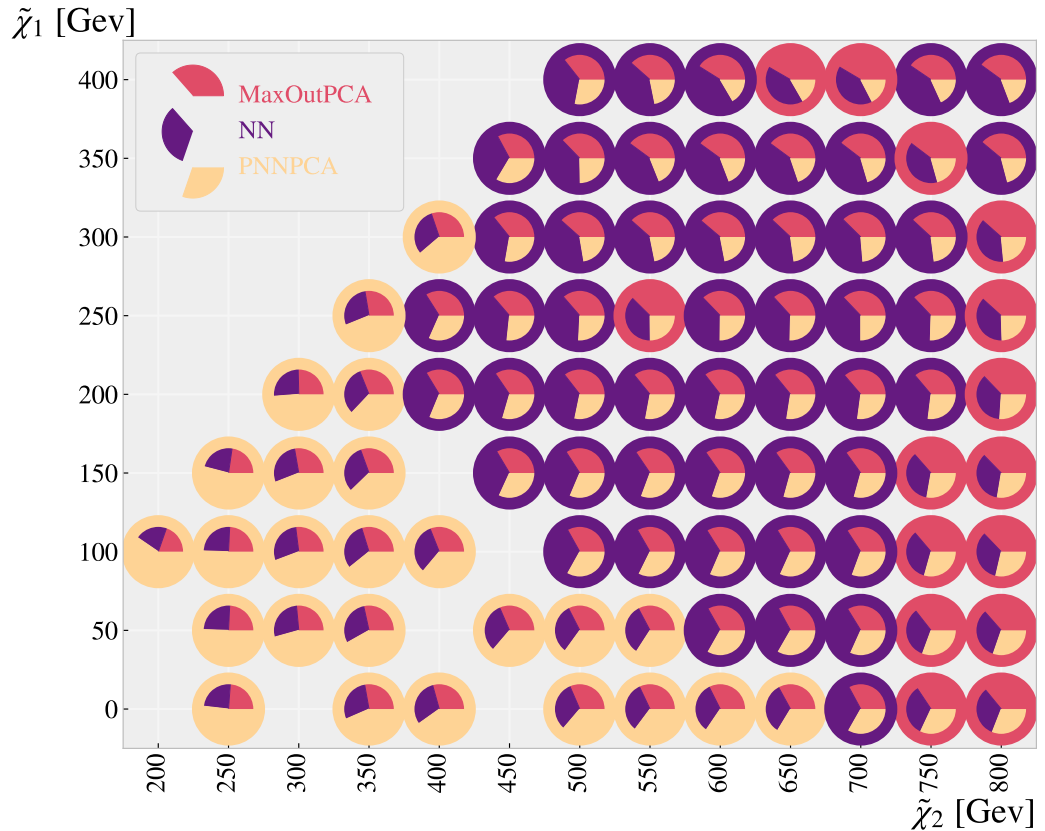


Figure 4.24: A grid displaying the achieved significance on the full statistics signal set, using the signal region created by the *PNN* network.

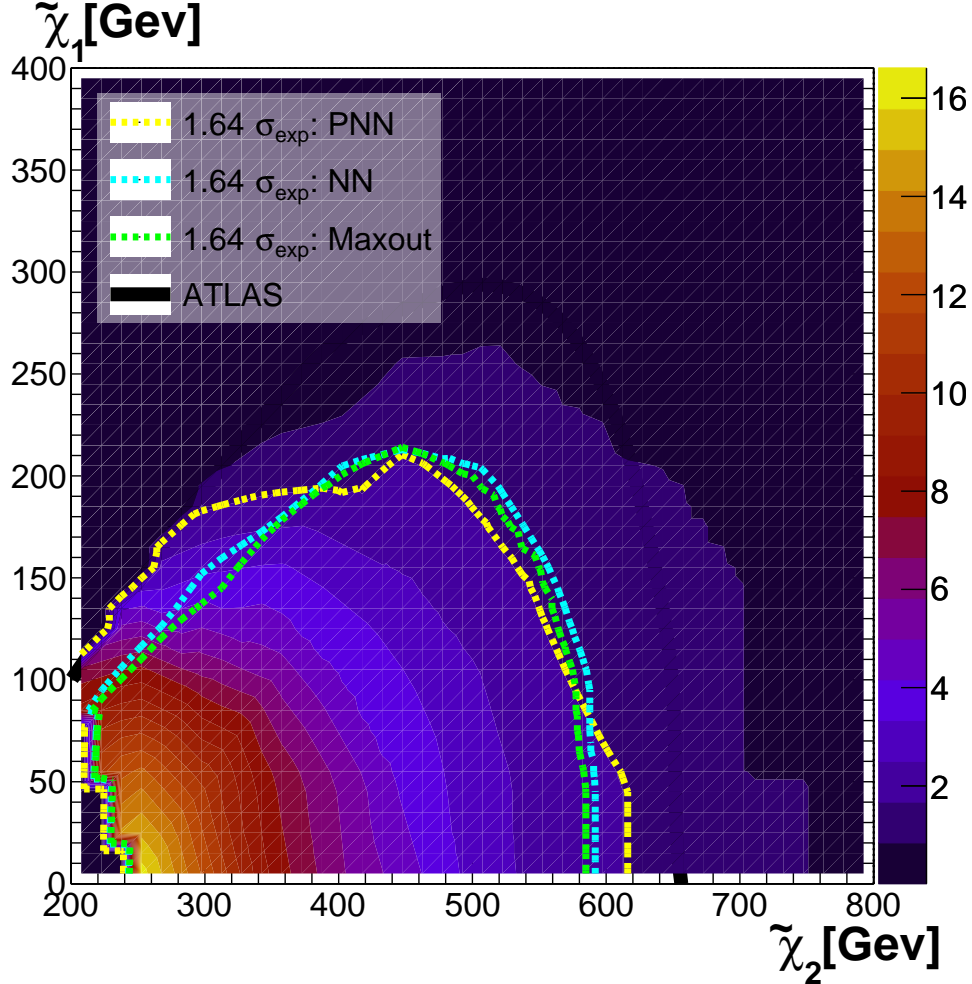


Figure 4.25: A grid displaying the achieved significance on the full statistics signal set, using the signal region created by the **PNN** network.

ATLAS in 2021 [35].

In the analysis by ATLAS, they have not assumed a flat uncertainty. Instead, an analysis has been made based on individual regions and collision processes. Due to time constraints, a flat uncertainty has been made for comparison reasons. Aligning with what I have found when reading similar analysis (as well as based on recommendation from my supervisors), the uncertainty will be in the region of 20% of the **SM** background. To further study the limits, I will additionally compare the models with an uncertainty of 10%.

In figure ??, I have drawn the contours of the significance achieved using the **PNN**, while outlining all points corresponding to a significance of 1.64. The same outline has been made on top of the contours of the **PNN** for the dense **NN**, maxout model and the statistical analysis made by ATLAS. The calculations of the significance for the output of the **ML** models were made with a flat uncertainty equal to 20% of the background. The figure shows that none of the models are able to extend the sensitivity achieved by ATLAS, although the **PNN** was able to equal the ATLAS analysis for smaller masses.

A similar figure to what was presented above, was made in figure 4.26. This figure presents the results while applying an uncertainty equal to 10% of the background. Compared to the limits in figure 4.25, figure 4.26 displays a far closer comparison between all three models and the results from ATLAS. In this comparison, the dense **NN** and maxout model were able to extend the sensitivity of the **PNN** for larger masses of both $\tilde{\chi}_1$ and $\tilde{\chi}_2$, but were beaten in most areas. The **PNN** is very close to being able to extend the sensitivity from ATLAS, for high masses of $\tilde{\chi}_2$ and low masses of $\tilde{\chi}_1$.

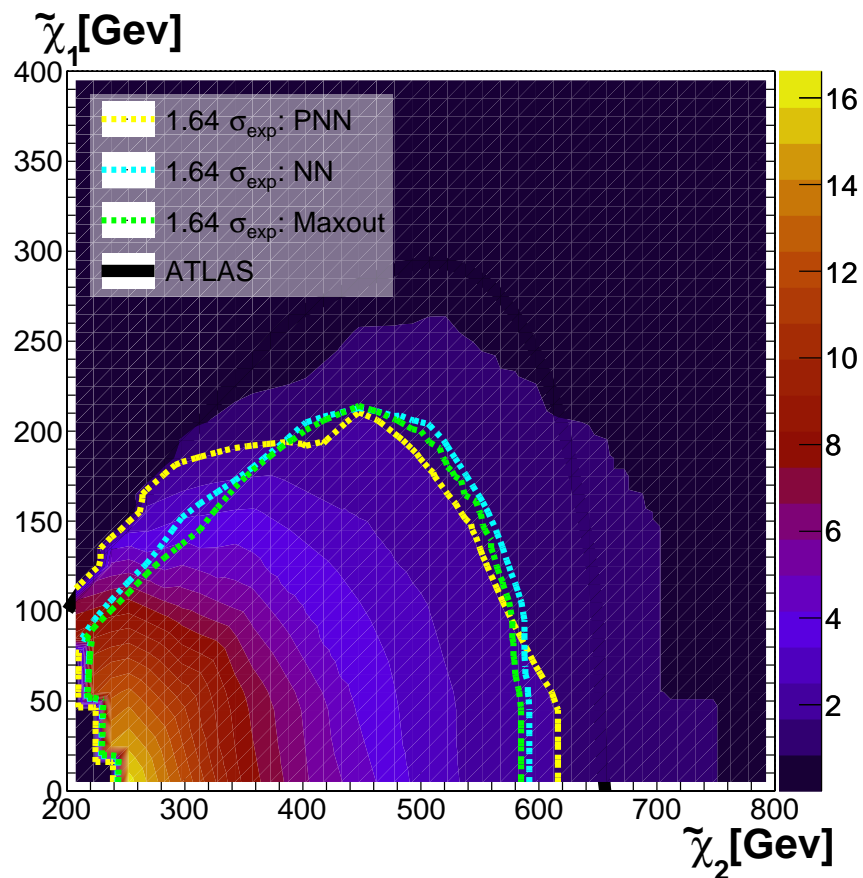


Figure 4.26: A grid displaying the achieved significance on the full statistics signal set, using the signal region created by the *PNN* network.

Appendices

Appendix A

A.1 Sensitivity Grids

A.1.1 Ensembles

A.1.2 Results from the [PCA](#)

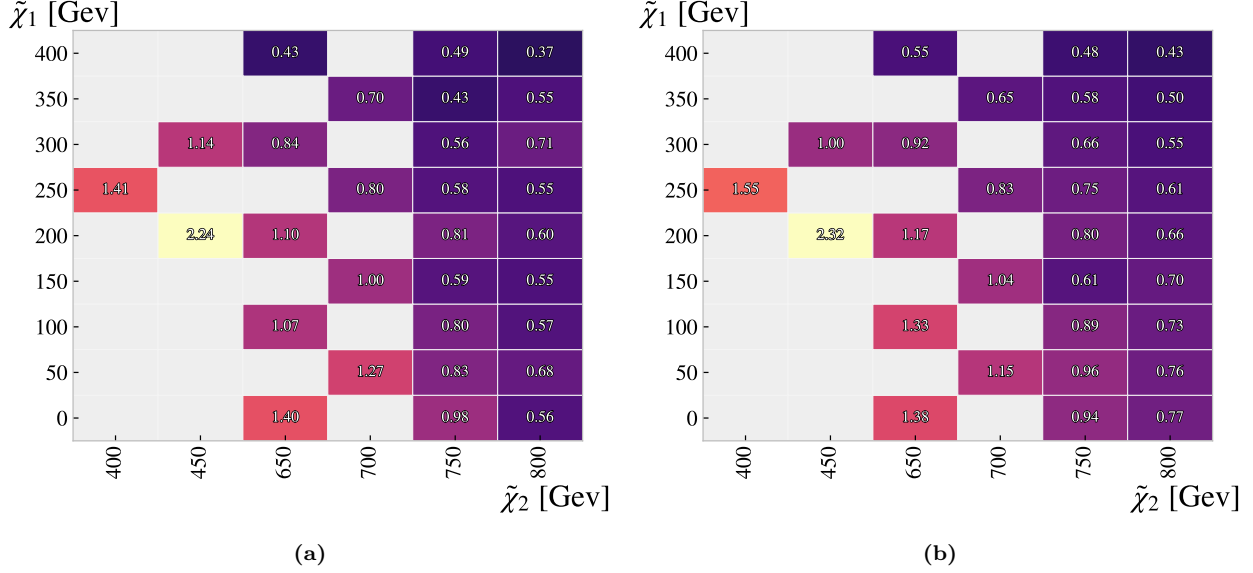


Figure 27: A grid displaying the achieved significance on the original signal set, using the signal region created by the [SCO 27a](#) and a channel-out network [27b](#). A [PCA](#) analysis has been applied to the data being utilized in this result.

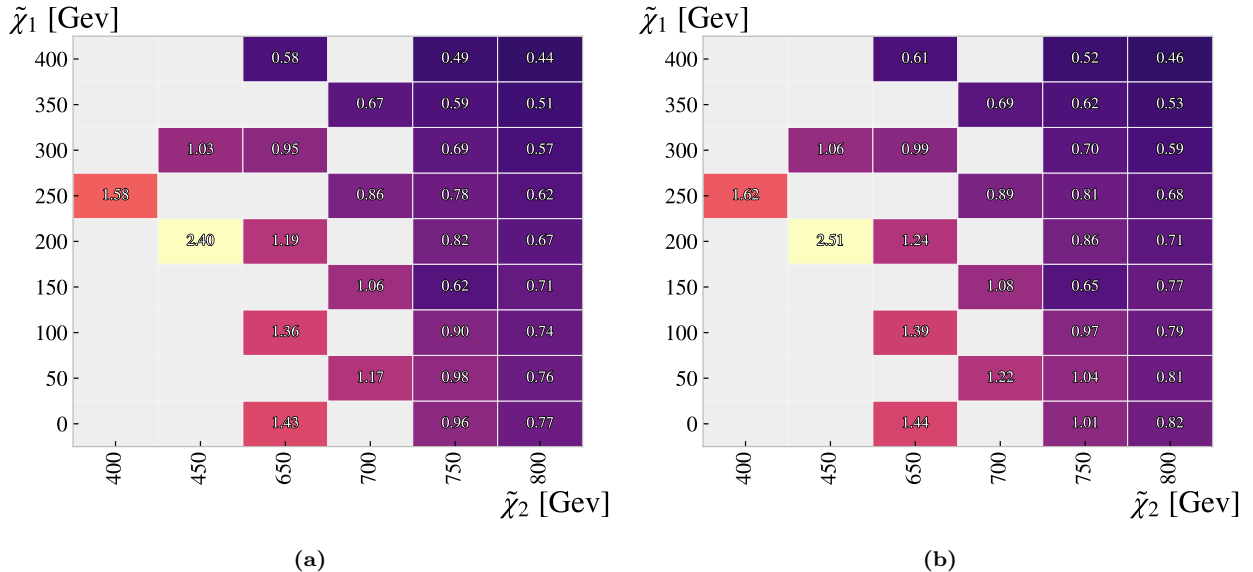


Figure 28: A grid displaying the achieved significance on the original signal set, using the signal region created by the [NN 28a](#) and a maxout network [28b](#). A [PCA](#) analysis has been applied to the data being utilized in this result.

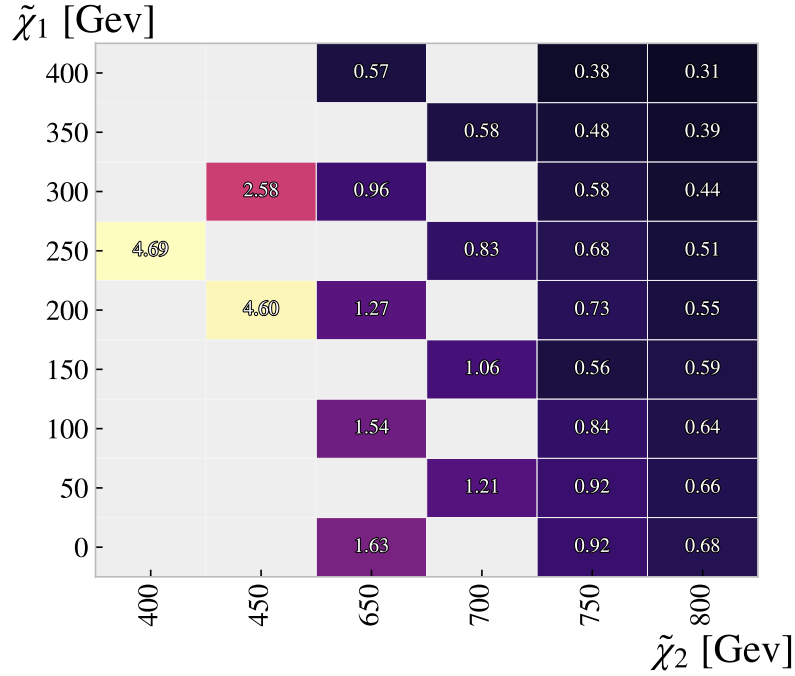


Figure 29: A grid displaying the achieved significance on the original signal set, using the signal region created by the [PNN](#) network. A [PCA](#) analysis has been applied to the data being utilized in this result.

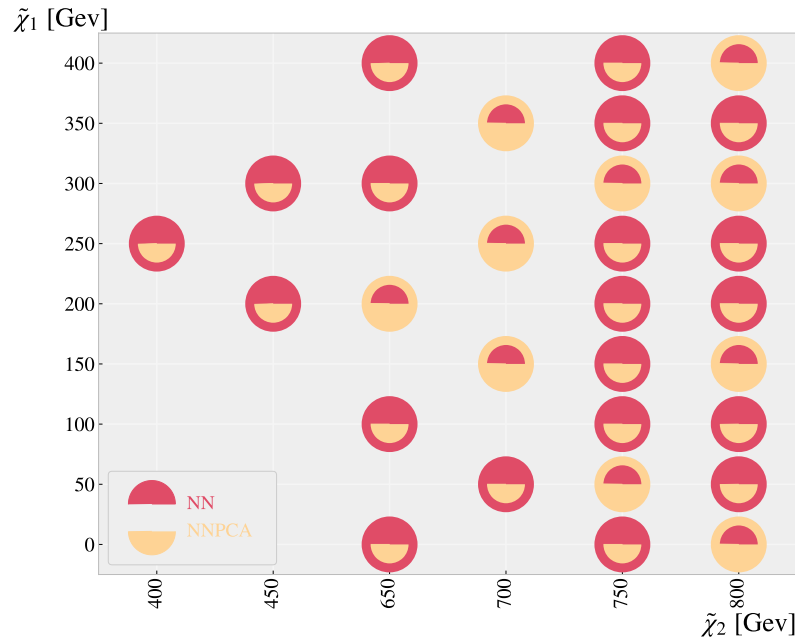


Figure 30: A grid displaying the achieved significance on the original signal set, using the signal region created by the [NN](#) network. A [PCA](#) analysis has been applied to the data being utilized in this result.

A.2 The Features

A.2.1 The Feature Distribution

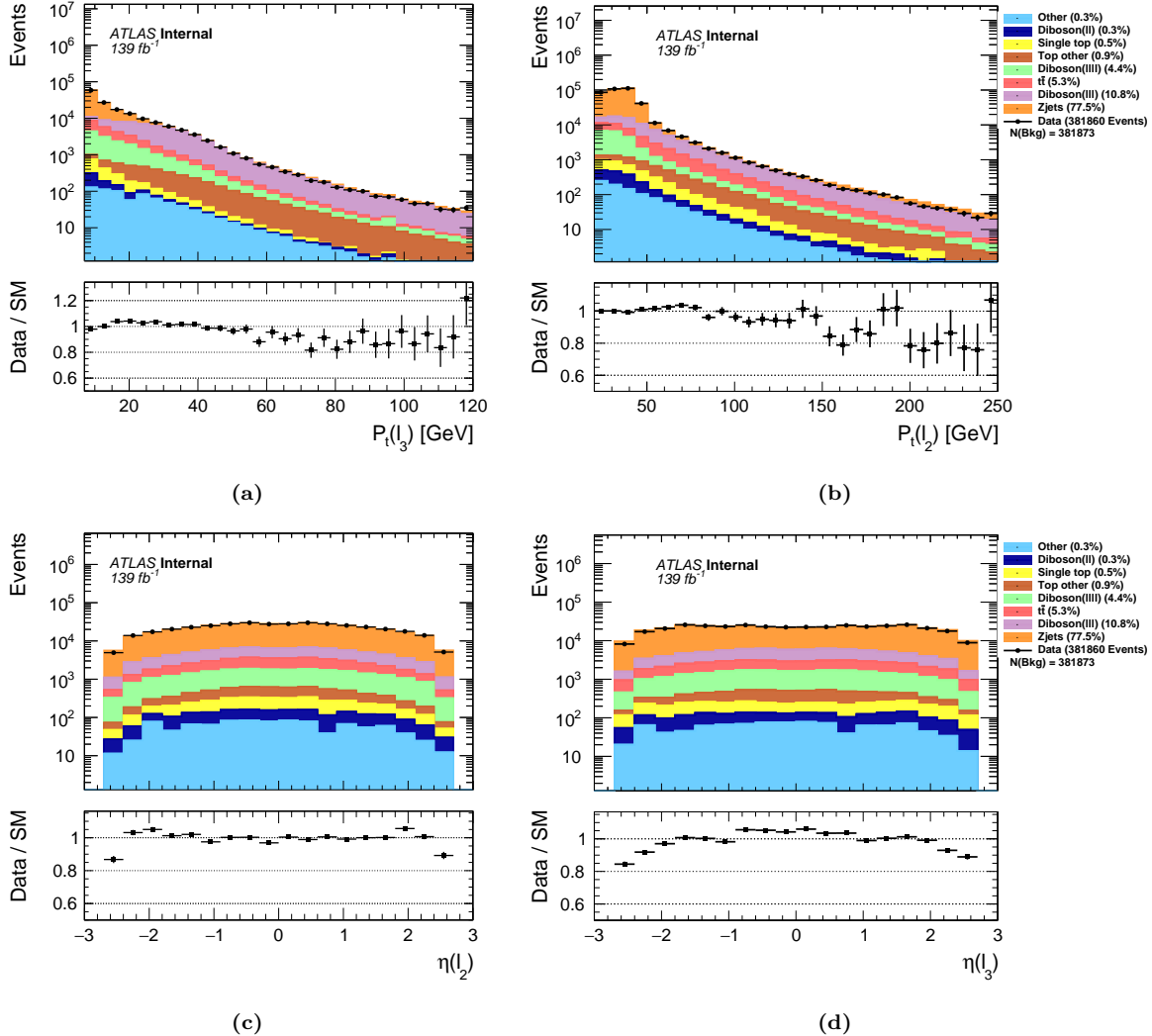


Figure 31: MC and real data comparison and event distribution for each channel over P_t for the first 3.4a, second 31b and third 31a lepton. Similarly, the distribution over η for the 3.4b, second 31c and third 31d lepton.

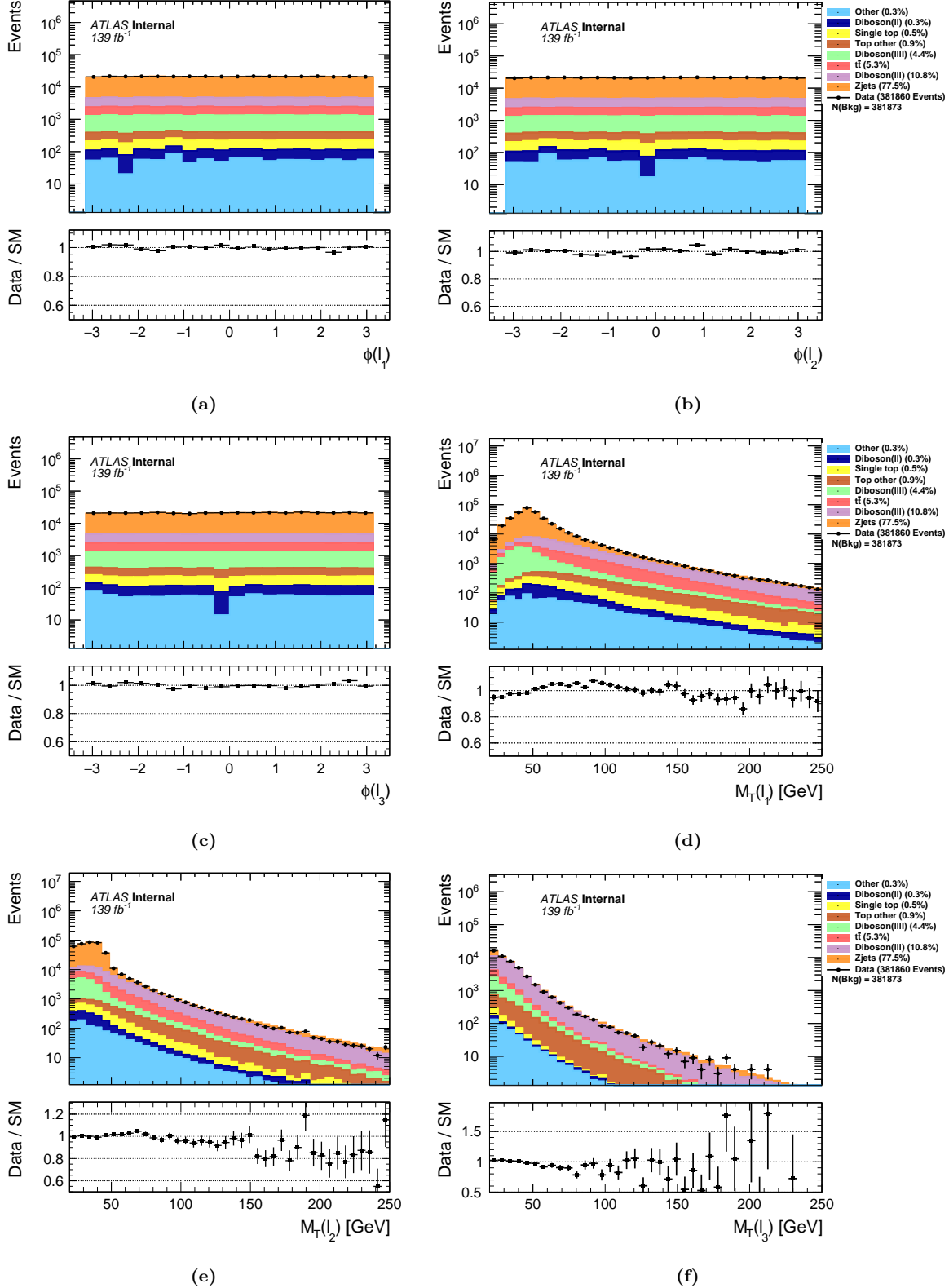


Figure 32: MC and real data comparison and event distribution for each channel over ϕ for the first 32a, second 32b and third 32c lepton. Similarly, the distribution over m_t for the first 32d, second 32e and third 32f lepton.

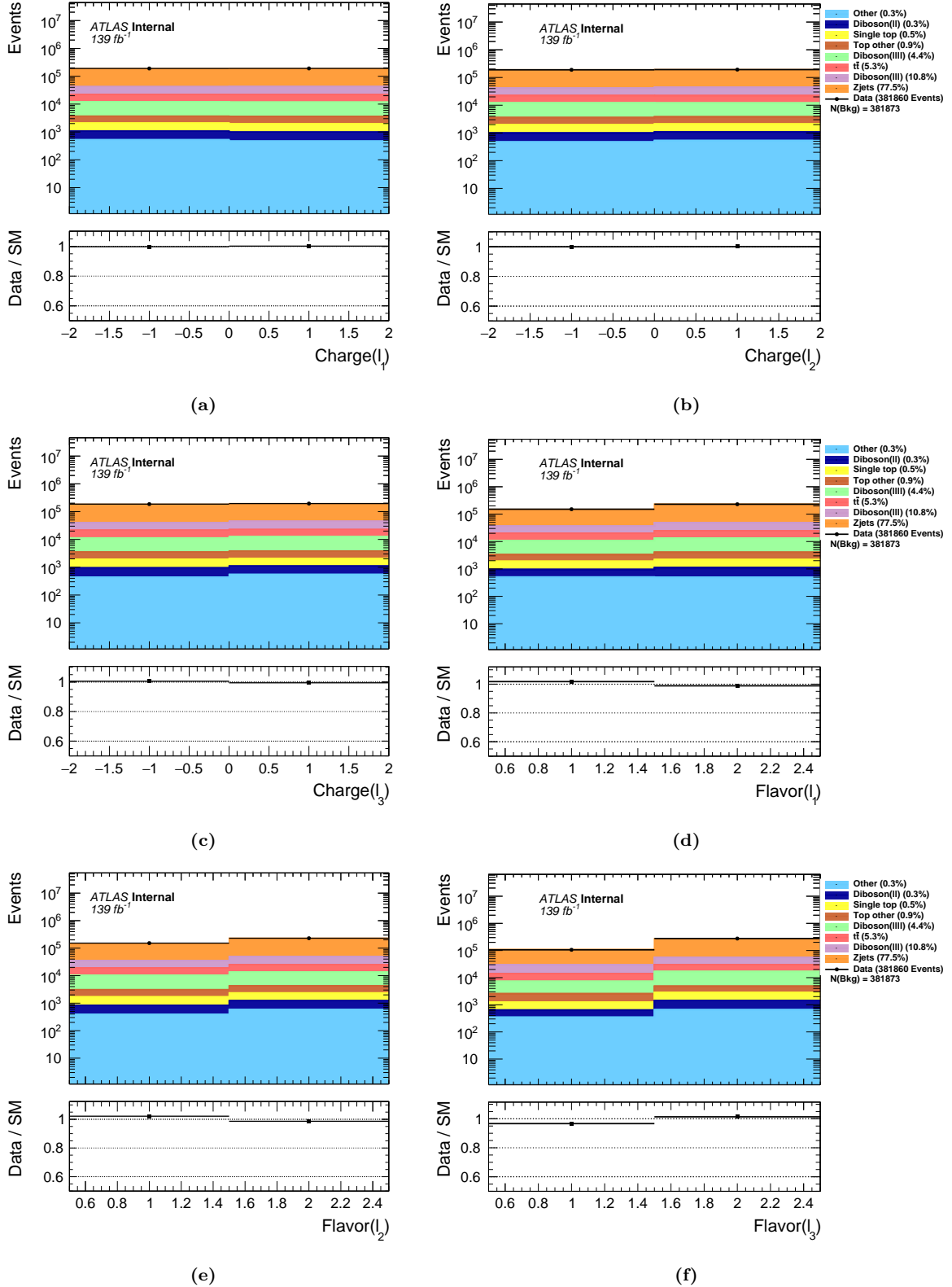


Figure 33: MC and real data comparison and event distribution for each channel over the charge for the first 33a , second 33b and third 33c lepton. Similarly, the distribution over the flavor for the first 33d, second 33e and third 33f lepton

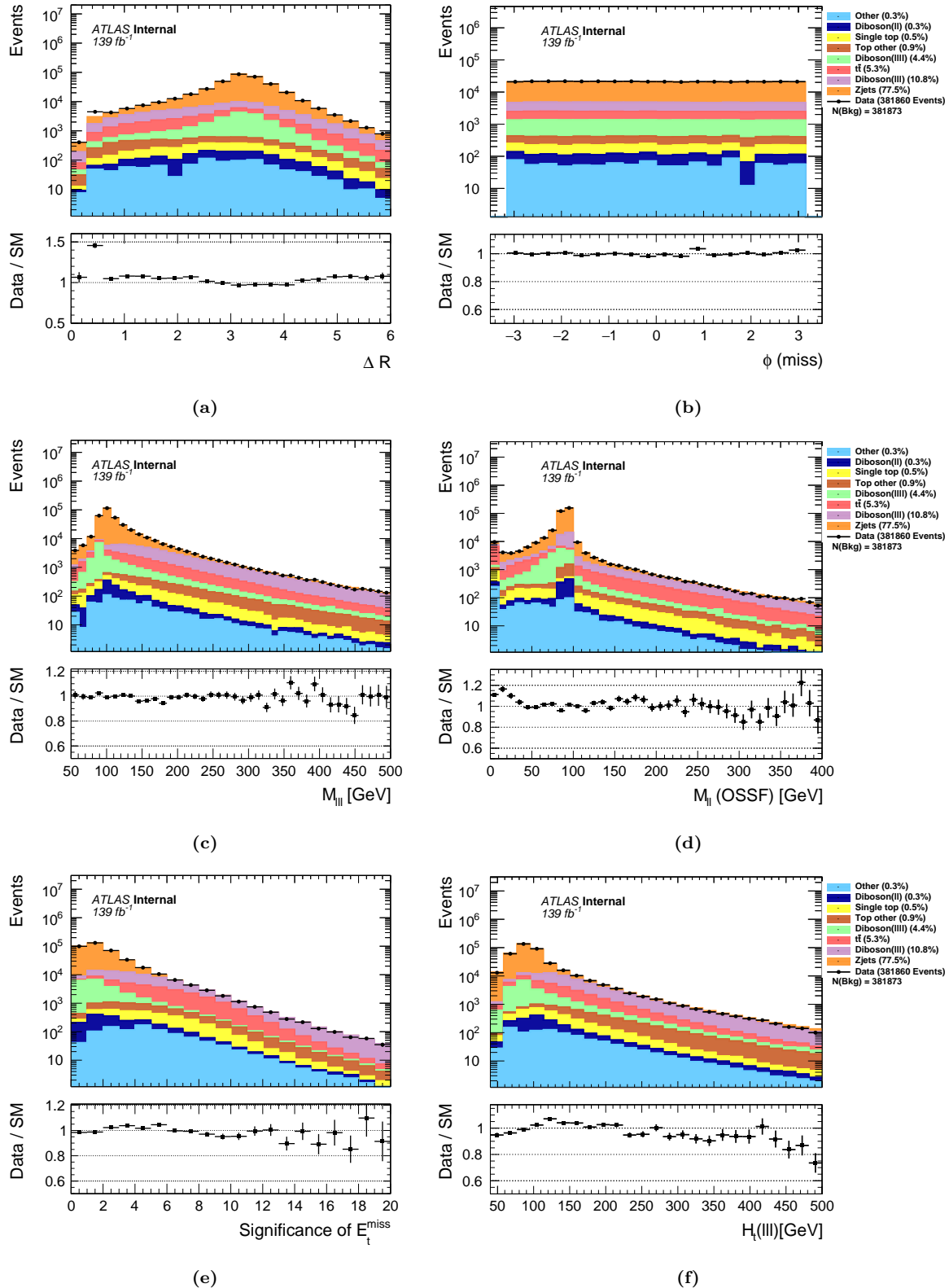


Figure 34: MC and real data comparison and event distribution for each channel over the energy 3.4c and azimuthal angle 34b for the transverse momentum. The distribution of the invariant mass of the three leptons 34c and the OSSF pair 34d. The distribution over the significance of the missing transverse energy 34e and the sum of P_t 34f.

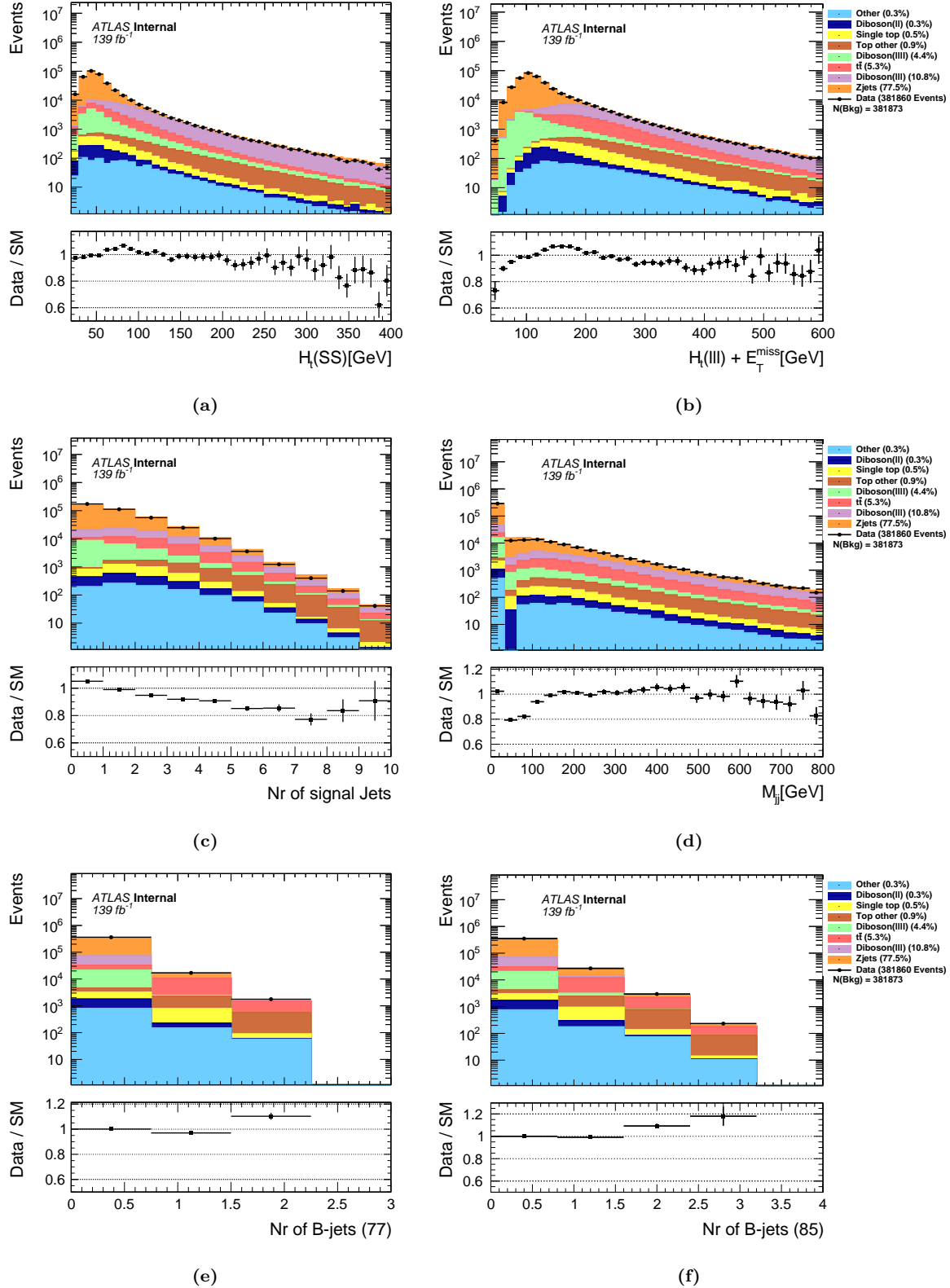


Figure 35: MC and real data comparison and event distribution for each channel over the sum of P_t for the SS pair 35a and the sum over all three leptons added with E_t^{miss} 35b. The distribution over ΔR 34a and the flavor combination of the three leptons 34d. The distribution of number of jets 35c and the mass of the leading di-jet pair 35d.

Feature Name	Description
P_t	Transverse momentum
η_t	Pseudo rapidity
ϕ_t	Azimuthal angle
M_T	Transverse mass
$Charge$	EM charge
$Flavour$	Particle type
E_T^{miss}	Transverse missing energy
$\phi(miss)$	Azimuthal angle of the missing energy
M_{lll}	Trilepton mass
$M_{ll}(OSSF)$	Mass of the OSSF pair
Sig E_T^{miss}	Significance of E_T^{miss}
$H_t(lll)$	Sum of P_t for all three leptons
$H_t(SS)$	Sum of P_t for the SS pair
$H_t(lll) + E_T^{miss}$	-
ΔR	Distance defined in the $\eta - \phi$ space
Flavor combo	Combination of flavors for all three leptons
Nr of signal Jets	Nr of jets passing the signal criteria
M_{jj}	Mass of the leading jet pair
Nr of B-jets(77)	-
Nr of B-jets(85)	-

Table 2: A summary and description of all features used in this analysis.

A.3 The implementation of Channel-Out, SCO and Maxout

Channel-out

For the activation function defined to create the channel-out layer, I again grouped the nodes similarly as I did for max-out. Instead of returning the largest value from each unit, I used TensorFlow's function, `tf.greater_equal` to create a tensor with booleans. The booleans are chosen by comparing each unit to the largest value in that unit. By multiplying this tensor to the original input, I am left with the desired result of a tensor containing the largest activated nodes along with the rest whom are now set to zero.

```

1 def call(self, inputs: tf.Tensor, mask: tf.Tensor = None) -> tf.Tensor:
2     # Pass input through weight kernel and adding bias terms.
3     inputs = gen_math_ops.MatMul(a=inputs, b=self.kernel)
4     inputs = nn_ops.bias_add(inputs, self.bias)
5
6     num_inputs = inputs.shape[0]
7     if num_inputs is None:
8         num_inputs = -1
9
10    # Reshaping inputs such that they are grouped correctly
11    num_competitors = self.units // self.num_groups
12    new_shape = [num_inputs, self.num_groups, num_competitors]
13    inputs = tf.reshape(inputs, new_shape)
14
15    # Finding maximum activations and setting losers to 0.
16    outputs = tf.math.reduce_max(inputs, axis=-1, keepdims=True)
17    outputs = tf.where(tf.equal(inputs, outputs), outputs, 0.)
18    # Reshaping outputs to original input shape
19    outputs = tf.reshape(outputs, [num_inputs, self.units])
20
21    self.counter = outputs
22    return outputs

```

Listing 1: Python implementation for the custom activation function used to define the channel-out layer.

```

1 def call(self, inputs: tf.Tensor, mask: tf.Tensor = None) -> tf.Tensor:
2     inputs = gen_math_ops.MatMul(a=inputs, b=self.kernel)
3     inputs = nn_ops.bias_add(inputs, self.bias)
4     #tf.print(inputs)
5     num_inputs = inputs.shape[0]
6
7     if num_inputs is None:

```

```

8     num_inputs = -1
9
10    shuffle_index = tf.random.shuffle(self.index)
11    unshuffle_index = tf.tensor_scatter_nd_update(tensor = self.zeros ,
12                                                 indices = tf.reshape(shuffle_index
13                                                 ,
14                                                 [inputs.shape
15                                                 [1],1]),
16                                                 updates = self.index)
17
18    # Reshaping inputs such that they are grouped correctly
19    num_competitors = self.units // self.num_groups
20    new_shape = [num_inputs, self.num_groups, num_competitors]
21    inputs_s = tf.reshape(inputs_s, new_shape)
22
23    # Finding maximum activations and setting losers to 0.
24    outputs = tf.math.reduce_max(inputs_s, axis=-1, keepdims=True)
25
26    outputs = tf.where(tf.equal(inputs_s, outputs), 1.0, 0.)
27    # Reshaping outputs to original input shape
28    outputs = tf.reshape(outputs, [num_inputs, self.units])
29
30    outputs = tf.gather(outputs, unshuffle_index, axis = 1)
31    outputs = tf.multiply(inputs, outputs)
32    self.counter = outputs
33    return outputs

```

Listing 2: Python implementation for the custom activation function used to define the SCO layer.

```

1 def call(self, inputs: tf.Tensor) -> tf.Tensor:
2     # Passing input through weight kernel and adding bias terms
3     inputs = gen_math_ops.MatMul(a=inputs, b=self.kernel)
4     inputs = nn_ops.bias_add(inputs, self.bias)
5
6     num_inputs = inputs.shape[0]
7     if num_inputs is None:
8         num_inputs = -1
9     num_competitors = self.units // self.num_groups
10    new_shape = [num_inputs, self.num_groups, num_competitors]
11
12    # Reshaping outputs such that they are grouped correctly
13    inputs = tf.reshape(inputs, new_shape)
14    # Finding maximum activation in each group
15    outputs = tf.math.reduce_max(inputs, axis=-1, keepdims=True)
16
17    counter = tf.where(tf.equal(inputs, outputs), outputs, 0.)
18    # Reshaping outputs to original input shape
19    self.counter = tf.reshape(counter, [num_inputs, self.units])
20
21    return tf.reshape(outputs, [num_inputs, self.num_groups])

```

Listing 3: Python implementation for the custom activation function used to define the max-out layer.

Acronyms

ADAM	Adaptive Moment Estimation	ROC	Receiver Operating Characteristic
API	Application Programming Interface	SCO	Stochastic-Channel-Out
ATLAS	A Toroidal LHC Apparatus	SGD	Stochastic Gradient Decent
AUC	Area Under the Curve	SM	Standard Model
BDT	Boosted Decision Trees	SMM	Several-Mass-Model
BEH	Brout-Englert-Higgs	SP	Superpartner
BSM	Beyond Standard Model	SR	Signal region
CC	Cut-and-Count	SS	Same Sign
CNN	Convolutional Neural Network	SUSY	Supersymmetry
CP	Charge-Parity		
DNN	Deep Neural Networks		
DT	Decision Trees		
EM	Electromagnetic		
FFNN	Feed-Forward Neural Network		
FSMLM	Full Statistics Minus Low Masses		
HEP	High Energy Physics		
HPC	High Performance Computing		
LHC	Large Hadron Collider		
MC	Monte Carlo		
ML	Machine Learning		
MSSM	Minimal Supersymmetric Standard Model		
NN	Neural Network		
OMM	One-Mass-Model		
OSSF	Opposite Sign Same Flavour		
PCA	Principal Component Analysis		
PNN	Parametrized Neural Network		
QCD	Quantum Chromo Dynamics		
QED	Quantum Electro Dynamics		
QFT	Quantum Field Theory		
RNN	Recursive Neural Network		

Bibliography

- [1] G. Aad, T. Abajyan, B. Abbott, J. Abdallah, S. A. Khalek, A. Abdelalim et al., *Observation of a new particle in the search for the standard model higgs boson with the ATLAS detector at the LHC*, *Physics Letters B* **716** (sep, 2012) 1–29.
- [2] J. J. T. M. F.R.S., *Xlviii. the relation between the atom and the charge of electricity carried by it*, *The London, Edinburgh, and Dublin Philosophical Magazine and Journal of Science* **40** (1895) 511–544, [<https://doi.org/10.1080/14786449508620801>].
- [3] P. E. R. F.R.S., *Lxxix. the scattering of α and β particles by matter and the structure of the atom*, *The London, Edinburgh, and Dublin Philosophical Magazine and Journal of Science* **21** (1911) 669–688, [<https://doi.org/10.1080/14786440508637080>].
- [4] F. Reines and C. L. Cowan, *The neutrino*, *Nature* **178** (1956) 446–449.
- [5] J. Bernstein, *Spontaneous symmetry breaking, gauge theories, the higgs mechanism and all that*, *Rev. Mod. Phys.* **46** (Jan, 1974) 7–48.
- [6] SUPER-KAMIOKANDE COLLABORATION collaboration, Y. Fukuda, T. Hayakawa, E. Ichihara, K. Inoue, K. Ishihara, H. Ishino et al., *Evidence for oscillation of atmospheric neutrinos*, *Phys. Rev. Lett.* **81** (Aug, 1998) 1562–1567.
- [7] J. Joyce, *Finnegans Wake*. Penguin Books, New York, 1999.
- [8] W. Thomson, *Lord kelvin addresed the british association for the advancement of science*, 1900.
- [9] O. Antipin, D. Atwood and A. Soni, *Search for rs gravitons via wlwl decays*, *Physics Letters B* **666** (2008) 155–161.
- [10] E. Oks, *Brief review of recent advances in understanding dark matter and dark energy*, .
- [11] D. Chung, L. Everett, G. Kane, S. King, J. Lykken and L.-T. Wang, *The soft supersymmetry-breaking lagrangian: theory and applications*, *Physics Reports* **407** (2005) 1–203.
- [12] J. Pequenao, “Event Cross Section in a computer generated image of the ATLAS detector..” 2008.
- [13] E. Gramstad, *Searches for supersymmetry in di-lepton final states with the ATLAS detector at $\sqrt{s} = 7 \text{ TeV}$* , .
- [14] D. Guest, J. Collado, P. Baldi, S.-C. Hsu, G. Urban and D. Whiteson, *Jet flavor classification in high-energy physics with deep neural networks*, *Physical Review D* **94** (dec, 2016) .
- [15] J. Pumplin, *How to tell quark jets from gluon jets*, *Phys. Rev. D* **44** (Oct, 1991) 2025–2032.
- [16] D. P. Kingma and J. Ba, “Adam: A method for stochastic optimization.” 10.48550/arXiv.1412.6980.
- [17] F. Pedregosa, G. Varoquaux, A. Gramfort, V. Michel, B. Thirion, O. Grisel et al., *Scikit-learn: Machine learning in Python*, *Journal of Machine Learning Research* **12** (2011) 2825–2830.
- [18] Q. Wang and J. JaJa, “From maxout to channel-out: Encoding information on sparse pathways.”
- [19] P. Baldi, K. Cranmer, T. Fauchet, P. Sadowski and D. Whiteson, *Parameterized machine learning for high-energy physics*, **1601.07913 [hep-ex, physics:hep-ph]**.
- [20] T. Chen and C. Guestrin, *XGBoost: A scalable tree boosting system*, in *Proceedings of the 22nd ACM SIGKDD International Conference on Knowledge Discovery and Data Mining*, KDD ’16, (New York, NY, USA), pp. 785–794, ACM, 2016. [DOI](#).
- [21] T. Chen and C. Guestrin, *XGBoost*, in *Proceedings of the 22nd ACM SIGKDD International Conference on Knowledge Discovery and Data Mining*, ACM, aug, 2016. [DOI](#).
- [22] M. Bugge, *Discovery and exclusion in high energy physics*, 2022.
- [23] S. Raychaudhuri, *Introduction to monte carlo simulation*, in *2008 Winter Simulation Conference*, pp. 91–100. [DOI](#).
- [24] R. Brun and F. Rademakers, *Root - an object oriented data analysis framework*, in *AIHENP’96 Workshop, Lausane*, vol. 389, pp. 81–86, 1996.
- [25] The Root team, “Rdataframe.”
- [26] T. pandas development team, *pandas-dev/pandas: Pandas*, Feb., 2020. 10.5281/zenodo.3509134.
- [27] The Root team, “Tlorentzvector.”
- [28] M. Franchini, K. H. Mankinen, G. Carratta, F. Scutti, A. Gorisek, E. Lytken et al., *Search for type-III seesaw heavy leptons in dilepton final states in pp collisions at $\sqrt{s} = 13 \text{ TeV}$ with the ATLAS detector*, .
- [29] M. Aaboud, , G. Aad, B. Abbott, D. C. Abbott, O. Abdinov et al., *Electron reconstruction and identification in the ATLAS experiment using the 2015 and 2016 LHC proton–proton collision data at $\sqrt{s}= 13 \text{ TeV}$* , *The European Physical Journal C* **79** (aug, 2019) .
- [30] ATLAS collaboration, G. Aad, B. Abbott, D. Abbott, A. Abed Abud, K. Abeling,

- D. Abhayasinghe et al., *Observation of WWW production in pp collisions at $\sqrt{s} = 13$ TeV with the ATLAS detector. Observation of WWW Production in pp Collisions at $\sqrt{s} = 13\text{eV}$ with the ATLAS Detector*, *Phys. Rev. Lett.* **129** (2022) 061803, [[2201.13045](#)].
- [31] P. Liashchynskyi and P. Liashchynskyi, *Grid search, random search, genetic algorithm: A big comparison for nas*, 2019. [10.48550/ARXIV.1912.06059](#).
- [32] A. Gholamy, V. Kreinovich and O. Kosheleva, *Why 70/30 or 80/20 relation between training and testing sets: A pedagogical explanation*, .
- [33] ATLAS collaboration, *Performance of the Reconstruction and Identification of Hadronic Tau Decays with ATLAS*, tech. rep., CERN, Geneva, 2011.
- [34] ATLAS collaboration, *Performance of Top Quark and W Boson Tagging in Run 2 with ATLAS*, tech. rep., CERN, Geneva, 2017.
- [35] A. Collaboration, “Search for chargino–neutralino pair production in final states with three leptons and missing transverse momentum in $\sqrt{s} = 13\text{ TeV}$ pp collisions with the ATLAS detector.” [10.1140/epjc/s10052-021-09749-7](#).